THEORETICAL AND EXPERIMENTAL ANALYSES OF INTERFACE DELAMINATION IN THIN-FILM/SUBSTRATE SYSTEMS

HAIYAN JIANG

(B. Sci. Fudan University)

A THESIS SUBMITTED

FOR THE DEGREE OF MASTER OF SCIENCE

DEPARTMENT OF MATERIALS SCIENCE

NATIONAL UNIVERSITY OF SINGAPORE

2005

ACKNOWLEDGEMENT

The author would like to express her sincere gratitude and heartfelt appreciation to her supervisors, Dr. Kaiyang Zeng and Dr. Yong-wei Zhang, for their continuous encouragement, guidance and valuable advice throughout this project. The concepts, knowledge and scientific analysis methods the author gained from them are not only invaluable to this project but also beneficial to the author's future works.

The author would also emphasize her appreciation to Ms. Lu Shen, for her technical support and advice, without which this project could not be finished in time. The author would like to thank Mr. Shan Gao, Ms. Joyce Pei Ting Tan, Mr. Chunguang Tang, and Mr. Shuang Yang, for their valuable suggestions and encouragement.

Special appreciation is extended to Mr. Yuefeng Ma, for his great help in data processing and invaluable suggestions in problem discussions.

No words can adequately express the author's appreciation to her parents, her grandmother and all her good friends in Singapore, China, USA, Britain, Australia and so on, for their continuous encouragement and understanding throughout the days for this project.

Last but not the least, special thanks and prayers for her loved grandfather.

TABLE OF CONTENTS

SUMMARY

The mechanical behavior and interface adhesion properties of thin film systems during indentation tests have been investigated by finite element method (FEM) and indentation experiments using a micro-wedge-tip indenter. Special attention is paid to the onset and propagation of interface delaminations, as well as their effects on the indentation response.

In the FEM simulations, a traction separation law (TSL) instead of conventional crack growth criterion is employed to describe the interface adhesion due to the presence of large-scale yielding condition during delaminations. The effects of dominant parameters of TSL, i.e., interface strength and interface energy, on the initiation of interface delamination, have been investigated by parametric studies. A methodology, which is capable of determining the interface adhesion properties of thin-film/substrate systems, has been proposed based on the results of parametric studies.

Indentation tests using a micro-wedge-tip indenter have been performed to investigate the delamination process and the mechanical properties of selected thin-film/substrate systems. An indentation range, in which the experimentally-measured properties are less affected by the substrate, is determined by re-arranging the load-penetration curves and defining an effective stiffness. Thus, the film-only reduced modulus and yield strength can be derived, which are further used to perform numerical simulations to extract the interface adhesion properties of the thin-film/substrate systems tested.

It is found that the simulation results agree well with the experimental ones: similar characteristics of the load-penetration curves corresponding to the interface delaminations have been observed in both the simulation and experimental results. Furthermore, the values of the interface adhesion properties of the 500nm BD/Si system are extracted by fitting the load-penetration curve obtained by experiment with the one obtained by simulations.

Keywords:

nanoindentation, traction separation law, interface delamination, effective stiffness, interface strength, interface energy

LIST OF TABLES

LIST OF FIGURES

Chapter 1 Introduction

1.1. Motivations and Objectives

In recent years, a wide range of applications of thin-film/substrate systems have been found in micro-electronic and optoelectronic devices. Driven by these applications, various techniques, such as sputtering, vapor deposition, ion implantation and laser glazing, etc., have been developed to fabricate thin-film/substrate systems. An important feature of these thin-film/substrate systems is that, the interfaces between different components or materials are ubiquitous. Even though the films and the substrates fully meet the requirements of the applications, the delaminations of the films from the substrates often lead to the failure of the entire systems. Thus, the interface adhesion quality between the film and substrate, which often plays a dominant role in the reliability and stability of the devices, has drawn much attention [1-8].

Indentation experiments, which have been performed to measure material hardness for more than one hundred years, are now rekindled by the development of new indentation instruments and techniques, as well as the improved theories. Many attempts have been made to use indentation to measure the mechanical properties of hybrid materials, including thin film structures and nanomaterials. Due to the difficulties in interpreting experimental data, it is still a challenging issue to extract interface adhesion properties by indentation tests directly [5-8].

A finite element method (FEM) [9] based on cohesive zone model has recently

been developed to correlate the interface adhesion of a thin film bonded to a substrate with the indentation load-penetration characteristics. In this model, thin-film/substrate systems are subjected to wedge indentations, which generate interface delamination of the thin film from its substrate. FEM simulations are then used to determine the load-penetration relationship and the critical state of the onset of the interface delamination of the systems during the indentation process, with the interface adhesion properties as initial input data. This approach, known as forward analysis, provides a direct relationship between the interface adhesion properties and experimentally-measured load-penetration curves.

In real application situations, however, indentation load-penetration curves can be readily measured through experiments, whereas interface adhesion properties are to be determined. Therefore, to derive interface adhesion properties, i.e., interface strength and interface energy, from experimentally-measured load-penetration relationship, known as reverse analysis, may be practically more interesting and important in applications.

The main objectives of this project are: 1) to gain fundamental understanding of the interface adhesion properties and the initiation of the delamination of thin film systems during indentation process using finite element modeling and indentation experiments by means of forward analysis; 2) to establish the relationships between the experimentally-measured information (i.e., the load-penetration curves) and the interface adhesion properties of thin film systems by means of reverse analysis; and 3) to develop a general methodology to characterize the interface adhesion properties by

using indentation technique combining with FEM simulations.

1.2. Nanoindentation Test

Indentation technique is a basic tool to characterize the mechanical properties of the surface of bulk materials and thin films [10-21].

It was Moh who first performed a hardness test in 1822 wherein a permanent scratch was left on the material of interest by a harder one. Following the definition of Moh's hardness, i.e., the capability of material resistance against the penetration by another, other tests, such as Brinell, Knoop, Vickers and Rockwell tests, were established by refining the method of indenting one material with another [22].

For so-called nanoindentation tests, the penetration depth during the test is in the order of nanometers, which make it possible to characterize the mechanical properties of thin film systems. The load-penetration curve, which is recorded continuously during indentation experiments, can be used to derive many important mechanical properties, such as hardness and elastic modulus [12-14]. The elastic modulus obtained by this technique is consistent with that obtained by the conventional standard tensile testing for many materials [23-25]. Nanoindentation experiments are now attempted to characterize the interface adhesion properties and the onset of delamination process of the thin-film/substrate systems. In this project, we therefore use the nanoindentaion technique to experimentally investigate the characteristics of the interface delaminations of thin-film/substrate systems.

1.3. Finite Element Modeling

FEM has been well established nowadays and it can be used for solving a wide variety of practical problems. The method may be dated back to the analysis of aircraft structural problems presented by Turner et al. [26] in 1956, in which simple finite elements (pin-jointed bars and triangular plates) were used. In 1968, Przemieniecki [27] applied FEM to stress analysis problems. Zienkiewicz and Cheung [28] gave a broad interpretation of FEM and its applicability to any general field problem in 1967, which gave an impulse to a wider range of applications of FEM to solutions to linear and non-linear differential equations. Over the years, FEM has been used to solve different types of applied science and engineering problems with the improvement of the speed and accuracy of computers.

The basic idea of FEM is to find the solution to a complicated problem by replacing it with a simpler one [29]. The discretization of the solution region, which is considered as a build-up of many small, interconnected subregions called finite element, is the first step in the FEM. This is equivalent to approximating the original problem that has an infinite number of degrees of freedom by a simpler one that has a finite number of degrees of freedom. The shapes, sizes, number and configurations of the elements should be chosen to simulate the original body or domain as closely as possible with respect to the computational time involved for the solution. Thus, it becomes possible to find an approximate solution in the absence of mathematical tool for the exact one to the practical problem. Generally, it is possible to improve or refine the approximate solution by spending more computational effort.

1.4. Scope

This thesis is divided into five chapters and two appendices. Chapter 2 gives a brief introduction to the theories of indentation tests. The basic theories and formulations involved in finite element modeling are presented in Chapter 3, together with the discussions of the simulation results. Chapter 4 deals with the experimental results and discussions. Conclusions and future work are presented in Chapter 5.

References

[1]. J. A. Knapp, D. M. Follstaedt, S. M. Myers, J. C. Barbour and T. A. Friedamnn, J. Appl. Phys. 85 (1999) 1460.

[2]. R. Narasimhan and S. K. Biswas, Int. J. Mech. Sci. 40 (1998) 357.

[3]. M. D. Kiese, W. W. Gerberich and N. R. Moody, J. Mater. Res. 14 (1999) 3007.

[4]. M. D. Kiese, W. W. Gerberich and N. R. Moody, J. Mater. Res. 14 (1999) 3019.

[5]. M. P. De Boer and W. W. Gerberich, Acta Mater. 44 (1996) 3169.

[6]. M. P. De Boer and W. W. Gerberich, Acta Mater. 44 (1996) 3177.

[7]. T. Y. Tsui, J. Vlassak and W. D. Nix, J. Mater. Res. 14 (1999) 2196.

[8]. T. Y. Tsui, J. Vlassak and W. D. Nix, J. Mater. Res. 14 (1999) 2204.

[9]. Y. W. Zhang, K. Y. Zeng and R. Thampurun, Mater. Sci. Eng. A319 (2001) 893.

[10]. J. B. Pethica, R. Hutchings and W. C. Oliver, Phil. Mag. A48 (1983) 593.

[11]. J. L. Loubet, J. M. Georges, O. Marchesini and G. Meille, J. Trib. 106 (1984) 43.

[12]. M. F. Doerner and W. D. Nix, J. Mater. Res. 1 (1986) 601.

[13]. W. C. Oliver and G. M. Pharr, J. Mater. Res. 7 (1992) 1564.

[14]. G. M. Pharr, W. C. Oliver and F. R. Brotzen, J. Mater. Res. 7 (1992) 613.

[15]. S. P. Baker, Mater. Res. Soc. Symp. Proc. 308 (1993) 209.

[16]. A. E. Giannakopoulos, P. L. Larsson and R. Vestergaard, Int. J. Solids Struct. 31 (1994) 2679.

[17]. P. L. Larsson, A. E. Giannakopoulos, E. Söderlund, D. J. Rowcliffe and R. Vestergaard, Int. J. Solids Struct. 33 (1996) 221.

[18]. A. E. Giannakopoulos and P. L. Larsson, Mech. Mater. 25 (1997) 1.

[19]. K. Zeng, E. Söderlund, A. E. Giannakopoulos and D. J. Rowcliffe, Acta Mater. 44 (1996) 1127.

[20]. K. Zeng and D. J. Rowcliffe, Phil. Mag. A74 (1996) 1107.

[21]. B. J. Briscoe, K. S. Sebastian and M. J. Adams, J. Phys. D: Appl. Phys. 27 (1994) 1156.

[22]. A. C. Fischer-Cripps, Nanoindentation, Springer-Verlag, New York, 2002.

[23]. W. D. Nix, Mater. Sci. Eng. A234 (1997) 37.

[24]. W. D. Nix, Scr. Mater. 39 (1998) 545.

[25]. H. Kutomi, A. Daugela, W. W. Gerberich, H. Fujii and T. J. Wyrobek, Tribol. Int. 36 (2002) 255.

[26]. M. J. Turner, R. W. Clough, H. C. Martin and L. J. Topp, J. Aeronaut Sci. 23 (1956) 805.

[27]. J. S. Przemieniecki, Theory of Matrix Structural Analysis, McGraw-Hill, New York, 1968.

[28]. O. C. Zienkiewicz and Y. K. Cheung, The Finite Element Method in Structural and Continuum Mechanics, McGraw-Hill, London, 1967.

[29]. S. S. Rao, The Finite Element Method in Engineering, Pergamon, Oxford, 1989.

Chapter 2 Theories of Indentation

2.1. Basic Theories of Indentation

2.1.1. Hardness

Hardness is an old concept for characterizing the mechanical properties of a material. Historically, it can be divided into three main categories by different measuring methods: scratch hardness, indentation hardness and dynamic hardness [1].

Scratch hardness is the oldest form, which indicates the ability of one solid to be scratched by another. Though the scratch tests are convenient and simple, they involve complicated functions of elasticity, plasticity, and surface friction, which make it difficult to provide a scientific definition [2]. Indentation hardness is determined by the load and the corresponding size of the permanent impression formed in static indentations, while dynamic hardness is expressed in terms of either the height of rebound of the indenter, or the energy of impact and the size of the remaining indentation, which makes the number of the test variables beyond manageable level.

In 1881, Hertz [3] first postulated that an absolute value of hardness was the least value of the pressure beneath a spherical indenter, which was necessary to produce a permanent deformation at the center of the area of contact. Later, Auerbach [4], Meyer [5], and Hoyt [6] developed various measurements to remove some practical difficulties involved in Hertz's proposal. Now the generally accepted definition of hardness is expressed as:

$$H = \frac{P_{\max}}{A} \tag{2.1.1}$$

where H is the hardness; P_{max} is the maximum load applied to the indenter; and A is the projected contact area between the specimen and the indenter at P_{max}.

2.1.2. Depth Sensing Indentation

In conventional macro-indentation tests, the applied loads range from one to several hundred newtons. For micro-hardness testing, the applied loads are usually within a 10N order. Due to the increasing interests in the properties of thin film systems, nanoindentations are more commonly used nowadays since the typical loads are in a millinewton range and are measured with a resolution of several nanonewtons [2], whereas conventional indentation tests are inadequate to characterize the properties of thin film systems.

In the conventional macro/micro-indentation tests, the contact area is measured by using optical microscope after the load is removed. If this method is employed in nanoindentation tests, it would cause pronounced inaccuracy due to the following two reasons: 1) the contact areas (or the projections of them) are usually too small to be measured by normal optical microscope, or even, by scanning electron microscope (SEM); and 2) the recoveries of elastic deformation for some materials, at least for hard metals and ceramics, lead to the changes of contact areas during unloading. However, for depth sensing indentation (DSI), the load and the corresponding penetration depth are recorded throughout the whole indentation procedure with high resolution. This technique not only ensures a more accurate measurement of contact area but also provides information about elastic properties, plastic properties, and

time-dependent properties of the material tested.

The nanoindentation test procedure usually contains a few segments, including loading to a maximum load, holding at the maximum load, unloading to a pre-set load and another holding at a lower load for thermal drift correction, etc. The sequence for these segments can be programmed to meet the requirements of specific experiments. By using appropriate analysis methods, the elastic modulus and hardness of the specimen can be obtained through the interpretations of the load-penetration curves.

2.1.3. Interpretation of Load-Penetration Curves

A schematic representation of load-penetration curve during an indentation test is shown in Figure 2-1. The whole indentation process consists of a loading part (A→B) and an unloading one (B→C). P_{max} is the maximum load and h_{max} is the corresponding penetration depth of the indenter tip; h_0 is the final depth of the

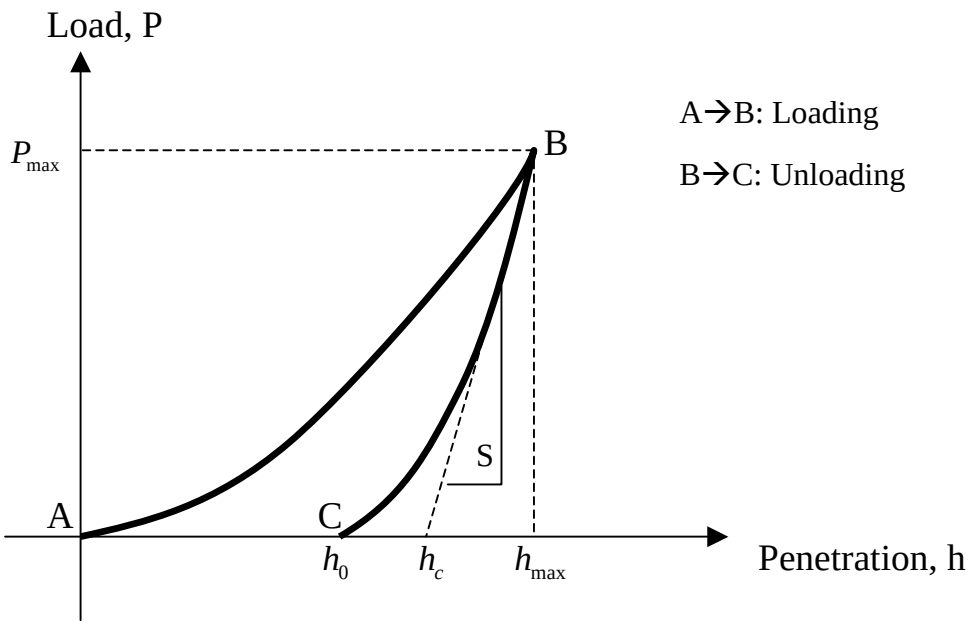

Fig. 2-1 Schematic representation of load versus penetration during indentation [2].

contact impression after unloading; h_c is the contact depth defined as the intercept of the initial unloading curve tangent at $P_{\max}$; and S represents the contact stiffness defined as $S = \frac{\partial P}{\partial h}$ at the maximum load.

In most cases the loading part involves plastic deformation as well as elastic deformation, while the initial part of unloading is usually considered elastic, which makes it possible to model the contact problem between the indenter and the specimen as a rigid punch indenting an elastic half-space.

This problem can be dated back to Boussinesq [7] and Hertz [3] in late 19th century. Hertz proposed a relationship between the load and the penetration depth in view of a semi-infinite elastic half-space indented by a rigid sphere as follows:

$$P = \frac{8\sqrt{R}}{3}\frac{E}{1-\nu^2}h^{3/2} \tag{2.1.2}$$

where P is the load applied; h is the penetration depth; R is the sphere radius; E and ν are the Young's modulus and Poisson's ratio of the material indented, respectively.

In 1939, based on Boussinesq's potential function method, Love [8] related the load to the penetration depth of an elastic half-space indented by a rigid cone:

$$P = \frac{2E\tan\theta}{\pi(1-\nu^2)}h^2 \tag{2.1.3}$$

where θ is the semi-included angle of the cone.

Later on, Sneddon proposed more generalized relations between the load and the penetration depth for the cases of elastic indentation with different geometries of indenter tips [9-11]. Generally, for many simple geometries of the indenters, the relation can be expressed as:

$$P = \alpha_0 h^m \tag{2.1.4}$$

where P is the load applied; h is the elastic displacement of the indenter; α_0 is a constant related to the indenter geometry, elastic modulus and Poisson's ratio of both the indenter and the specimen; and m is a constant only related to the geometry of the indenter and usually varies from 1 for a flat-ended cylindrical punch to 2 for a conical tip.

2.2. DSI Analysis Method

The fundamentals for interpreting the DSI data were first proposed by Bulychev and Alekhin [12]. They developed a DSI instrument operated in Vickers micro-hardness regime and established the basic assumptions that are generally employed to analyze the DSI data as follows:

1) The deformation upon unloading is predominantly elastic.

2) The elastic compliances of the indenter and specimens can be considered to be isotropic and can be linearly combined to produce a 'reduced modulus' of the contact, E_r:

$$\frac{1}{E_r} = \frac{(1-\nu_s^{\ 2})}{E_s} + \frac{(1-\nu_i^2)}{E_i} \tag{2.2.1}$$

where ν is the Poisson's ratio; and the subscripts s and i represent the specimen and the indenter, respectively.

3) The two assumptions above lead to the contact stiffness derived by using elasticity theory:

$$S = \frac{\partial P}{\partial h} = \frac{2}{\sqrt{\pi}} E_r \sqrt{A} \tag{2.2.2}$$

where E_r is the reduced modulus mentioned above; and A is the contact area.

Though originally derived for an elastic isotropic half-space indented by a conical indenter, this method can also be applied to spherical and cylindrical indenters [14]. Moreover, this method can be generalized to any indenter that can be described as a body of revolution of a smooth function [15]. Since the method is independent of indenter geometry, it is effective for deriving the elastic modulus of materials by non-flat punch tips. For Vickers and Berkovich indenters, finite element analysis showed that the deviations from their flat-ended equivalents were only about 1.2% and 3.4%, respectively [16].

2.2.1. Derivation of Young's Modulus

Based on indentation experiments and the model of Bulychev and Alekhin [12], Doerner and Nix [13] proposed the first comprehensive method to derive contact area A and reduced modulus E_r from DSI data.

They noticed that the initial portions of the unloading curves were linear for some materials, especially for metallic materials, leading to their assumption that the contact area remained constant during initial unloading. Thus, the elastic behavior of the unloading part could be modeled as an elastic solid indented by a flat punch and the contact stiffness can be derived from the slope of the initial portion of the unloading curve. Practically, a linear fitting to the upper one third of the unloading curve is used.

In addition, they postulated that the deformation was plastic in the region where materials were in contact with the indenter, while elastic deformation happened only outside the contact region during unloading. Therefore, they obtained the plastic deformation h_p by fitting a straight line to the upper portion of the unloading curve and extrapolating this line to the depth axis. Thus, contact area A can be derived to replace the final displacement h_0 shown in Figure 2-1 to improve accuracy.

Later, Oliver and Pharr [14] tested many materials and found that unloading curves followed a power law relationship:

$$P = \beta_0 (h - h_0)^m \tag{2.2.3}$$

where β_0 and m are constants; m ranges from about 1.2 to 1.6; and h_0 is residual depth shown in Figure 2-1. Their observation indicated that the contact area changed during unloading, even in the initial part. Taking into consideration the changing contact area during unloading, Oliver and Pharr [14] revised Doerner and Nix's method [13] by defining a contact depth:

$$h_c = h_{\max} - \varepsilon \frac{P_{\max}}{S} \tag{2.2.4}$$

where S is determined by analytically differentiating Eq.(2.2.3) and evaluating its value at the maximum indentation depth; and ε is a constant that equals 0.72 for a conical tip, 1.0 for a flat-ended punch and 0.75 for other tips that can be described as a parabolic revolution. It can be seen that Oliver and Pharr's model is identical to that of Doerner and Nix for the case of a flat ended punch ($\varepsilon = 1$); for any other cases, the contact depth based on Oliver and Pharr's approach will be larger than that of Doerner and Nix's approach. This is because Oliver and Pharr's method takes into account the

elastic recovery not only outside, but also inside the indentation contact area, whereas Doerner and Nix's method only considers the elastic recovery outside the contact area as shown in Figure 2-2 [17].

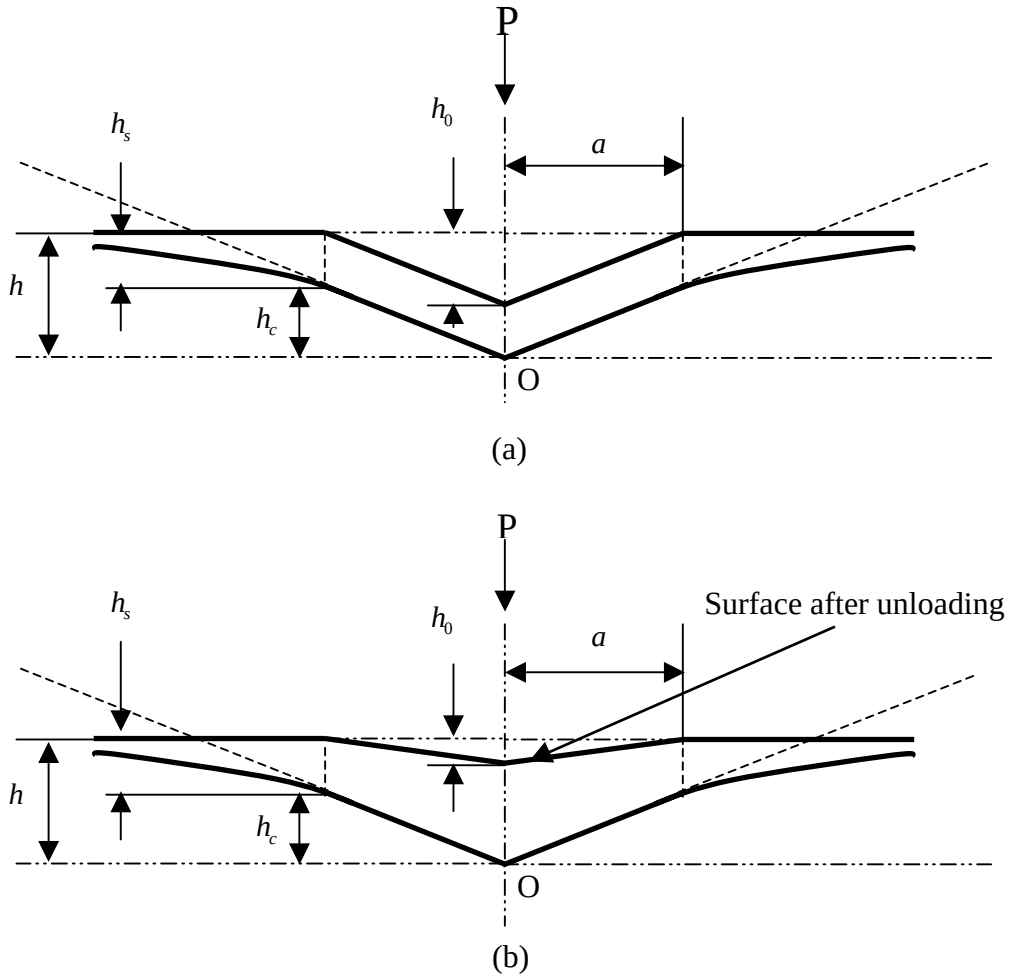

Fig. 2-2 Comparison of indentation penetration deformation between (a) Doerner and Nix's model, and (b) Oliver and Pharr's model.

Oliver and Pharr's method gives a more reasonable explanation on the unloading curve and is now widely used for deriving elastic modulus and hardness of materials by using nanoindentation techniques.

2.2.2. Theory of Wedge Indentation

Hill et al. [18] proposed a theoretical solution for a plastic material penetrated by a rigid frictionless wedge. This solution determines the deformation in the material squeezed out towards the surface, as well as the form of the lip. The basic assumptions of the theory are that: 1) the material is incompressible; and 2) the material is rigid until the yield strength is reached. They found that the average strain correlates with an equivalent reduction of area in a tensile test and increases with the angle of wedge indenter. For a semi-angle of 90º, the mean indentation pressure is about 2.6 times the pressure at 0º angle. They tested with lead indented by sharp steel indenters up to the largest semi-angle of 30º. Within this value, their theory works well. Furthermore, Dugdale [19] supported their theory by examining the impressions made in cold worked metals by wedge indenters of various angles.

Grunzweig et al. [20] presented a solution for a rough wedge following Hill's theory. The major difference is that the slip lines no longer meet the wedge face at 45º when the wedge is rough and the effect of friction is to raise the apparent indentation pressure by an amount that depends on the angle of the wedge and the coefficient of friction.

Based on the theory of indentation of a rigid perfectly-plastic solid, Tabor [21] showed that for ductile metals, the mean contact pressure was related to the yield strength of the material as:

$$p_m = CY \tag{2.2.5}$$

where p_m is the mean contact pressure; Y is the yield strength of the material

indented; and C is a constant whose value is about 3.

Mulhearn [22] subsequently showed that the mechanism of the indentation depends on the angle of the indenter. When the semi-angle of the indenter is less than 30º, the Hill's mechanism is obeyed well. However, in excess of 30º, a different mechanism sets in and becomes more and more important with increasing indenter angle. At large angles, the deformation can be approximated as a radial compression centered at or slightly below the bottom of the indenter. The dependence of different deformation mechanisms on the angle of a wedge indenter is probably due to the increasing importance of elastic deformation.

Later, based on the earlier work of Bishop et al. [23], Marsh [24] linked Mulhearn's mechanism of deformation at large angles to that of a cavity in an elastic-plastic material being expanded by an internal pressure, which was solved by Hill in 1950 [25]. Marsh [24] pointed out that the elastic modulus of the material was an important factor affecting the deformation mechanism. Highly elastic materials, i.e., the materials with a high value of the ratio of the elastic modulus to the yield strength E/Y, would be more amenable to radial compression and change more easily to a radial flow mechanism of deformation.

Using the same approach, Hirst and Howse [26] measured the indentation pressure for a range of materials by wedge indenters of different angles. They concluded that there were four main types of deformation and the regions as shown in Figure 2-3. Hill's mechanism for a plastic rigid solid can be applied only when the angle of the wedge is acute and the ratio of E/Y of the materials indented is high.

For less acute wedges or relatively more elastic materials, the mechanism is similar to that observed by Marsh and the indentation pressure follows the relation:

$$\frac{p_m}{Y} = M + N\ln(E/Y) \tag{2.2.6}$$

where M varies with wedge angle but N is approximately constant for a wedge whose angle exceeds 120°. For blunt wedges and highly elastic materials, elastic

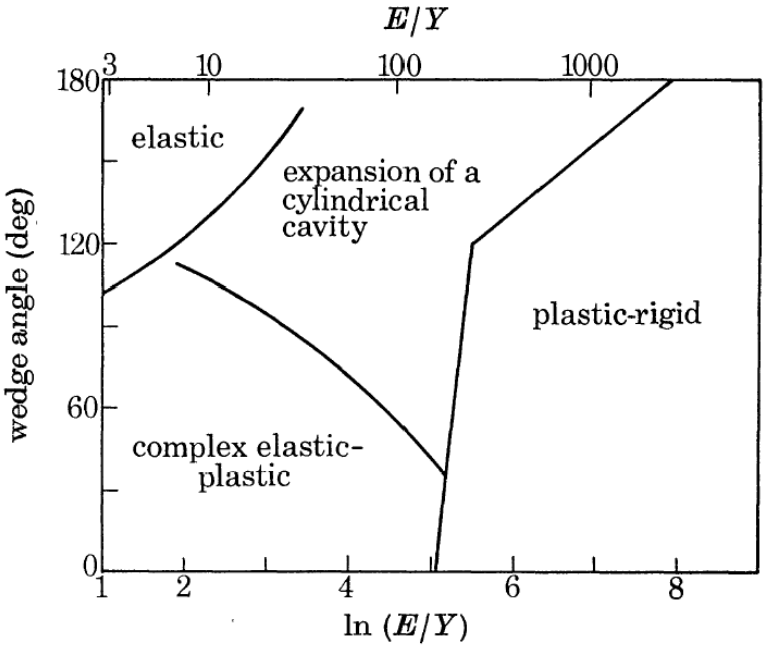

Fig. 2-3 Regions of operation of the different indentation mechanisms [26].

deformation predominates and the process can be modeled as an elastic solid indented by a rigid wedge. Thus, the pressure on the wedge at a point x is given by [27]:

$$p = \frac{E\cot\theta}{\pi(1-\nu^2)}\cosh^{-1}(a/x) \tag{2.2.7}$$

where x is the distance from the center of wedge indenter; a is the half-width of the indentation; and θ is the semi-angle of the wedge. The mean pressure, p_m, is given by:

$$p_m = \frac{E\cot\theta}{2(1-\nu^2)} \tag{2.2.8}$$

This elastic theory predicts the distribution of pressure and its mean value satisfactorily, except that the pressure within a narrow central band under the indenter falls below the infinite values predicted theoretically.

For blunt wedge indenters and materials having a low ratio of elastic modulus to yield strength, Johnson [28] suggested that the indentation pressure correlates with the single parameter $(E/Y)\tan\beta$. Here β is the angle of inclination of the indenter to the surface at the edge of the indentation. He then modified the expanding cavity model by replacing the cavity with an incompressible hemispherical core expended by an internal pressure as shown in Figure 2-4 and Figure 2-5.

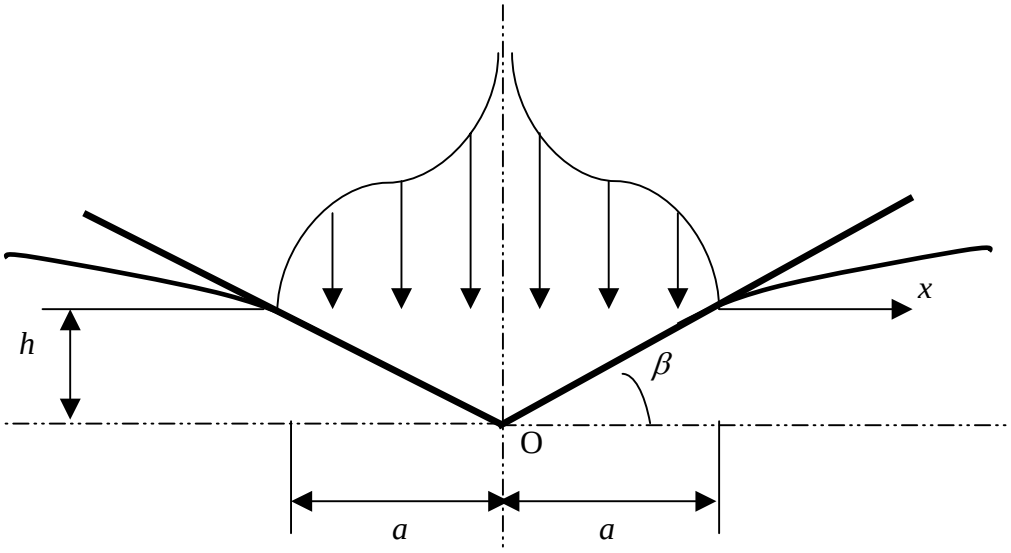

Fig. 2-4 Indentation of a surface by a rigid wedge [28].

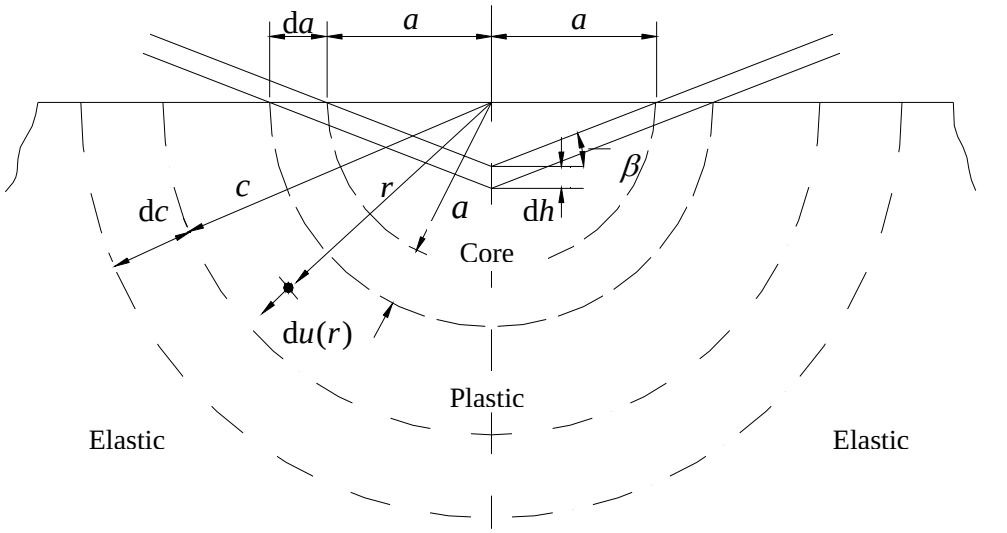

Fig. 2-5 Idealized model of a hemispherical plastic 'core' attached to the indenter surrounded by a symmetrically deformed region [28].

In this model, there is assumed to be a hydrostatic pressure within the core (Figure 2-5). The stresses and displacements outside the core are assumed to be radial symmetric, similar to that in an infinite elastic perfectly-plastic body with a cylindrical or spherical cavity under pressure. The elastic-plastic boundary lies at a radius of *c*, and the radial stress and displacement are given by Hill [25]:

$$\frac{\overline{p}}{Y} = -\left[\frac{\sigma_r}{Y}\right]_{r=a} = \frac{2}{\sqrt{3}}\left[\frac{1}{2} + \ln(\frac{c}{a})\right] \tag{2.2.9}$$

$$\frac{du(r)}{dc} = \frac{2}{\sqrt{3}}\frac{Y}{E}\left[\frac{5-4\nu}{2}\frac{c}{r} - \frac{3(1-2\nu)}{2}\frac{r}{c}\right] \tag{2.2.10}$$

Neglecting the compressibility of the core, we have:

$$\pi a du(a) = 2adh = 2a\tan\beta da \tag{2.2.11}$$

Put $r = a$ into Eq.(2.2.10) and notice $dc/da = c/a = \text{constant}$, thus we have:

$$\frac{4E}{\pi Y}\tan\beta = (5-4\nu)(c/a)^2 - 3(1-2\nu) \tag{2.2.12}$$

From Eq.(2.2.9) and Eq.(2.2.12), we obtain:

$$\frac{\bar{p}}{Y} = \frac{1}{\sqrt{3}}\left\{1 - \ln(5-4\nu) + \ln\left[\frac{4E}{\pi Y}\tan\beta + 3(1-2\nu)\right]\right\} \tag{2.2.13}$$

Although the relation was originally obtained within small strain and small value of β, it agrees with experimental results well up to $\beta = 30^{\circ}$. Therefore, this relation becomes one of the most widely accepted methods to the analysis of wedge indentation experiments.

References

[1]. H. O'Neill, Hardness Measurement of Metals and Alloys, Chapman & Hall, London, 1967.

[2]. A. C. Fischer-Cripps, Nanoindentation, Springer-Verlag, New York, 2002.

[3]. H. Hertz, J. Reine Angew. Math. 92 (1881) 156.

[4]. F. Auerbach, Ann. Phys. Chem. 43 (1891) 61.

[5]. E. Meyer, Phys. Z. 9 (1908) 66.

[6]. S. L. Hoyt, Trans. Am. Soc. Steel Treat. 6 (1924) 396.

[7]. J. Boussinesq, Applications des Potentiels a l'etude de Equilibre et du Mouvement des Solides Elastiques, Gauthier-Villars, Paris, 1885.

[8]. A. E. H. Love, Quart. J. Math. 10 (1939) 161.

[9]. I. N. Sneddon, Proc. Camb. Philo. Soc. 42 (1946) 29.

[10]. I. N. Sneddon, Proc. Camb. Philo. Soc. 44 (1948) 492.

[11]. I. N. Sneddon, Int. J. Eng. Sci. 3 (1965) 47.

[12]. S. I. Bulychev and V. P. Alekhin, Zavod. Lab. 53 (1987) 76.

[13]. M. F. Doerner and W. D. Nix, J. Mater. Res. 1 (1986) 601.

[14]. W. C. Oliver and G. M. Pharr, J. Mater. Res. 7 (1992) 1564.

[15]. G. M. Pharr, W. C. Oliver and F. R. Brotzen, J. Mater. Res. 7 (1992) 613.

[16]. R. B. King, Int. J. Solids Struct. 23 (1987) 1657.

[17]. S. P. Baker, Mater. Res. Soc. Symp. Proc. 308, 209 (1993).

[18]. R. Hill, E. H. Lee and S. J. Tupper, Proc. R. Soc. London A188 (1947) 273.

[19]. D. S. Dugdale, J. Mech. Phys. Solids 2 (1953) 14.

[20]. J. Grunzweig, I. M. Longman and N. J. Petch, J. Mech. Phys. Solids 2 (1954) 81.

[21]. D. Tabor, The Hardness of Metals, Clarendon Press, Oxford, 1951.

[22]. T. O. Mulhearn, J. Mech. Phys. Solids 7 (1959) 85.

[23]. R. F. Bishop, R. Hill and N. F. Mott, Proc. Phys. Soc. 57 (1945) 147.

[24]. D. M. Marsh, Proc. R. Soc. Lond. A, Math. Phys. Sci. 279 (1964) 420.

[25]. R. Hill, The Mathematical Theory of Plasticity, Clarendon Press, Oxford, 1950.

[26]. W. Hirst and M. G. J. W. Howse, Proc. R. Soc. Lond. A, Math. Phys. Sci. 311 (1969) 429.

[27]. I. N. Sneddon, Fourier Transforms, McGraw-Hill, New York, 1951.

[28]. K. L. Johnson, J. Mech. Phys. Solids 18 (1970) 115.

Chapter 3 Modeling

3.1. Methodology

The onset of delamination in a thin-film/substrate system generated by wedge indentation is of main interest. FEM is employed to understand the initiation and propagation of the interface delamination. Parametric studies are performed to show the effect of the interface adhesion properties on the initiation of the interface delamination. A method, which is capable of determining the interface adhesion properties, i.e., interface strength and interface energy, is proposed based on the results of the parametric studies and the limitation of this method is discussed.

3.2. Problem Formulation

The thin-film/substrate system is assumed to be subjected to wedge indentation. For simplicity, the wedge indenter is considered to be rigid and frictionless. In addition, it is assumed that the length to width ratio of the indenter is large, so that the plane-strain condition is applied.

Due to the symmetry of the system geometry, together with the assumption that the materials are isotropic, only half of the system is taken into consideration. Both the thin film and the substrate are assumed to be ductile enough so that the interface is the only site where delamination is allowed to occur. Besides, both the thin film and the substrate are modeled as elasto-plastic materials based on the J_2 theory, and the stress-strain relation is:

$$\varepsilon = \begin{cases} \sigma / E & \sigma \le \sigma_y \\ (\sigma_y / E)(\sigma / \sigma_y)^{1/N} & \sigma > \sigma_y \end{cases} \tag{3.2.1}$$

where σ_y is the yield strength; and N is the strain-hardening exponent. In addition, the viscosity of the substrate is included by using a power-law visco-plastic relationship:

$$\dot{\bar{\varepsilon}}^p = D\left[(\frac{\bar{\sigma}}{\sigma_e})^m - 1 \right] \tag{3.2.2}$$

where $\dot{\bar{\varepsilon}}^p$ is the effective plastic strain rate; $\bar{\sigma}$ is the effective stress; σ_e is the inviscid equivalent stress; D is a reference strain rate; and m is the strain rate sensitivity exponent.

During the interface delamination, the system is likely to undergo extensive plastic deformation; thus, the plastic zone can be considerably large. As a result, traditional criteria for crack growth based on a singular field become questionable when the crack tip is near or in the plastic zones [1-2]. Therefore, a traction-separation law (TSL) proposed by Tvergaard and Hutchinson is employed to describe the behavior of the interface [3-6]. The general idea is to describe fracture and damage process by a local stress-displacement dependent relationship [7].

Following the notation introduced by Tvergaard and Hutchinson [5], a typical form of TSL is shown in Figure 3-1, where δ_t, δ_n are the separations in tangential and normal directions, respectively; δ_t^c, δ_n^c are two constants that represent the critical separations in these two directions; λ_1 and λ_2 are the parameters to adjust the shape of TSL. The interface strength $\hat{\sigma}$ is the maximum separation stress under normal stressing, and the interface energy Γ_0 is the energy consumed by interface

separation per unit area in the delamination.

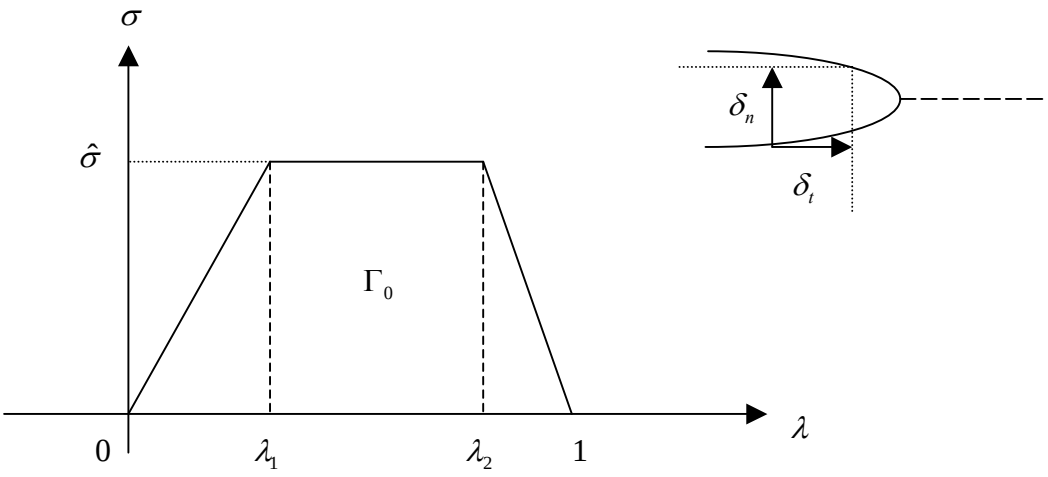

Fig. 3-1 Traction separation law.

A single dimensionless separation measure can be defined as:

$$\lambda = \sqrt{(\frac{\delta_n}{\delta_n^c})^2 + (\frac{\delta_t}{\delta_t^c})^2} \tag{3.2.3}$$

so that $\lambda = 1$ is the condition for the onset of delamination. The potential that dictates the interface behaviors is given by:

$$\phi = \phi(\delta_t, \delta_n) = \delta_n^c \int_0^\lambda \sigma(\bar{\lambda}) d\bar{\lambda} \tag{3.2.4}$$

The stress can be expressed as:

$$\sigma(\lambda) = \begin{cases} \dfrac{\hat{\sigma}}{\lambda_1}\lambda, & 0 \le \lambda \le \lambda_1 \\ \hat{\sigma}, & \lambda_1 \le \lambda \le \lambda_2 \\ \dfrac{\hat{\sigma}}{1-\lambda_2}(1-\lambda), & \lambda_2 \le \lambda \le 1 \end{cases} \tag{3.2.5}$$

so that the derivative of stress to λ can be deducted:

$$\sigma'(\lambda)=\begin{cases}\dfrac{\hat{\sigma}}{\lambda_1}, & 0\le\lambda\le\lambda_1\\ 0, & \lambda_1\le\lambda\le\lambda_2\\ -\dfrac{\hat{\sigma}}{1-\lambda_2}, & \lambda_2\le\lambda\le 1\end{cases} \tag{3.2.6}$$

Then the normal and tangential components of the surface traction are given by:

$$T_n=\phi_n=\frac{\partial\phi}{\partial\delta_n}=\frac{\partial\phi}{\partial\lambda}\frac{\partial\lambda}{\partial\delta_n}=\delta_n^c\sigma(\lambda)\frac{1}{2\lambda}\frac{2\delta_n}{(\delta_n^c)^2}=\frac{\sigma\delta_n}{\lambda\delta_n^c} \tag{3.2.7}$$

$$T_t=\phi_t=\frac{\partial\phi}{\partial\delta_t}=\frac{\partial\phi}{\partial\lambda}\frac{\partial\lambda}{\partial\delta_t}=\delta_n^c\sigma(\lambda)\frac{1}{2\lambda}\frac{2\delta_t}{(\delta_t^c)^2}=\frac{\sigma\delta_n^c\delta_t}{\lambda(\delta_t^c)^2} \tag{3.2.8}$$

The interface energy can be expressed as:

$$\Gamma_0=\hat{\sigma}\delta_n^c(1-\lambda_1+\lambda_2)/2 \tag{3.2.9}$$

Among all the parameters governing TSL, usually, the shape of TSL is relatively unimportant [8]. Thus, the interface strength $\hat{\sigma}$ and interface energy Γ_0 are the two most important parameters characterizing TSL, on which we focus in our parametric studies.

The advantage of using TSL is that one need not assume whether the thin film system is fully-bonded, fully-debonded or pre-cracked since it has been included in the interface delamination criterion inherently [1].

3.3. Finite Element Method

A fully implicit FEM is employed to analyze the onset of interface delamination in thin-film/substrate system during indentation tests. The whole thin-film/substrate system is divided into three substructures to be analyzed respectively: film, substrate and interface [1], as shown in Figure 3-2.

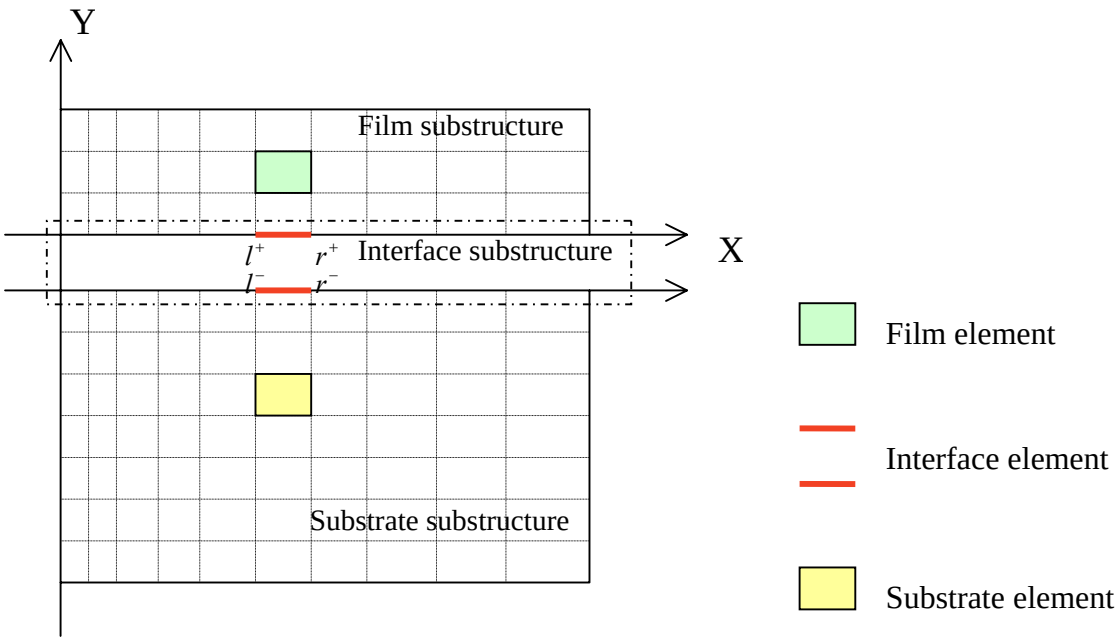

Fig. 3-2 Substructures of the thin-film/substrate system.

3.3.1. Governing Equation of Interface Substructure

For any element in the interface substructure (e.g. element 'l-r' in Figure 3-2), we define the relative nodal displacement vector as:

$$\begin{aligned} w^e &= \{\delta_t^l \ , \delta_n^l \ , \delta_t^r \ , \delta_n^r\}^T \\ &= \{u_{xl}^+ \ -u_{xl}^- \ , u_{yl}^+ \ -u_{yl}^- \ , u_{xr}^+ \ -u_{xr}^- \ , u_{yr}^+ \ -u_{yr}^-\}^T \end{aligned} \tag{3.3.1}$$

Correspondingly, we have the nodal force vector:

$$f^e = \{f_{xl} \ , f_{yl} \ , f_{xr} \ , f_{yr}\}^T \tag{3.3.2}$$

From the Principle of Virtual Work (Plane strain), we have:

$$\int_l \left(T^{n+1}\right)^T \delta u^e ds = \left(f^{e^{n+1}}\right)^T \delta w^e \tag{3.3.3}$$

where $u^e = \{u_x^+ - u_x^- \ , u_y^+ - u_y^-\}^T = \{\delta_t \ , \delta_n\}^T$; and $\delta u^e = N \delta w^e$, in which N is the shape function of the interface element; w^e is the relative nodal displacement; δu^e is the possible displacement of any point in the element. Substituting Eq.(3.3.1) and Eq.(3.3.2) into Eq.(3.3.3), we have:

$$\int_l \left(T^{n+1}\right)^T N\delta w^e ds = \left(f^{e^{n+1}}\right)^T \delta w^e$$

$$\int_l N^T T^{n+1} ds = f^{e^{n+1}}$$

For a small time step $\Delta\tau$ and small deformation:

$$\int_e N^T (T^n + \Delta T) ds = f^{e^n} + \Delta f \tag{3.3.4}$$

Notice that:

$$\begin{aligned} T &= \{T_t \ , T_n\}^T = \{\phi_t \ , \phi_n\}^T \\ \Delta T &= \dot{T}\Delta\tau \\ \dot{T} &= [\frac{d}{d\tau}(\phi_t) \ , \frac{d}{d\tau}(\phi_n)]^T = \{\phi_{tt}\dot{\delta}_t + \phi_{tn}\dot{\delta}_n \ , \phi_{tn}\dot{\delta}_t + \phi_{nn}\dot{\delta}_n\}^T \\ &= \begin{bmatrix} \phi_{tt} & \phi_{tn} \\ \phi_{tn} & \phi_{nn} \end{bmatrix} \begin{Bmatrix} \dot{\delta}_t \\ \dot{\delta}_n \end{Bmatrix} \\ &\triangleq \tilde{\phi}\ddot{u}^e \end{aligned}$$

where $u^e = Nw^e$; and $\dot{u}^e = N\dot{w}^e = N\frac{\Delta w^e}{\Delta\tau}$. Thus, $\dot{T} = \tilde{\phi}N\frac{\Delta w^e}{\Delta\tau}$, in which ϕ_{nn}, ϕ_{tt} and ϕ_{nt} can be calculated from Eq.(3.2.7) and Eq.(3.2.8):

$$\begin{aligned} \phi_{nn} &= \frac{\partial^2\phi}{\partial\delta_n^{\,2}} = \frac{\partial}{\partial\delta_n}(\frac{\partial\phi}{\partial\delta_n}) = \frac{\partial}{\partial\delta_n}(T_n) = \frac{1}{\delta_n^c}\frac{\partial}{\partial\delta_n}(\frac{\sigma(\lambda)}{\lambda}\delta_n) \\ &= \frac{1}{\delta_n^c}[\delta_n(\frac{\sigma'}{\lambda} - \frac{\sigma}{\lambda^2})\frac{1}{\lambda}\frac{\delta_n}{(\delta_n^c)^2} + \frac{\sigma}{\lambda}] \\ &= \frac{1}{\lambda\delta_n^c}[\sigma + \frac{1}{\lambda}(\frac{\delta_n}{\delta_n^c})^2(\sigma' - \frac{\sigma}{\lambda})] \end{aligned} \tag{3.3.5}$$

$$\begin{aligned} \phi_{tt} &= \frac{\partial^2\phi}{\partial\delta_t^{\,2}} = \frac{\partial}{\partial\delta_t}(\frac{\partial\phi}{\partial\delta_t}) = \frac{\partial}{\partial t}(T_t) = \frac{\delta_n^c}{(\delta_t^c)^2}\frac{\partial}{\partial\delta_t}(\frac{\sigma(\lambda)}{\lambda}\delta_t) \\ &= \frac{\delta_n^c}{(\delta_t^c)^2}[\frac{\sigma}{\lambda} + \delta_t(\frac{\sigma'}{\lambda} - \frac{\sigma}{\lambda^2})\frac{1}{\lambda}\frac{\delta_t}{(\delta_t^c)^2}] \\ &= \frac{\delta_n^c}{\lambda(\delta_t^c)^2}[\sigma + \frac{1}{\lambda}(\frac{\delta_t}{\delta_t^c})^2(\sigma' - \frac{\sigma}{\lambda})] \end{aligned} \tag{3.3.6}$$

$$\begin{aligned}\phi_{nt} &= \frac{\partial}{\partial \delta_t}(\frac{\partial \phi}{\partial \delta_n}) = \frac{\partial}{\partial \delta_t}(T_n) = \frac{\delta_n}{\delta_n^c}\frac{\partial}{\partial \delta_t}(\frac{\sigma(\lambda)}{\lambda}) \\ &= \frac{\delta_n}{\delta_n^c}[(\frac{\sigma'}{\lambda} - \frac{\sigma}{\lambda^2})\frac{1}{\lambda}\frac{\delta_t}{(\delta_t^c)^2}] \\ &= \frac{1}{\lambda^2}\frac{\delta_n}{\delta_n^c}\frac{\delta_t}{(\delta_t^c)^2}(\sigma' - \frac{\sigma}{\lambda})\end{aligned} \tag{3.3.7}$$

Plugging all the relations above into Eq.(3.3.4), we have:

$$\int_l (N^T T^n + N^T \tilde{\phi} N \frac{\Delta w^e}{\Delta \tau}\Delta\tau) ds = f^{e^n} + \Delta f^e$$
$$\int_l N^T \tilde{\phi} N ds \Delta w^e = f^{e^n} + \Delta f^e - \int N^T T^n ds$$

Using $\Delta f^e = f^{e^{n+1}} - f^{e^n}$, we have:

$$\int_e N^T \tilde{\phi} N ds \Delta w^e = f^{e^{n+1}} - \int N^T T^n ds \tag{3.3.8}$$

Rewriting in matrix form, we have the governing equation of the interface substructure:

$$\mathbf{K_{\delta\delta}\Delta w^e = f^{e^{n+1}} - \int N^T T^n ds} \tag{3.3.9}$$

Therefore during the iteration, with the initial data of δ_n and δ_t, the stiffness matrix $\mathbf{K_{\delta\delta}}$ and force vector $\mathbf{f^{e^{n+1}}}$ can be obtained.

$$\delta_n, \delta_t \Rightarrow \lambda, w^e \Rightarrow \sigma, \sigma' \Rightarrow T_n, T_t, \phi_{nn}, \phi_{tt}, \phi_{nt}, \dot{T} \Rightarrow \mathbf{K_{\delta\delta}} \Rightarrow$$

$$\mathbf{f^{e^{n+1}} = K_{\delta\delta}\Delta w^e - \int N^T T^n ds}$$

However, a special treatment is needed when $\delta_n = \delta_t = 0$, that is:

$$\delta_n = \delta_t = 0 \Rightarrow \lambda = 0 \Rightarrow T_n = T_t = 0 \Rightarrow$$

$$\begin{cases} \phi_{nn} = \dfrac{\hat{\sigma}}{\lambda_1}\dfrac{1}{\delta_n^c} \\ \phi_{tt} = \dfrac{\hat{\sigma}}{\lambda_1}\dfrac{\delta_n^c}{(\delta_t^c)^2} \\ \phi_{nt} = 0 \end{cases} \tag{3.3.10}$$

3.3.2. Governing Equation of Film and Substrate Substructures

Four-node linear elements are used with a finer mesh at the region near the indenter in both the film and substrate substructures.

From the Principle of the Virtual Work, we have:

$$\int_e \delta\varepsilon^T \sigma^{n+1} dV = \int_{\partial e} \delta u^T T^{n+1} ds \tag{3.3.11}$$

for each element, where $\delta\varepsilon = B\delta u^e$; $\delta u = N\delta u^e$; u^e is the displacement of nodes; N is the shape function; and δu is the possible displacement of any point in the element, so that:

$$\int_e \delta u^{eT} B^T \sigma^{n+1} dV = \int_{\partial e} \delta u^{eT} N^T T^{n+1} ds \tag{3.3.12}$$

$$\int_e B^T \sigma^{n+1} dV = \int_{\partial e} N^T T^{n+1} ds \tag{3.3.13}$$

For a small deformation step, we have:

$$\sigma^{n+1} = \sigma^n + \Delta\sigma$$

$$\Delta\sigma = D_{ep}\Delta\varepsilon$$

$$\Delta\varepsilon = B\Delta u^e$$

Plugging above equations into Eq.(3.3.13), we have:

$$\int_e B^T(\sigma^n + \Delta\sigma) dV = \int_{\partial e} N^T T^{n+1} ds$$

$$\int_e B^T D_{ep} B\Delta u^e dV = \int_{\partial e} N^T T^{n+1} ds - \int_e B^T \sigma^n dV$$

$$K^{ep}\Delta u^e = \int_{\partial e} N^T T^{n+1} ds - \int_e B^T \sigma^n dV$$

Considering all the elements in the substructure, we have:

$$\sum K^{ep}\Delta u^e = \sum \left(\int_{\partial e} N^T T^{n+1} ds - \int_e B^T \sigma^n dV\right) \tag{3.3.14}$$

Rewriting in matrix form, we have:

$$\mathbf{K\Delta u} = \mathbf{f^{n+1}} - \mathbf{f^n} \tag{3.3.15}$$

To use interface boundary condition, we make the following classification on the degrees of freedom (DOFs) for the film and the substrate:

I) For the film, all the DOFs are divided into 3 types:

i) DOFs belonging to the interface substructure are designated with subscript '*if*';

ii) DOFs belonging to the loading area (i.e., those will contact with the indenter during indentation process) are designated with subscript '*lf*';

iii) All the other DOFs are designated with subscript '*nf*';

II) For the substrate, all the DOFs are divided into 2 types:

i) DOFs belonging to the interface substructure are designated with subscript '*is*';

ii) All the other DOFs are designated with subscript '*ns*'.

Then Eq.(3.3.15) becomes:

$$\begin{bmatrix} K_{nn} & K_{ni} & K_{nl} \\ K_{ni} & K_{ii} & K_{il} \\ K_{nl} & K_{il} & K_{ll} \end{bmatrix}_f \begin{Bmatrix} \Delta u_{nf} \\ \Delta u_{if} \\ \Delta u_{lf} \end{Bmatrix} = \begin{Bmatrix} f_n^{n+1} \\ f_i^{n+1} \\ f_l^{n+1} \end{Bmatrix}_f - \begin{Bmatrix} f_n^n \\ f_i^n \\ f_l^n \end{Bmatrix}_f \tag{3.3.16}$$

for the film substructure, and becomes:

$$\begin{bmatrix} K_{nn} & K_{ni} \\ K_{in} & K_{ii} \end{bmatrix}_s \begin{Bmatrix} \Delta u_{ns} \\ \Delta u_{is} \end{Bmatrix} = \begin{Bmatrix} f_n^{n+1} \\ f_i^{n+1} \end{Bmatrix}_s - \begin{Bmatrix} f_n^n \\ f_i^n \end{Bmatrix}_s \tag{3.3.17}$$

for the substrate substructure. Through the condensation of the degree of freedom, we have:

$$\begin{bmatrix} K_{11} & K_{12} \\ K_{21} & K_{22} \end{bmatrix}_f \begin{Bmatrix} \Delta u_{if} \\ \Delta u_{ls} \end{Bmatrix} = \begin{Bmatrix} f_n^{n+1} - f_n^n \\ f_i^{n+1} - f_i^n \end{Bmatrix}_f \tag{3.3.18}$$

for the film substructure, and:

$$\left[K_{11}\right]_s \{\Delta u_{is}\} = \{f_i^{n+1} - f_i^n\}_s \tag{3.3.19}$$

for the substrate substructure.

Taking the force balance and compatible conditions into consideration, we have:

$$f_{if}^{n+1} = -f_{is}^{n+1}, f_{if}^n = -f_{is}^n$$

$$\Delta u_{if} - \Delta u_{is} = \Delta\delta \Rightarrow \begin{cases} \Delta u_{if} = \Delta u_m + \Delta\delta/2 \\ \Delta u_{is} = \Delta u_m - \Delta\delta/2 \end{cases} \tag{3.3.20}$$

where Δu_m is the average of Δu_{if} and Δu_{is}. Substituting the force balance and compatible conditions into Eq.(3.3.18) and Eq.(3.3.19), we have:

$$\begin{bmatrix} K_{11} & K_{12} \\ K_{21} & K_{22} \end{bmatrix}_f \begin{Bmatrix} \Delta u_m \\ \Delta u_l \end{Bmatrix}_f + \begin{bmatrix} K_{11} & 0 \\ K_{21} & 0 \end{bmatrix}_f \begin{Bmatrix} \Delta\delta/2 \\ 0 \end{Bmatrix}_f = \begin{Bmatrix} \Delta f_i \\ \Delta f_l \end{Bmatrix}$$

$$\left[K_{11}\right]_s \{\Delta u_m\} - \left[K_{11}\right]_s \{\Delta\delta/2\} = \{\Delta f_i\}$$

Namely:

$$\begin{cases} K_{11f}\Delta u_m + K_{12f}\Delta u_l + K_{11f}\Delta\delta/2 = \Delta f_{if} \\ K_{21f}\Delta u_m + K_{22f}\Delta u_l + K_{12f}\Delta\delta/2 = \Delta f_{lf} \\ K_{11s}\Delta u_m - K_{11s}\Delta\delta/2 = \Delta f_{is} = -\Delta f_{if} \end{cases}$$

$$\Rightarrow \begin{cases} (K_{11f} + K_{11s})\Delta u_m + (K_{11f} - K_{11s})\Delta\delta/2 + K_{12f}\Delta u_l = 0 \\ K_{12f}\Delta u_m + K_{21f}\Delta u_l + K_{12f}\Delta\delta/2 = \Delta f_l^n \\ (K_{11f} - K_{11s})\Delta u_m + (K_{11f} + K_{11s})\Delta\delta/2 + K_{12f}\Delta u_l = 2\Delta f_{if} \end{cases}$$

Rewriting in matrix form, we have:

$$\begin{bmatrix} K_{11f} + K_{11s} & K_{12f} & K_{11f} - K_{11s} \\ K_{12f} & K_{22f} & K_{12f} \\ K_{11f} - K_{11s} & K_{12f} & K_{11f} + K_{11s} \end{bmatrix} \begin{Bmatrix} \Delta u_m \\ \Delta u_l \\ \Delta\delta/2 \end{Bmatrix} = \begin{Bmatrix} 0 \\ f_l^n \\ 2\Delta f_{if} \end{Bmatrix} \tag{3.3.21}$$

Notice that $K_{\delta\delta}\Delta\delta = \Delta f_{is} = -\Delta f_{if}$ in the interface substructure, we have:

$$2\Delta f_{if} = -4K_{\delta\delta}\Delta\delta/2 \tag{3.3.22}$$

so that we can obtain the final governing equation by substituting Eq.(3.3.22) into Eq.(3.3.21):

$$\begin{bmatrix} K_{11f}+K_{11s} & K_{12f} & K_{11f}-K_{11s} \\ K_{12f} & K_{22f} & K_{12f} \\ K_{11f}-K_{11s} & K_{12f} & K_{11f}+K_{11s}+4K_{\delta\delta} \end{bmatrix} \begin{Bmatrix} \Delta u_m \\ \Delta u_l \\ \Delta\delta/2 \end{Bmatrix} = \begin{Bmatrix} 0 \\ \Delta f_l^n \\ 0 \end{Bmatrix} \qquad (3.3.23)$$

3.3.3. Boundary Conditions

The Y-Axis of the mesh (see Figure 3-2) is fixed in horizontal direction but free to move vertically. The nodes in the contact region between the indenter and the thin-film/substrate system are constrained to move with the indenter, but free to move along the surface of the indenter. Thus the boundary conditions can be summarized as:

$$u(y) = 0 \qquad x = 0 \qquad (3.3.24)$$

$$v(x) = 0 \qquad y = 0 \qquad (3.3.25)$$

$$v(x) = -\left(\delta - \frac{x}{\tan\theta}\right) \text{ in the contact region} \qquad (3.3.26)$$

where δ is the indentation depth; and θ is the included semi-angle of the indenter, which is taken to be 60º in the simulations.

3.4. Algorithm for Numerical Integration of Constitutive Relation

FEM has been successfully used to analyze structures and processes exhibiting non-linear, inelastic behavior, which has been defined in terms of stress and a set of state variables in most inelastic constitutive models. Typically, the solutions to these non-linear problems are performed incrementally and those to the inelastic constitutive equations are obtained by numerical integration. Several methods have been proposed to integrate the elastoplastic constitutive equations [9-12]. In this section, we will briefly illustrate the algorithm proposed by Aravas [13] with respect

to our special case.

In our case, strain increments are several times the size of the yield surface in strain space. Therefore, the backward Euler method for the integration of elastoplastic constitutive equations leads to better accuracy [10].

In this method, strains and rotations of finite size are considered and Newton's method is employed to solve the equation. The stiffness matrix used in the solution of the overall equations is gained by consistent linearization of the elastoplastic equations so that the quadratic convergence of the iterative solution schemes can be obtained [14-15].

3.4.1. Constitutive Equations and Backward Euler Method

The integration of the constitutive equations is carried out at the integration points, where the strain increment $\Delta\boldsymbol{\varepsilon}$ is given. Our task is to calculate the stress and state variables at the end of the increment with the assumption that the solution is known at the start of each increment.

3.4.1.1. Strain Rate Decomposition

Following the algorithm proposed by Aravas [13], we assume the following strain rate decomposition:

$$d\boldsymbol{\varepsilon} = d\boldsymbol{\varepsilon}^e + d\boldsymbol{\varepsilon}^p \tag{3.4.1}$$

where $d\boldsymbol{\varepsilon}$ is a differential change in the total strain; $d\boldsymbol{\varepsilon}^e$ is a differential change in the elastic strain; and $d\boldsymbol{\varepsilon}^p$ is a differential change in the inelastic (plastic) strain.

The integrated form of Eq.(3.4.1) is:

$$\boldsymbol{\varepsilon} = \boldsymbol{\varepsilon}^e + \boldsymbol{\varepsilon}^p \tag{3.4.2}$$

where $\boldsymbol{\varepsilon}, \boldsymbol{\varepsilon}^e$, and $\boldsymbol{\varepsilon}^p$ are summations of corresponding values at the start of the increment and the incremental values associated with that increment.

For case of linear elasticity, we have:

$$\boldsymbol{\sigma} = \mathbf{C}^{\mathbf{e}} : \boldsymbol{\varepsilon} \tag{3.4.3}$$

where $\boldsymbol{\sigma}$ is the Cauchy (true) stress; and $\mathbf{C}^{\mathbf{e}}$ is the fourth-order elasticity tensor. For isotropic case:

$$C^e_{ijkl} = 2G\delta_{ik}\delta_{jl} + (K - \frac{2}{3}G)\delta_{ij}\delta_{kl} \tag{3.4.4}$$

where G and K are the elastic shear modulus and bulk modulus, respectively; and δ_{ij} is the Kronecker delta.

During the integration of the elastoplastic equations, if the total elastic strain $\boldsymbol{\varepsilon}^e_{t+\Delta t}$ is known, the total stress is updated by:

$$\boldsymbol{\sigma}_{t+\Delta t} = \mathbf{C}^{\mathbf{e}} : \boldsymbol{\varepsilon}^e_{t+\Delta t} \tag{3.4.5}$$

If we introduce an elastic predictor, $\boldsymbol{\sigma}^e = \mathbf{C}^{\mathbf{e}} : (\boldsymbol{\varepsilon}^e_t + \Delta\boldsymbol{\varepsilon})$ as proposed by Aravas [13], Eq.(3.4.5) becomes:

$$\boldsymbol{\sigma}_{t+\Delta t} = \boldsymbol{\sigma}^e - \mathbf{C}^{\mathbf{e}} : \Delta\boldsymbol{\varepsilon}^p \tag{3.4.6}$$

The subscript t is the time at the start of the increment and $t + \Delta t$ is the time at the end of the increment. $\boldsymbol{\varepsilon}^e_t$ is the elastic strain at the start of the increment.

3.4.1.2. Basic Assumptions

The basic variables used are: p, q, and H^α, where p is the hydrostatic

stress (the first invariant of the stress tensor) $p = -\frac{1}{3}\boldsymbol{\sigma} : \mathbf{I}$; q is the equivalent stress (the second invariant of the stress tensor) $q = (\frac{3}{2}\mathbf{s} : \mathbf{s})^{1/2}$; and $H^{\alpha}, \alpha = 1, 2, 3 \cdots n$ is a set of scalar state variables. Here $\mathbf{I}$ is the second-order identity tensor, and $\mathbf{s}$ is the stress deviator, $s_{ij} = \sigma_{ij} + \delta_{ij} p$. The basic assumptions used are:

Assumption 1: Based on J_2 theory, the yield function only involves p, q, and H^{α} and is given by:

$$\Phi(\boldsymbol{\sigma}, H^{\alpha}) = \Phi(p_{t+\Delta t}, q_{t+\Delta t}, H^{\alpha}_{t+\Delta t}) = 0 \tag{3.4.7}$$

Assumption 2: The flow rule can be given by:

$$d\boldsymbol{\varepsilon}^{p} = d\Lambda \frac{\partial g}{\partial \boldsymbol{\sigma}} \tag{3.4.8}$$

where $d\Lambda$ is a positive scalar; and $g = g(p, q, H^{\alpha})$ is the flow potential.

Assumption 3: The evolution of the state variables is given by:

$$\Delta H^{\alpha} = \bar{h}^{\alpha}(\Delta\boldsymbol{\varepsilon}^{p}, \boldsymbol{\sigma}_{t+\Delta t}, H^{\beta}_{t+\Delta t}) \tag{3.4.9}$$

where $\bar{h}^{\alpha}$ should be homogeneous of degree one in $d\boldsymbol{\varepsilon}^{P}$ for rate independent materials.

3.4.1.3. Derivation of Governing Equations

Notice that $(\frac{\partial p}{\partial \sigma})_{ij} = \frac{\partial p}{\partial \sigma_{ij}} = -\frac{1}{3}\delta_{ij}$ and $(\frac{\partial q}{\partial \sigma})_{ij} = \frac{\partial q}{\partial \sigma_{ij}} = \frac{\partial (\frac{1}{3} s_{ij} s_{ij})^{1/2}}{\partial \sigma_{ij}} = \frac{3}{2}\frac{s_{ij}}{q}$,

Eq.(3.4.8) can be written as:

$$d\boldsymbol{\varepsilon}^{p} = d\Lambda[-\frac{1}{3}(\frac{\partial g}{\partial p})_{t+\Delta t}\mathbf{I} + \frac{2}{3}(\frac{\partial g}{\partial q})_{t+\Delta t}(\frac{\mathbf{s}}{q})_{t+\Delta t}]$$

Introduce $\Delta\varepsilon_p = -d\Lambda(\frac{\partial g}{\partial p})_{t+\Delta t}$ and $\Delta\varepsilon_q = d\Lambda(\frac{\partial g}{\partial q})_{t+\Delta t}$ and notice $\mathbf{n} = \frac{3}{2}\frac{\mathbf{s}}{q}$, thus we obtain:

$$\Delta\varepsilon_p(\frac{\partial g}{\partial q})_{t+\Delta t}+\Delta\varepsilon_q(\frac{\partial g}{\partial p})_{t+\Delta t}=-d\Lambda[(\frac{\partial g}{\partial p})(\frac{\partial g}{\partial q})]_{t+\Delta t}+d\Lambda[(\frac{\partial g}{\partial q})(\frac{\partial g}{\partial p})]_{t+\Delta t}=0 \quad (3.4.10)$$

The flow rule Eq.(3.4.8) can be written as:

$$\Delta\boldsymbol{\varepsilon}^p=\frac{1}{3}\Delta\varepsilon_p\mathbf{I}+\Delta\varepsilon_q\mathbf{n}_{t+\Delta t} \quad (3.4.11)$$

Substituting Eq.(3.4.11) into Eq.(3.4.4), we obtain:

$$\mathbf{C}^{\mathbf{e}}:\Delta\boldsymbol{\varepsilon}^p=K\Delta\varepsilon_p\mathbf{I}+2G\Delta\varepsilon_q\mathbf{n}_{t+\Delta t} \quad (3.4.12)$$

Meanwhile, from the definition of the stress deviator $\mathbf{s}$, stress can be written as:

$$\boldsymbol{\sigma}_{t+\Delta t}=-p_{t+\Delta t}\mathbf{I}+\mathbf{s}_{t+\Delta t}=-p_{t+\Delta t}\mathbf{I}+\frac{2}{3}q_{t+\Delta t}\mathbf{n}_{t+\Delta t} \quad (3.4.13)$$

Thus, Eq.(3.4.6) can be rewritten as:

$$\boldsymbol{\sigma}_{t+\Delta t}=\boldsymbol{\sigma}^e-\mathbf{C}^{\mathbf{e}}:\Delta\boldsymbol{\varepsilon}^p=\boldsymbol{\sigma}^e-K\Delta\varepsilon_p\mathbf{I}-2G\Delta\varepsilon_q\mathbf{n}_{t+\Delta t} \quad (3.4.14)$$

Projecting the predictor $\boldsymbol{\sigma}^e$ on to $\mathbf{I}$ and $\mathbf{n}_{t+\Delta t}$, $\boldsymbol{\sigma}^e=-p^e\mathbf{I}+q^e\mathbf{n}_{t+\Delta t}$, we obtain:

$$\boldsymbol{\sigma}_{t+\Delta t}=-p^e\mathbf{I}+q^e\mathbf{n}_{t+\Delta t}-K\Delta\varepsilon_p\mathbf{I}-2G\Delta\varepsilon_q\mathbf{n}_{t+\Delta t} \quad (3.4.15)$$

Compare Eq.(3.4.15) with Eq.(3.4.13), and notice that $\mathbf{n}_{t+\Delta t}=\frac{3}{2q^e}\mathbf{s}^e$, thus we have:

$$p_{t+\Delta t}=p^e+K\Delta\varepsilon_p \quad (3.4.16)$$

$$q_{t+\Delta t}=q^e-3G\Delta\varepsilon_q \quad (3.4.17)$$

Then the evolution of the state variables can be expressed as:

$$\Delta H^\alpha=h^\alpha(\Delta\varepsilon_p,\Delta\varepsilon_q,p_{t+\Delta t},q_{t+\Delta t},H^\beta_{t+\Delta t}) \quad (3.4.18)$$

where $h^\alpha(\Delta\varepsilon_p,\Delta\varepsilon_q,p_{t+\Delta t},q_{t+\Delta t},H^\beta_{t+\Delta t})=\bar{h}^\alpha(\frac{1}{3}\Delta\varepsilon_p\mathbf{I}+\Delta\varepsilon_q\mathbf{n}_{t+\Delta t},-p_{t+\Delta t}\mathbf{I}+\frac{2}{3}q_{t+\Delta t}\mathbf{n}_{t+\Delta t},H^\beta_{t+\Delta t})$.

Therefore, the problem of integrating the elastoplastic equations reduces to the solution of the following set of non-linear equations:

$$\Delta\varepsilon_p(\frac{\partial g}{\partial q})_{t+\Delta t}+\Delta\varepsilon_q(\frac{\partial g}{\partial p})_{t+\Delta t}=0$$

$$\Phi(p_{t+\Delta t},q_{t+\Delta t},H^\alpha_{t+\Delta t})=0$$

$$p_{t+\Delta t} = p^e + K\Delta\varepsilon_p$$

$$q_{t+\Delta t} = q^e - 3G\Delta\varepsilon_q$$

$$\Delta H^\alpha = h^\alpha(\Delta\varepsilon_p, \Delta\varepsilon_q, p_{t+\Delta t}, q_{t+\Delta t}, H^\beta_{t+\Delta t})$$

For simplicity, we neglect subscript $t+\Delta t$ in the following subsections.

3.4.2. Newton's Method for Non-Linear System

3.4.2.1. Newton's Equation

Newton's method is employed to solve the non-linear equations mentioned above. There are five unknowns, $\Delta\varepsilon_p, \Delta\varepsilon_q, p, q, H^\beta$, and five equations. It is noted that $p, q,$ and H^β can be explicitly expressed by $\Delta\varepsilon_p$ and $\Delta\varepsilon_q$. Thus, there are only two primary unknowns, $\Delta\varepsilon_p$ and $\Delta\varepsilon_q$ and two basic equations Eq.(3.4.10) and Eq.(3.4.7).

Taking c_p and c_q as the corrections for $\Delta\varepsilon_p$ and $\Delta\varepsilon_q$, the Newton's equations for Eq.(3.4.10) and Eq.(3.4.7) can be expressed as:

$$A_{11}c_p + A_{12}c_q = b_1 \tag{3.4.19}$$

$$A_{21}c_p + A_{22}c_q = b_2 \tag{3.4.20}$$

The values of the coefficients of Eq.(3.4.19) and Eq.(3.4.20) are given in Appendix 1.

At the beginning of the integration, we take the initial data of $\Delta\varepsilon_p$ and $\Delta\varepsilon_q$, then c_p and c_q can be obtained by solving Eq.(3.4.19) and Eq.(3.4.20). Afterwards, $\Delta\varepsilon_p$ and $\Delta\varepsilon_q$ are updated through:

$$\Delta\varepsilon_p{}^{k+1} \to \Delta\varepsilon_p{}^{k} + c_p, \quad \Delta\varepsilon_q{}^{k+1} \to \Delta\varepsilon_q{}^{k} + c_q$$

3.4.2.2. Properties of Linearization Moduli

In the above Newton's iteration, the size of the linear system is very important for high resolution. The efficiency of the solution solvers depends much on the symmetric property of the matrix of coefficients. In order to explore the property, we need to calculate the 'linearization moduli' $\mathbf{D} = (\frac{\partial \boldsymbol{\sigma}}{\partial \boldsymbol{\varepsilon}})_{t+\Delta t}$.

By using Eq.(3.4.11), Eq.(3.4.5) can be written as:

$$\boldsymbol{\sigma}_{t+\Delta t} = \mathbf{C}^e : \boldsymbol{\varepsilon}^e_{t+\Delta t} = \mathbf{C}^e : (\boldsymbol{\varepsilon} - \boldsymbol{\varepsilon}^p_t - \frac{1}{3}\Delta\varepsilon_p \mathbf{I} - \Delta\varepsilon_q \mathbf{n}) \tag{3.4.21}$$

where $\boldsymbol{\varepsilon}^p_t$ is the plastic strain at the start of the increment. Taking derivative at both sides of above equations, we obtain:

$$\partial\boldsymbol{\sigma} = \mathbf{C}^e : (\partial\boldsymbol{\varepsilon} - \frac{1}{3}\partial\Delta\varepsilon_p \mathbf{I} - \partial\Delta\varepsilon_q \mathbf{n} - \Delta\varepsilon_q \frac{\partial \mathbf{n}}{\partial \boldsymbol{\sigma}} : \partial\boldsymbol{\sigma}) \tag{3.4.22}$$

in which $\frac{\partial \mathbf{n}}{\partial \boldsymbol{\sigma}} = \frac{\partial}{\partial \boldsymbol{\sigma}}(\frac{3}{2q}\mathbf{s}) = \frac{3}{2q}\frac{\partial \mathbf{s}}{\partial \boldsymbol{\sigma}} - \frac{3}{2}\mathbf{s}\frac{1}{q^2}\frac{\partial q}{\partial \boldsymbol{\sigma}} = \frac{1}{q}(\frac{3}{2}\mathbf{J} - \frac{1}{2}\mathbf{I}\otimes\mathbf{I} - \mathbf{n}\otimes\mathbf{n})$, where $J_{ijkl} = \delta_{ik}\delta_{jl}$ is the fourth-order identity tensor with Cartesian components. Taking derivative of Eq.(3.4.10) and Eq.(3.4.7), we obtain:

$$\partial\Delta\varepsilon_p \frac{\partial g}{\partial q} + \Delta\varepsilon_p[(\frac{\partial^2 g}{\partial p \partial q}\frac{\partial p}{\partial \boldsymbol{\sigma}} + \frac{\partial^2 g}{\partial q^2}\frac{\partial q}{\partial \boldsymbol{\sigma}}) : \partial\boldsymbol{\sigma} + \sum_{\alpha=1}^{n}\frac{\partial^2 g}{\partial q \partial H^\alpha}\partial H^\alpha] + \partial\Delta\varepsilon_q \frac{\partial g}{\partial p}$$

$$+\Delta\varepsilon_q[(\frac{\partial^2 g}{\partial p^2}\frac{\partial p}{\partial \boldsymbol{\sigma}} + \frac{\partial^2 g}{\partial p \partial q}\frac{\partial q}{\partial \boldsymbol{\sigma}}) : \partial\boldsymbol{\sigma} + \sum_{\alpha=1}^{n}\frac{\partial^2 g}{\partial p \partial H^\alpha}\partial H^\alpha] = 0 \tag{3.4.23}$$

$$(\frac{\partial \Phi}{\partial p}\frac{\partial p}{\partial \boldsymbol{\sigma}} + \frac{\partial \Phi}{\partial q}\frac{\partial q}{\partial \boldsymbol{\sigma}}) : \partial\boldsymbol{\sigma} + \sum_{\alpha=1}^{n}\frac{\partial \Phi}{\partial H^\alpha}\partial H^\alpha = 0 \tag{3.4.24}$$

Using Eq.(3.4.18), the above equations can be expressed in terms of $\partial\boldsymbol{\sigma}$:

$$A_{11}\partial\Delta\varepsilon_p + A_{12}\partial\Delta\varepsilon_q = (B_{11}\mathbf{I} + B_{12}\mathbf{n}) : \partial\boldsymbol{\sigma} \tag{3.4.25}$$

$$A_{21}\partial\Delta\varepsilon_p + A_{22}\partial\Delta\varepsilon_q = (B_{21}\mathbf{I} + B_{22}\mathbf{n}) : \partial\boldsymbol{\sigma} \tag{3.4.26}$$

Solving the above two equations gives:

$$\partial\Delta\varepsilon_p = (m_{pl}\mathbf{I} + m_{pn}\mathbf{n}) : \partial\boldsymbol{\sigma} \tag{3.4.27}$$

$$\partial\Delta\varepsilon_q = (m_{ql}\mathbf{I} + m_{qn}\mathbf{n}) : \partial\boldsymbol{\sigma} \tag{3.4.28}$$

The values of the coefficients of Eq.(3.4.25) to Eq.(3.4.28) are given in Appendix 2.

Substituting above equations into Eq.(3.4.22), we obtain:

$$\partial\boldsymbol{\sigma} = (\mathbf{J} + \mathbf{C}^e : \mathbf{M})^{-1} : \mathbf{C}^e : \partial\boldsymbol{\varepsilon} = (\mathbf{C}^{e-1} + \mathbf{M})^{-1} : \partial\boldsymbol{\varepsilon} \tag{3.4.29}$$

Thus, we have:

$$\mathbf{D} = (\frac{\partial\boldsymbol{\sigma}}{\partial\boldsymbol{\varepsilon}})_{t+\Delta t} = (\mathbf{M} + \mathbf{C}^{e-1})^{-1} \tag{3.4.30}$$

where $\mathbf{D}$ is symmetric when $\frac{1}{3}m_{pn} = m_{ql}$.

3.5. A Typical Case

In the present simulations, all the parameters involved in governing equations and constitutive relations are normalized by the yield strength of the film, $\sigma_{yf} = 200\text{MPa}$,

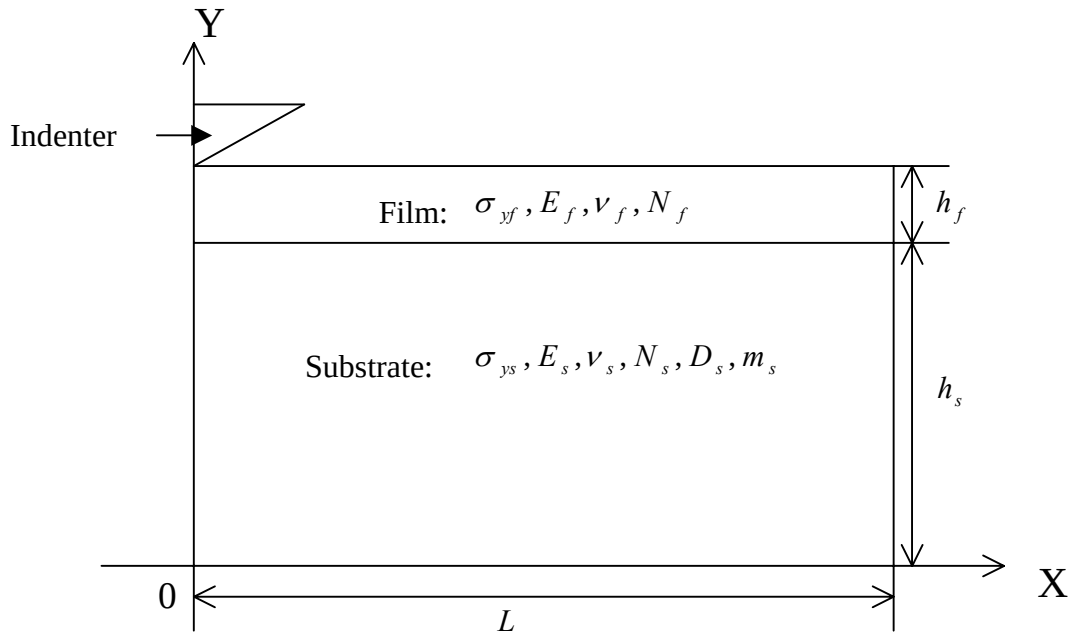

Fig. 3-3 Schematic description of the geometric and material properties.

and a convenient length of Δ_0=1μm. For the typical values of interface adhesion properties: $\lambda_1 = 0.15$, $\lambda_2 = 0.5$, $\delta_n^c / \delta_t^c = 1$, $\hat{\sigma} = 0.4\sigma_{yf}$, and $\Gamma_0 = 0.0039\sigma_{yf}\Delta_0$. For the typical geometric data: the thicknesses of the film and the substrate are $h_f = 6\Delta_0$ and $h_s = 60\Delta_0$, respectively; the length of the system is $L = 120\Delta_0$. For the typical material properties: the Young's moduli of the film and substrate are $E_f = 350\sigma_{yf}$ and $E_s = 700\sigma_{yf}$, respectively; the Poisson ratios are $\nu_f = \nu_s = 0.3$; the strain hardening exponents are $N_f = N_s = 0.1$; the yield strength of substrate is $\sigma_{ys} = 2.0\sigma_{yf}$, and the reference strain rate and strain rate sensitivity exponent of the substrate are respectively $D_s = 4.0\text{s}^{-1}$ and $m_s = 5.0$.

With the initial data given, the following information can be obtained from simulations: the load-penetration curve, the critical state (include the critical load, the critical displacement, etc.) at the onset of delamination, and the distribution of the stress and strain in the system and so on.

3.5.1. Interpretation of Load-Penetration Curve

The load-penetration curve obtained for the typical case described above is shown in Figure 3-4. The small fluctuations of the raw simulation data points are due to the discrete nature of finite elements along the contact interface between the wedge indenter and the thin film surface. Five-Point Fast Fourier Transform (FFT) is used to smoothen the curve. The initial part of the curve (A→B) is almost linear, indicating that the substrate effect is negligible. With the increase of the penetration depth, the curve becomes superlinear due to the increasing effect from the harder substrate. The

sudden load decrease at point C in the curve corresponding to the onset of the interface delamination, gives the critical load P_c. After delamination, the stiffness of the whole system decreases significantly, which can be seen from the change of the slope of the curve.

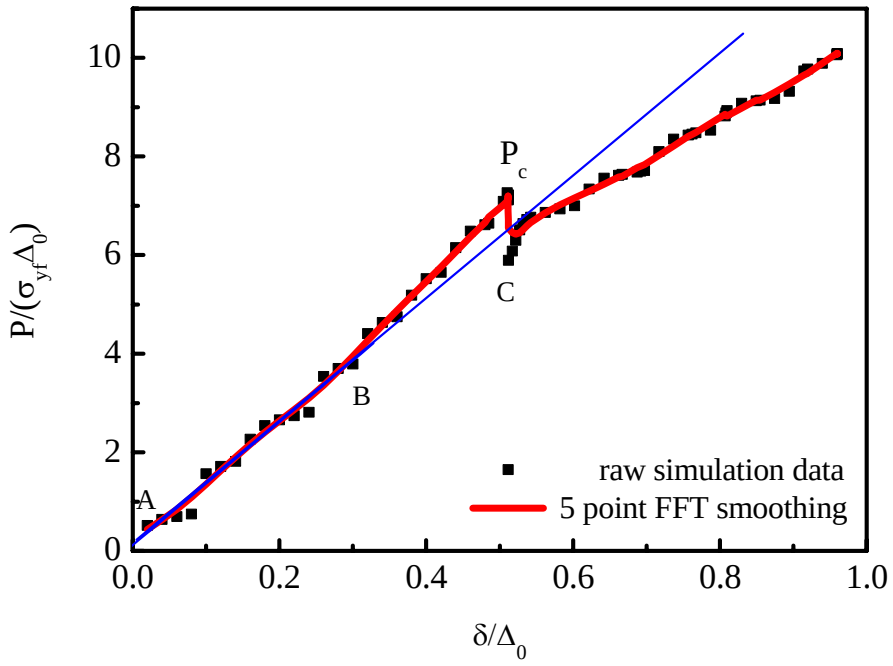

Fig. 3-4 Load versus penetration curve obtained by simulation for the typical case.

3.5.2. Evolution of Traction and Separation along Interface

Before interface delamination, the normal traction along the interface is negative, indicating that the film and substrate are in contact with each other. Correspondingly, the normal separation is zero along the interface. Hence the interface loading condition is in a pure shear mode.

However, after the interface delamination and further propagation, the interface loading condition transits into a mixed mode. As can be clearly seen from Figure 3-5,

the normal separation is no longer zero (the coordinate system is the same as that shown in Figure 3-2).

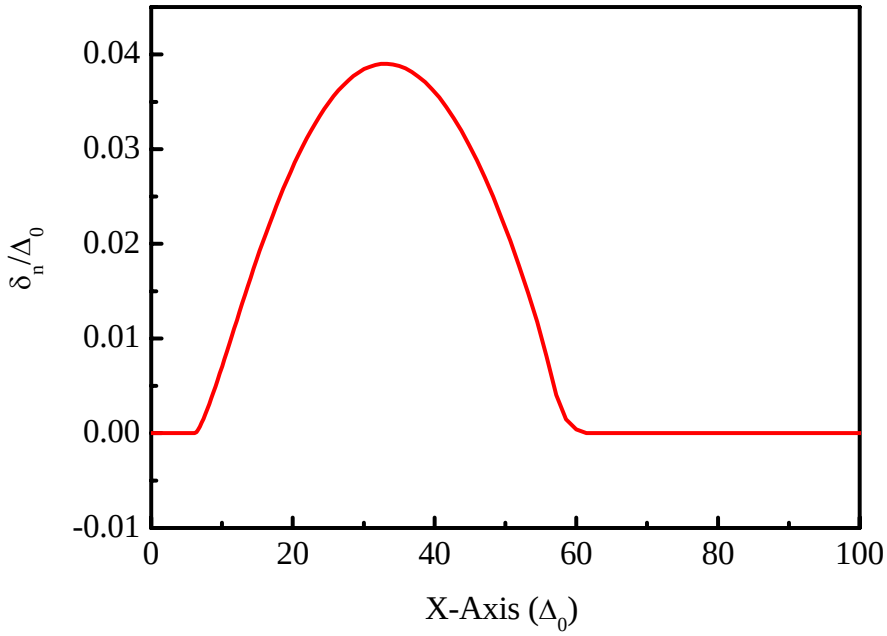

Fig. 3-5 Normal separation along the interface long after the critical moment.

The changes in shear traction and shear separation shed light on the process of interface delamination. Figure 3-6(a) shows the shear separation profile just before the interface delamination. The maximum shear separation is approximately $0.01\Delta_0$, smaller than the critical shear separation, $0.014\Delta_0$. The corresponding shear traction distribution is shown in Figure 3-7(a). It is seen that the traction at the maximum separation is lower than its surroundings, indicating the shear traction has already exceeded the maximum stress level, $0.4\sigma_{yf}$. The constant stress level, which equals to $0.4\sigma_{yf}$, is determined by the shape of TSL as shown in Figure 3-1. When the shear separation increases further and exceeds the critical separation as shown in Figure 3-6(b), the interface delamination occurs. The traction drops to zero at the positions

where the shear separation exceeds the critical one as shown in Figure 3-7(b). With further increase of the indentation depth, the shear separation increases further as shown in Figure 3-6(c), and the range in which the shear traction drops to zero also increases due to the propagation of the delamination as shown in Figure 3-7(c) (the coordinate system is the same as that shown in Figure 3-2).

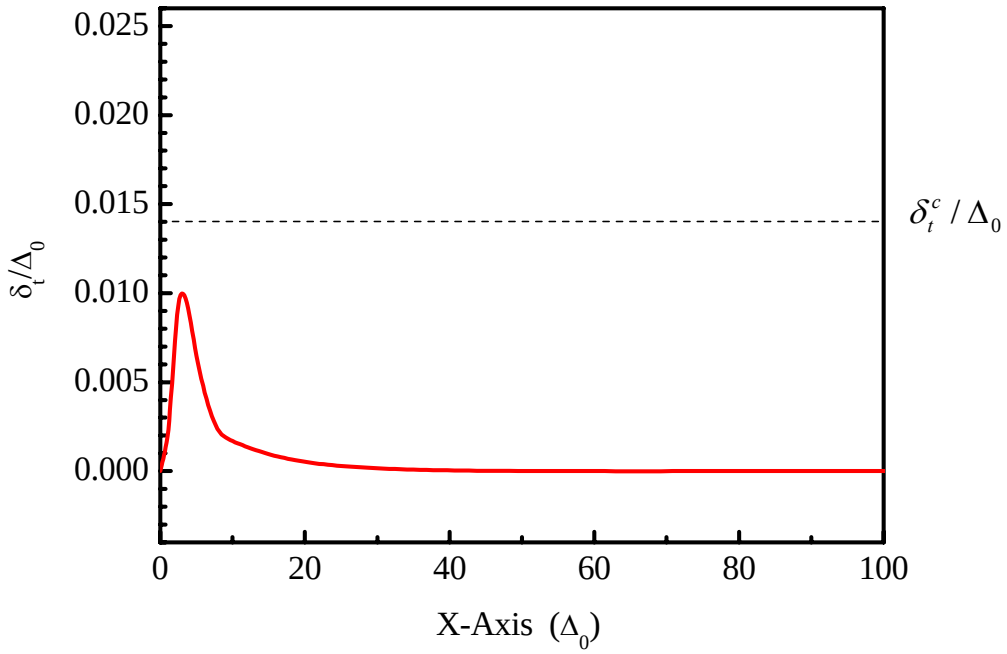

(a)

(**Fig. 3-6** to be continued)

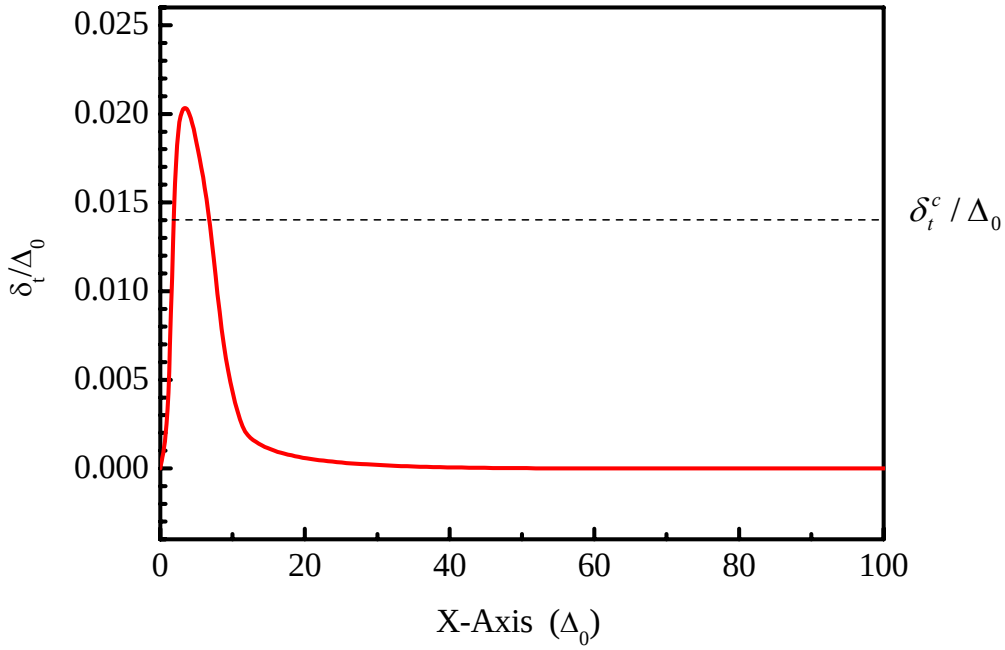

(b)

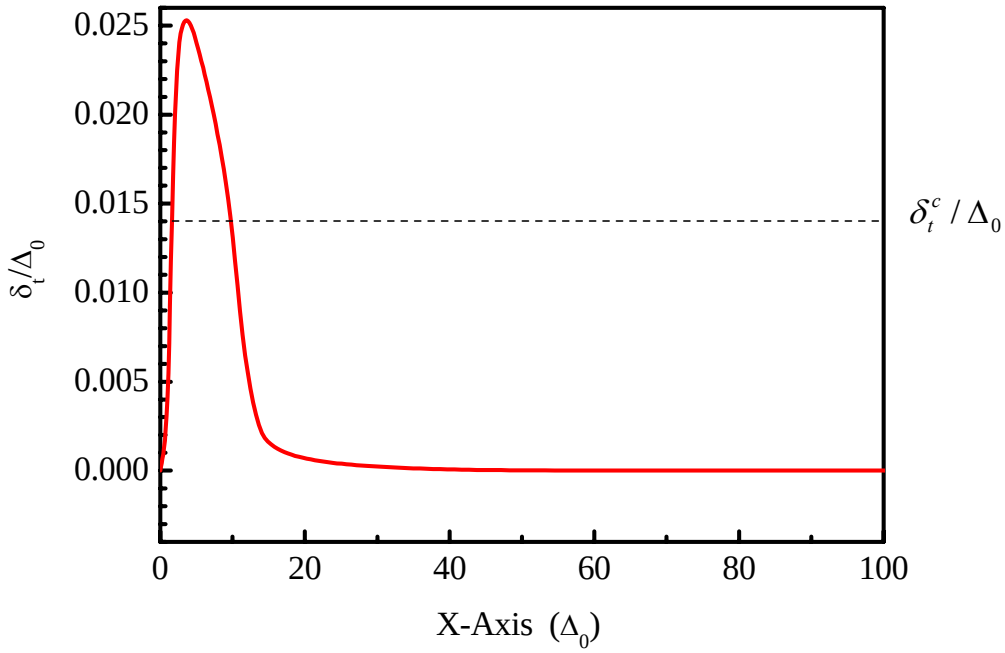

(c)

Fig. 3-6 Shear separation along the interface: (a) before the critical moment, (b) near the critical moment, and (c) after the critical moment.

δ_t^c is the pre-set critical separation.

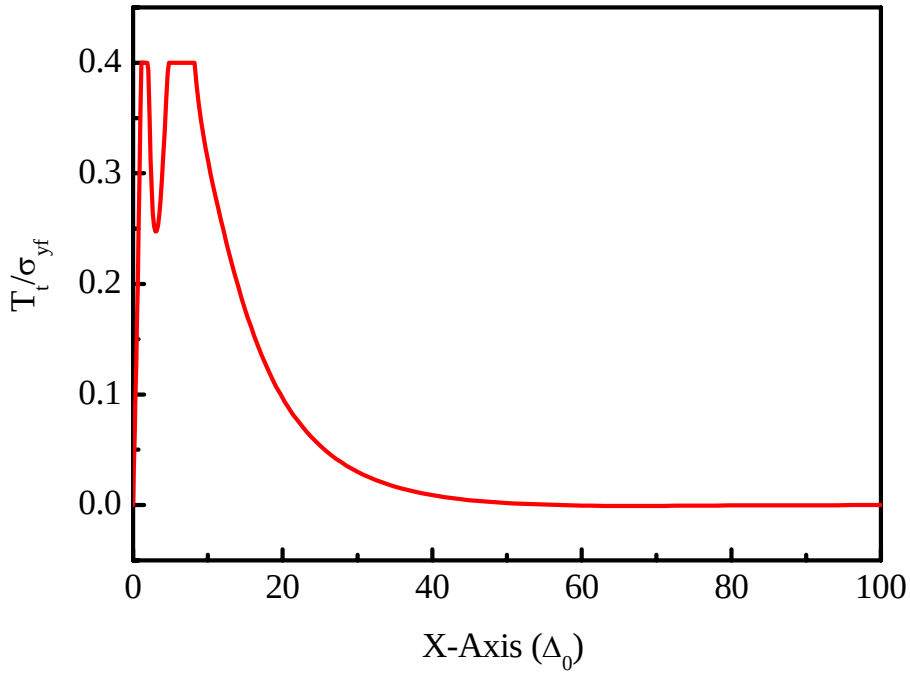

(a)

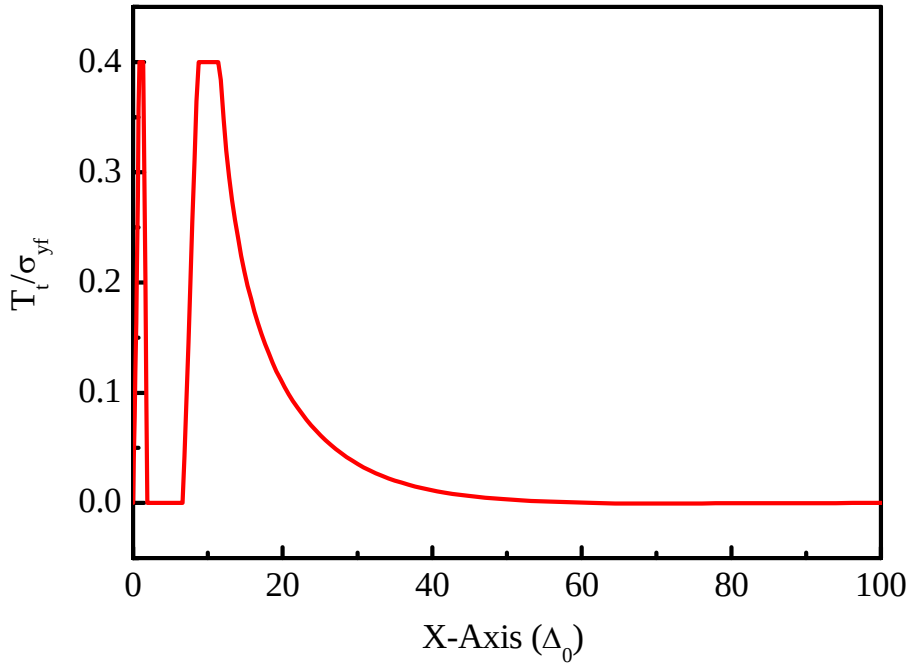

(b)

(**Fig. 3-7** to be continued)

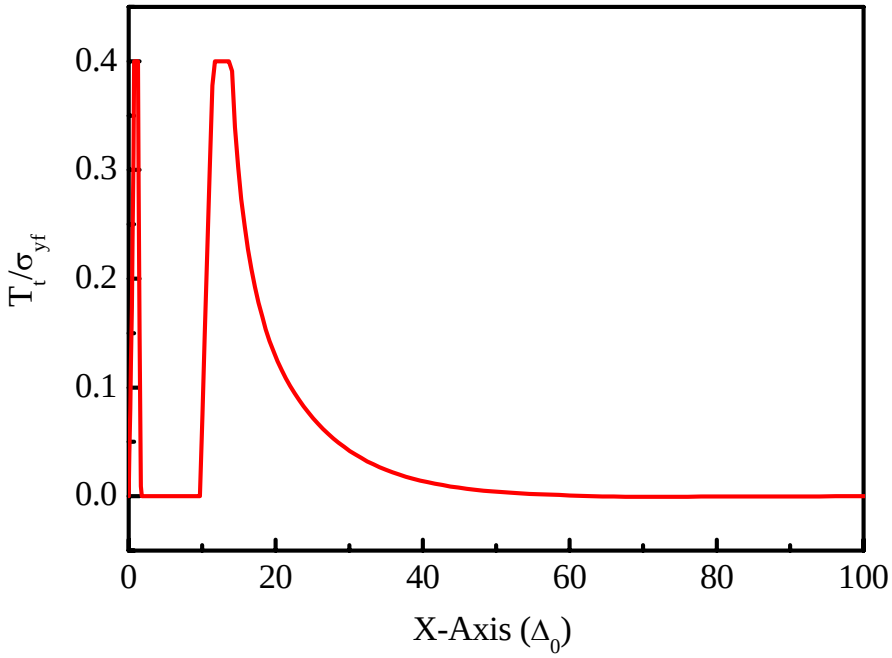

(c)

Fig. 3-7 Shear traction along the interface: (a) before the critical moment, (b) near the critical moment, and (c) after the critical moment.

The evolution of the traction and the separation along the interface shows clearly that the interface delamination initiates in pure shear (mode II), and subsequently transits into a mode II-dominated mixed mode upon further propagation. This result is consistent with that obtained by Li and Siegmund [19].

3.6. Effect of Interface Adhesion Properties

In order to develop an approach to extract the interface adhesion properties from the experimentally-measured information such as load-penetration curves, it is necessary to investigate their effects on the initiation of interface delamination. Many previous studies show that interface strength and interface energy are the two most

important parameters that govern the interface adhesion quality [8]. Therefore, we only focus on these two parameters. Their effects are investigated by parametric studies, during which the values of parameters of interest vary while all the other dimensionless parameters are fixed at typical values as given in the previous subsection. During the parametric studies, the interface strength varies from $\hat{\sigma} = 0.20\sigma_{yf}$ to $\hat{\sigma} = 0.80\sigma_{yf}$ while the interface energy varies from $\Gamma_0 = 0.0020\sigma_{yf}\Delta_0$ to $\Gamma_0 = 0.0100\sigma_{yf}\Delta_0$.

3.6.1. Effect of Interface Energy

With the variation of interface strength from $\hat{\sigma} = 0.20\sigma_{yf}$ to $\hat{\sigma} = 0.80\sigma_{yf}$, the critical load P_c / σ_{yf} corresponding to the onset of the interface delamination

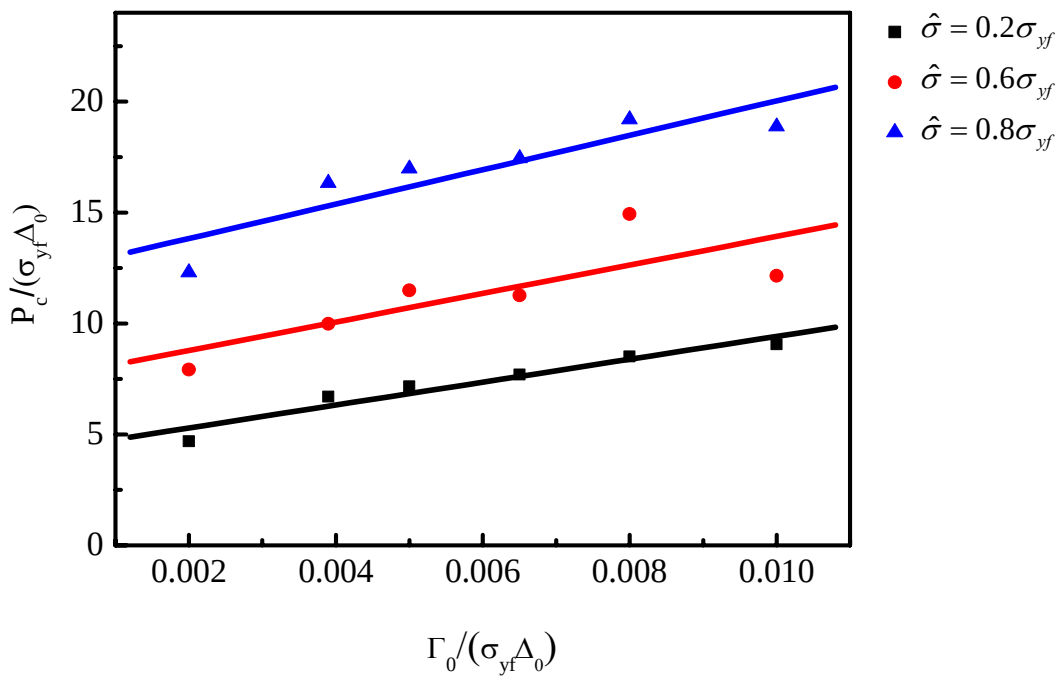

Fig. 3-8 Critical load versus interface energy at different levels of interface strength. The solid lines are the linear fit of the data points.

increases approximately linearly with an increase in interface energies as shown in Figure 3-8. This increase can be attributed to the increase in plastic dissipation. When the interface strength is fixed, the plastic zones in the film increase gradually with an increase in interface energy. This is evidenced by the size change of plastic zones colored by red as shown in Figure 3-9 to Figure 3-11 at different levels of interface energy when the interface strength is kept at $\hat{\sigma} = 0.20\sigma_{yf}$ (the coordinate system is the same as that shown in Figure 3-2).

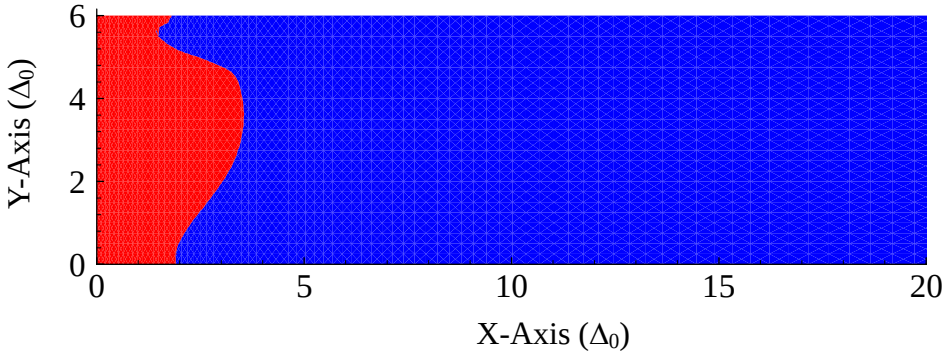

Fig. 3-9 Plastic zone in the film right before delamination when $\Gamma_0 = 0.0020\sigma_{yf}\Delta_0$ and $\hat{\sigma} = 0.20\sigma_{yf}$.

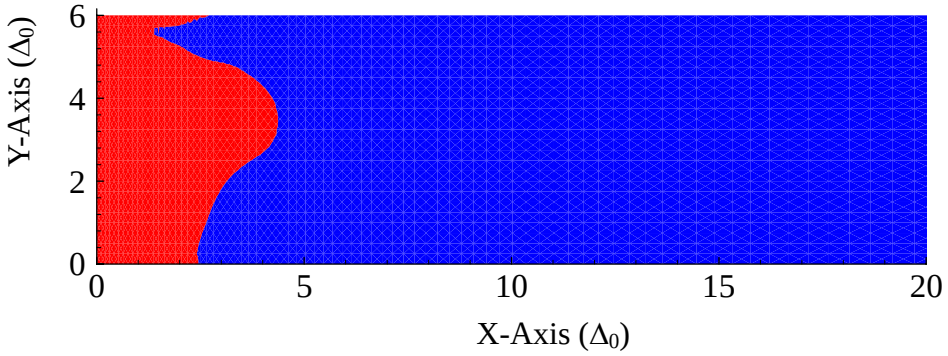

Fig. 3-10 Plastic zone in the film right before delamination when $\Gamma_0 = 0.0065\sigma_{yf}\Delta_0$ and $\hat{\sigma} = 0.20\sigma_{yf}$.

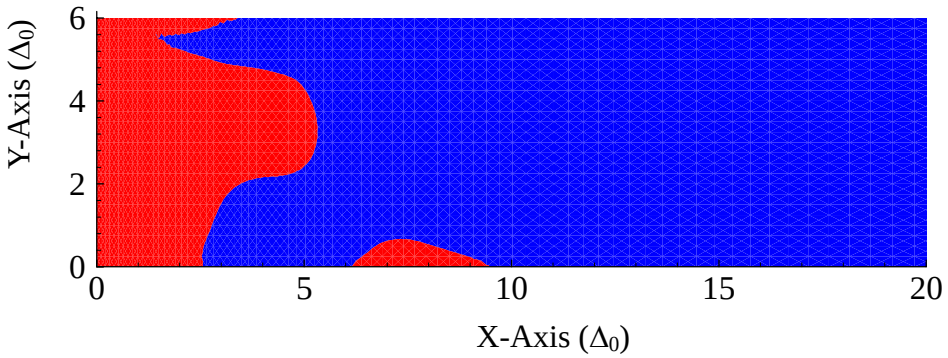

Fig. 3-11 Plastic zone in the film right before delamination when $\Gamma_0 = 0.0100\sigma_{yf}\Delta_0$ and $\hat{\sigma} = 0.20\sigma_{yf}$.

3.6.2. Effect of Interface Strength

When interface energy Γ_0 is fixed, the critical load generally increases superlinearly with increasing interface strength as shown in Figure 3-12 to Figure 3-14. However, it is noticed that at a low interface strength level, the critical load is approximately insensitive to the change of interface strength when the value of

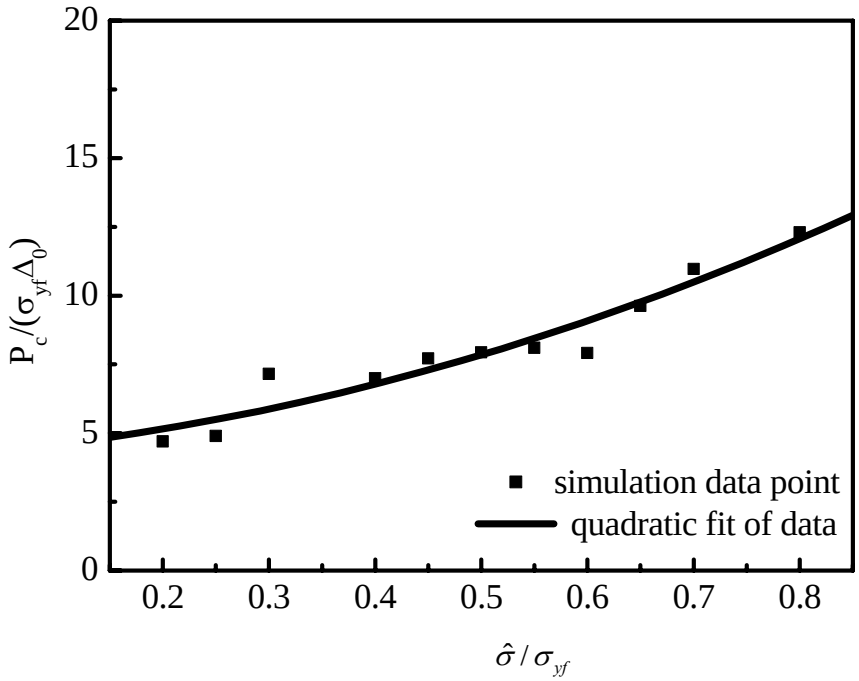

Fig. 3-12 Critical load versus interface strength when interface energy $\Gamma_0 = 0.0020\sigma_{yf}\Delta_0$.

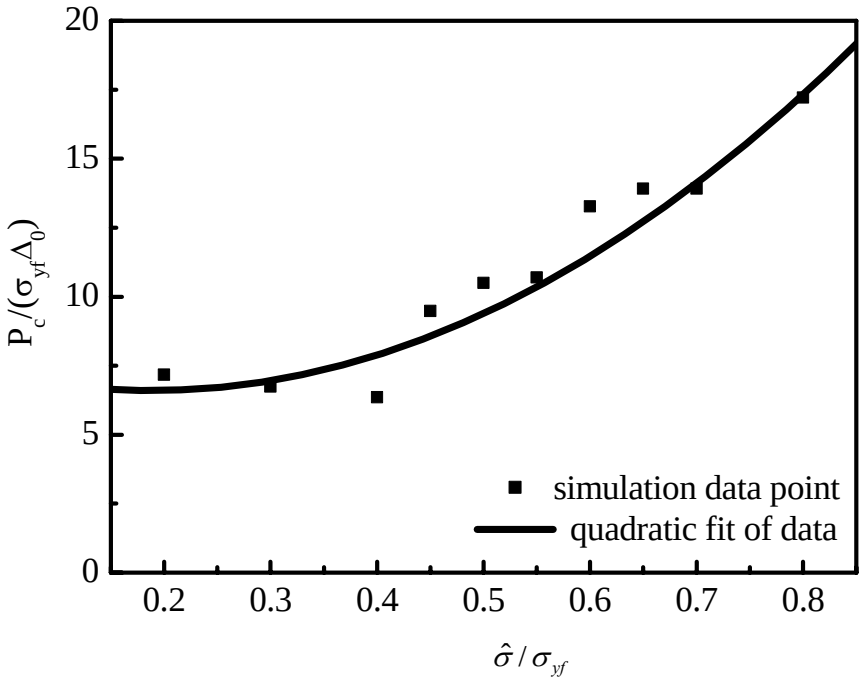

Fig. 3-13 Critical load versus interface strength when interface energy $\Gamma_0 = 0.0050\sigma_{yf}\Delta_0$.

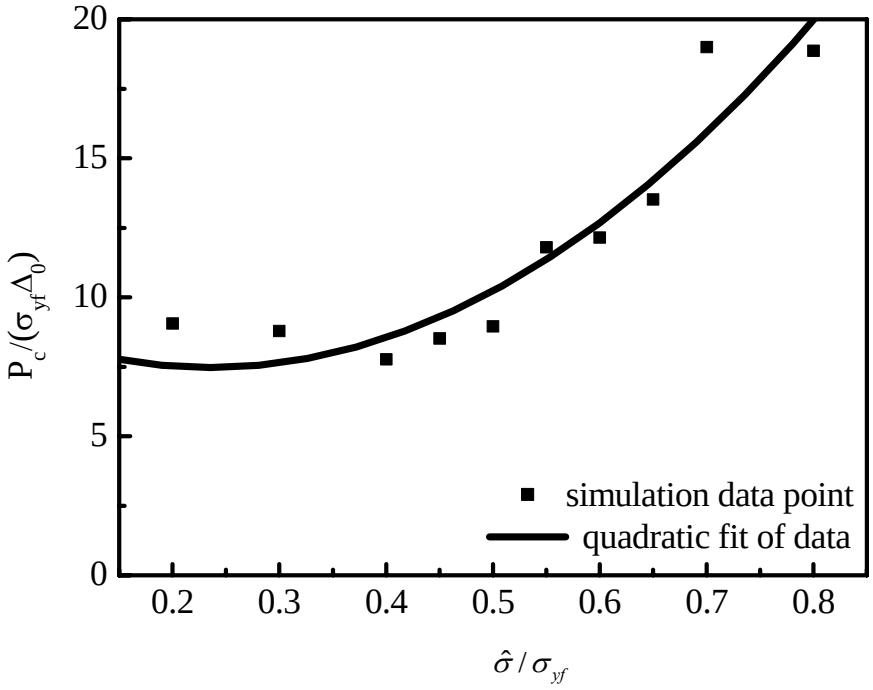

Fig. 3-14 Critical load versus interface strength when interface energy $\Gamma_0 = 0.0100\sigma_{yf}\Delta_0$.

interface energy is fixed at a large value as shown in Figure 3-14. This may be explained by the competition between two factors, i.e., interface strength $\hat{\sigma}$ and critical separation $\delta_t^c = \delta_n^c$. Referring to Eq.(3.2.9):

$$\Gamma_0 = \hat{\sigma}\delta_n^c(1-\lambda_1+\lambda_2)/2$$

we can see that the increase in interface strength $\hat{\sigma}$ will cause a decrease in the critical separation δ_n^c since interface energy Γ_0 is fixed. Meanwhile, the increase in interface strength $\hat{\sigma}$ will increase the critical load to initiate interface delamination, whereas the decrease of the critical separation $\delta_n^c = \delta_t^c$ will cause the critical load to decrease. In this region, our simulation results show that the plastic zones are of similar size (refer to Figure 3-15 to Figure 3-16, the coordinate system is the same as that shown in Figure 3-2) so that the plastic dissipation is approximately at the same level. Since the interface energy is fixed, the total energy dissipation should also be approximately at the same level, leading to the similar critical loads.

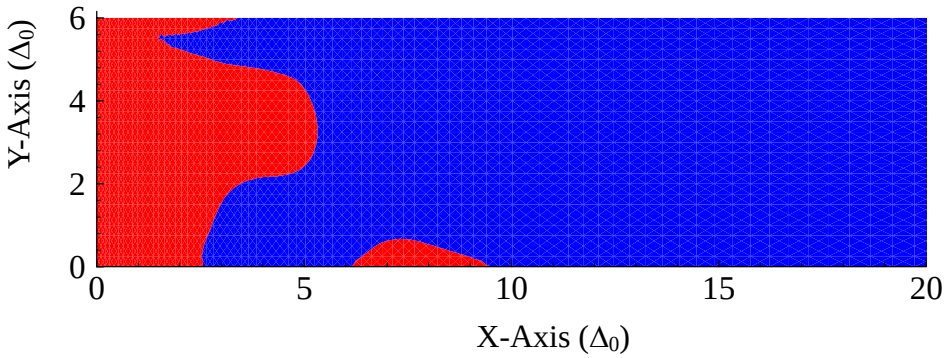

Fig. 3-15 Plastic zone in the film right before delamination when $\hat{\sigma} = 0.20\sigma_{yf}$ and $\Gamma_0 = 0.0100\sigma_{yf}\Delta_0$.

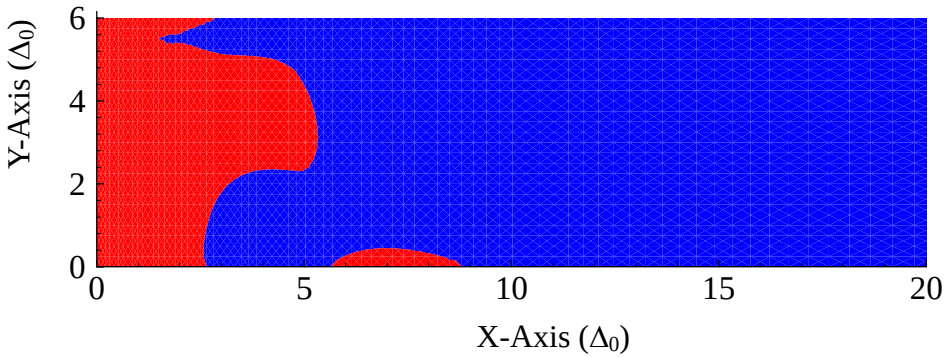

Fig. 3-16 Plastic zone in the film right before delamination when $\hat{\sigma} = 0.30\sigma_{yf}$ and $\Gamma_0 = 0.0100\sigma_{yf}\Delta_0$.

When $\hat{\sigma}/\sigma_{yf}$ is larger than 0.4, it is seen that the critical load P_c increases superlinearly with increasing interface strength $\hat{\sigma}$, while it only increases approximately linearly with increasing interface energy Γ_0 as discussed in previous subsection. This suggests that in this range, the effect of interface strength $\hat{\sigma}$ on the critical load P_c is more significant than that of interface energy Γ_0. The reason for this is that the change in the plastic zone size with interface strength at a fixed interface energy is more significant than that with increasing interface energy at a fixed interface strength (refer to Figure 3-9 to Figure 3-11). For example, when interface energy is kept at $\Gamma_0 = 0.0039\sigma_{yf}\Delta_0$, the plastic zone size just before the delamination increases significantly with increasing interface strength as shown in Figure 3-17 to Figure 3-19 (the coordinate system is the same as that shown in Figure 3-2).

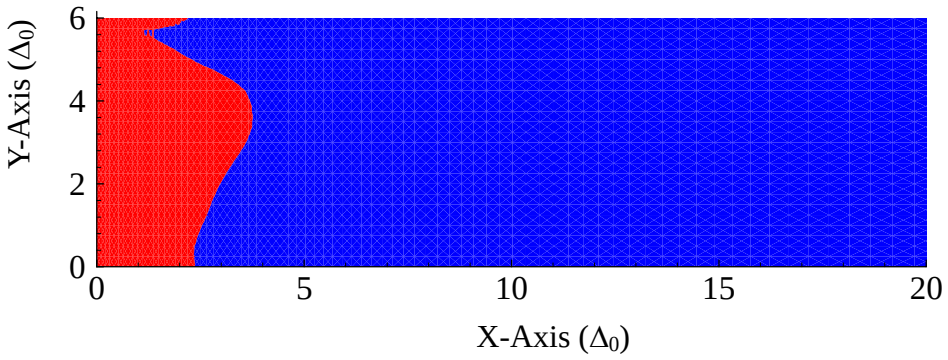

Fig. 3-17 Plastic zone in the film before delamination when $\hat{\sigma} = 0.20\sigma_{yf}$ and $\Gamma_0 = 0.0039\sigma_{yf}\Delta_0$.

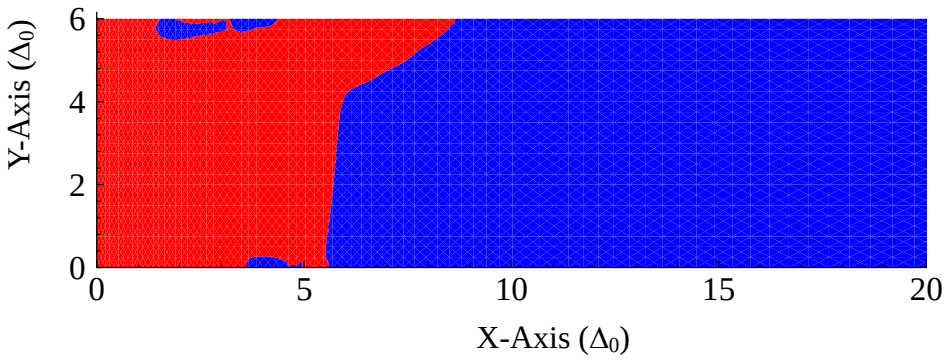

Fig. 3-18 Plastic zone in the film before delamination when $\hat{\sigma} = 0.55\sigma_{yf}$ and $\Gamma_0 = 0.0039\sigma_{yf}\Delta_0$.

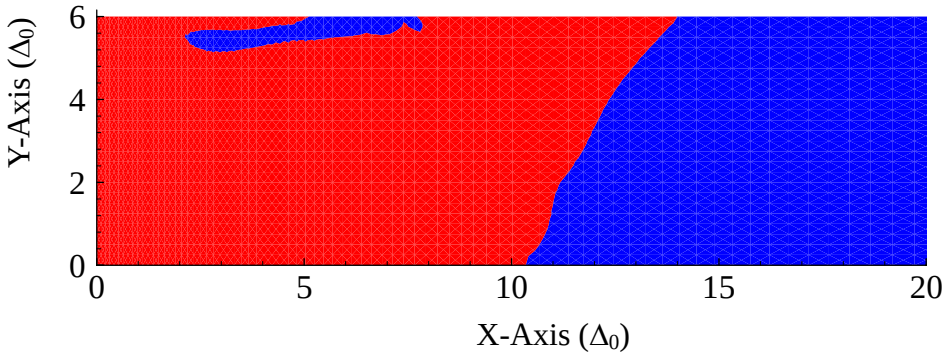

Fig. 3-19 Plastic zone in the film before delamination when $\hat{\sigma} = 0.80\sigma_{yf}$ and $\Gamma_0 = 0.0039\sigma_{yf}\Delta_0$.

In summary, the present simulation results clearly show that the initiation of interface delamination is closely related to the interface adhesion properties. An

increase in either the interface strength $\hat{\sigma}$ or the interface energy Γ_0 will result in an increase in the critical load P_c to initiate interface delamination. However, the effect of the interface strength $\hat{\sigma}$ on the critical load P_c is more significant than that of the interface energy Γ_0. This may be due to the fact that during indentation, the total energy dissipation is closely related to the plastic energy dissipation arising from the plastic deformation and surface energy arising from interface delamination. It appears that when $\hat{\sigma}/\sigma_{yf}$ is larger than 0.4, an increase in interface strength is more effective to increase the plastic deformation than an increase in interface energy, resulting in a more effective increase in the critical load.

3.7. Determination of Interface Adhesion Properties

For thin-film/substrate systems with weak interfaces, buckling may occur during indentation. As a result, interface toughness and interface adhesion properties may be determined by fracture mechanics since the plastic deformation is negligible [16-18]. However, for thin-film/substrate systems with strong interfaces, plastic zone size may be large compared with the characteristic length of the thin film systems. Thus the determination of the interface adhesion properties becomes a challenging issue. In the present work, a scheme based on the work of Li and Siegmund [19] is developed to determine the interface adhesion properties regardless of the plastic zone size.

Our parametric studies have shown that an increase in either interface strength $\hat{\sigma}$ or interface energy Γ_0 will cause an increase in the critical load P_c to initiate interface delamination, and their relationships can be described approximately by a

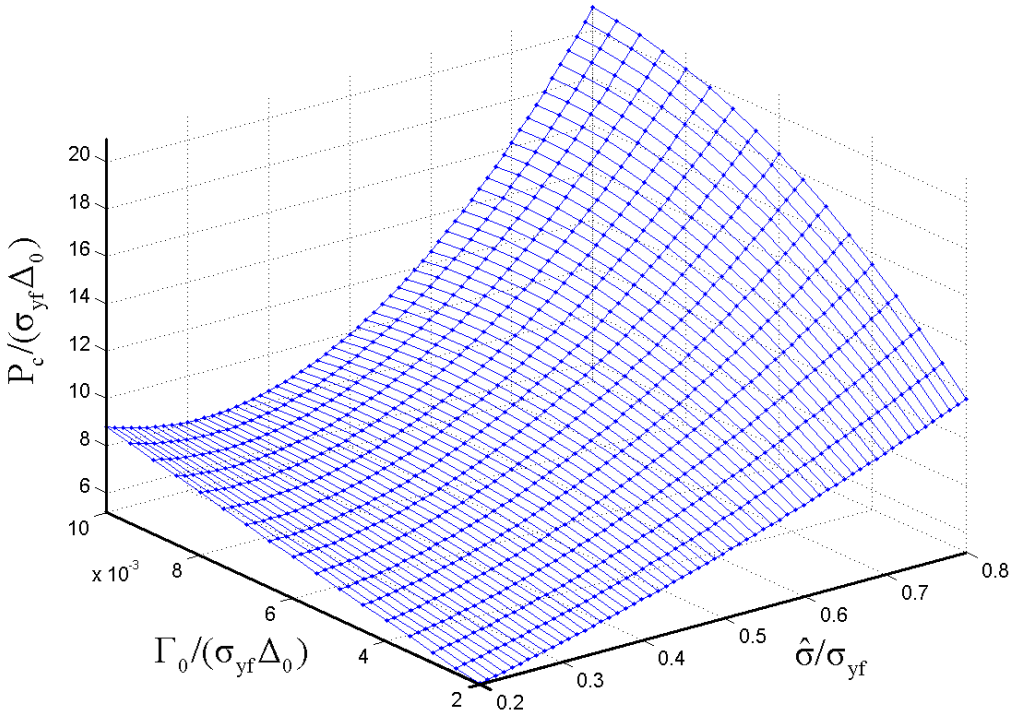

(a)

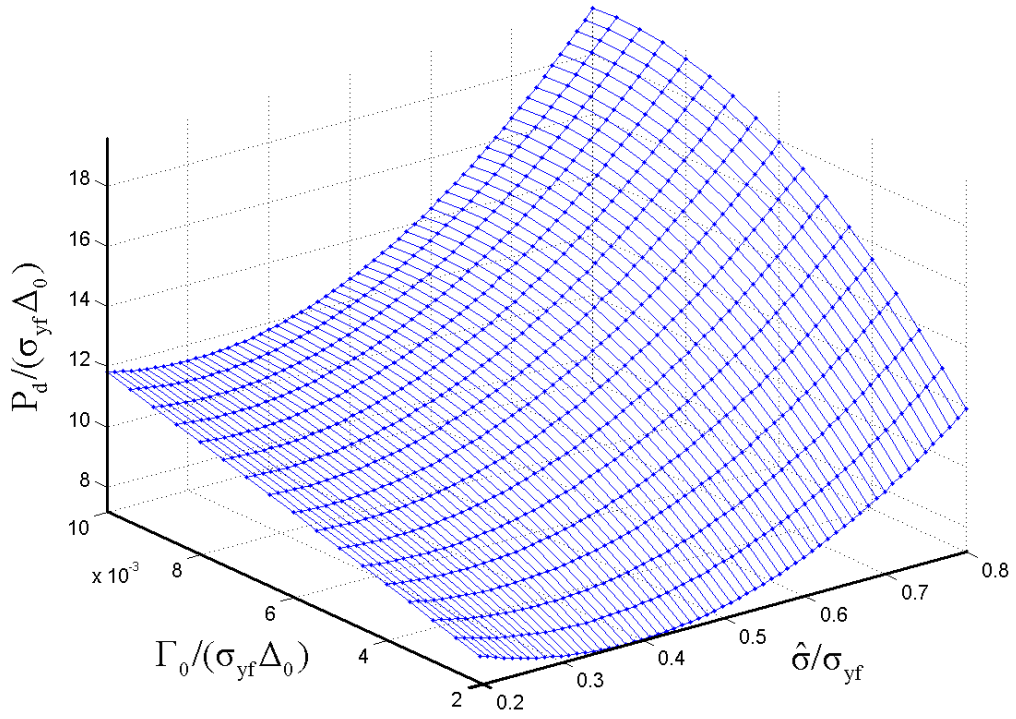

(b)

Fig. 3-20 Dependence on the interface adhesion properties of (a) P_c, and (b) P_d.

linear or superlinear fitting function. Thus a quadratic polynomial function is chosen to depict the dependence of the critical load P_c on interface strength $\hat{\sigma}$ and interface energy Γ_0 as shown in Figure 3-20 (a).

To determine the interface adhesion properties, i.e., interface strength $\hat{\sigma}$ and interface energy Γ_0, two characteristic parameters in the experimentally-measured load-penetration curves are needed. Other than the critical load P_c at the onset of the interface delamination, the load P_d at an additional penetration depth d after the interface delamination is used as the other characteristic parameter. Here $d = 0.3\Delta_0$ is chosen. The dependence of P_d on the interface strength $\hat{\sigma}$ and interface energy Γ_0 is depicted in Figure 3-20 (b). By replotting the data, we obtain a contour plot shown in Figure 3-21.

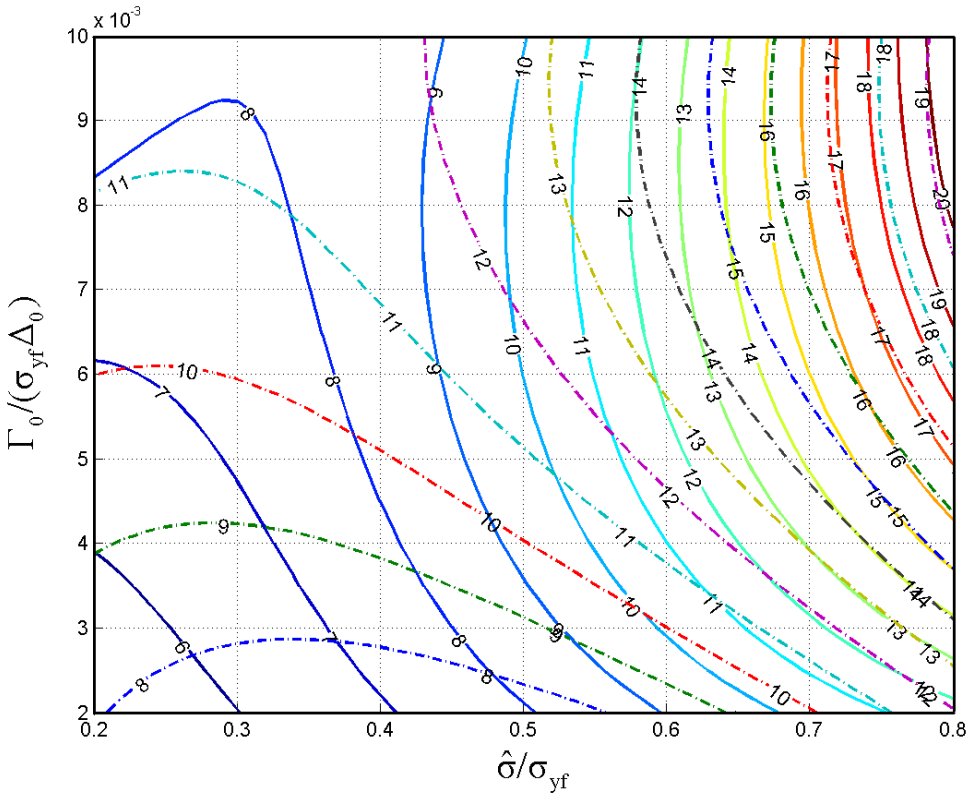

Fig. 3-21 Contour plots of the variation of P_c and P_d with interface adhesion properties. Solid line: $P_c/(\sigma_{yf}\Delta_0)$, and dashed line: $P_d/(\sigma_{yf}\Delta_0)$.

Therefore, the following scheme is proposed to determine the interface adhesion properties from the experimentally-measured information: 1) experiments are performed to measure the parameters of the thin film and substrate required for the simulations; 2) a series of basic simulations are performed to obtain the dependence of P_c and P_d on the interface strength $\hat{\sigma}$ and interface energy Γ_0; 3) a wedge indentation test is carried out to obtain P_c^e and P_d^e for the thin film system of interest; and finally 4) the interface strength $\hat{\sigma}$ and interface energy Γ_0 can be extracted by using P_c^e and P_d^e measured by the indentation test. The experiments to obtain the parameters for simulations will be presented in detail in the next chapter.

Several tests have been performed to check the accuracy of the proposed method. First, we select different intersections of P_c and P_d in the contour plot and determine the corresponding interface strength $\hat{\sigma}$ and interface energy Γ_0. Next, we perform FEM simulations with $\hat{\sigma}$ and Γ_0 as input data to obtain P_c' and P_d'. Finally, the relative errors between P_c and P_c', P_d and P_d' are calculated and listed in Table 3-1. All the values listed in Table 3-1 are normalized.

Table 3-1 Accuracy of the method.

$P_c/(\sigma_{yf}\Delta_0)$	$P_d/(\sigma_{yf}\Delta_0)$	$\hat{\sigma}/\sigma_{yf}$	$\Gamma_0/(\sigma_{yf}\Delta_0)$	$P_c'/(\sigma_{yf}\Delta_0)$	$P_d'/(\sigma_{yf}\Delta_0)$	$\frlvert P_c'-P_c\frrvert/P_c$	$\frlvert P_d'-P_d\frrvert/P_d$
6.0	8.0	0.2695	0.002676	5.5848	8.2091	6.92%	2.61%
7.0	9.0	0.3193	0.00 4196	6.2018	9.0806	11.40%	0.90%
8.0	8.0	0.4793	0.002443	7.9850	7.9850	0.19%	0.19%
8.0	11.0	0.3374	0.007885	7.9819	10.3801	0.23%	5.64%
11.0	11.0	0.6284	0.003422	11.2514	11.2514	2.29%	2.29%
11.0	13.0	0.5343	0.007792	10.0539	12.9243	8.60%	0.58%
14.0	15.0	0.6442	0.007569	14.2815	14.2815	2.01%	4.79%
12.0	12.0	0.6692	0.003629	10.9218	10.9218	8.99%	8.99%
12.0	12.0	0.7679	0.002409	11.3087	11.3087	5.76%	5.76%
17.0	17.0	0.7386	0.006987	14.4983	14.4983	14.72%	14.72%
20.0	19.0	0.7822	0.009738	17.2099	17.2099	13.95%	9.42%

It seems that the predictions agree well with the simulation results since the relative errors are within 15% for all the cases tested. However, there are still some limitations for this method:

I) Certain inaccuracy may arise from the simple quadratic polynomial fitting function, which may not be a perfect representation for the real dependence of P_c and P_d on the interface strength $\hat{\sigma}$ and interface energy Γ_0.

II) For interfaces with large values of the interface strength $\hat{\sigma}$ and interface energy Γ_0, unstable crack propagation immediately follows the occurrence of interface delamination. Hence, it is impossible to measure the value of P_d and we take $P_d = P_c$ for these cases. As a consequence, the interface adhesion

quality may be overestimated.

III) For the region in the contour plot (Figure 3-20) with large values of interface strength $\hat{\sigma}$ and interface energy Γ_0, the two families of curves are almost parallel to each other, which makes it difficult to determine the values of $\hat{\sigma}$ and Γ_0. This phenomenon was also observed in Li and Siegmund's work [19], although their basic series of simulations were different from ours.

IV) Under certain circumstances, two curves may intersect with each other at two different positions, giving two pairs of $\hat{\sigma}$ and Γ_0. This may be caused by the inaccuracy of interpolations. From the cases tested, the relative errors at the two positions (see Table 3-1, the eighth and ninth cases) are in the same order. This suggests that the two systems with two pairs of interface strength $\hat{\sigma}$ and interface energy Γ_0 may have the same P_c and P_d. Thus, more information is needed to determine the interface adhesion properties when the experimentally-measured P_c^e and P_d^e fall in this range.

3.8. Summary

Based on the results discussed above, the following conclusions can be reached:

I) The approach using TSL and FEM provides an effective way to investigate the interface delamination in a thin-film/substrate system induced by indentation.

II) The critical load to initiate interface delamination in a thin-film/substrate system increases with either increasing interface strength or increasing interface energy. However, the effect of the former on interface adhesion properties is more

significant than that of the latter when $\hat{\sigma}/\sigma_{yf}$ is larger than 0.4.

III) A scheme combining simulations and experiments is proposed to determine interface strength $\hat{\sigma}$ and interface energy Γ_0 from indentation load-penetration curves.

References

[1]. Y. W. Zhang, K. Y. Zeng and R. Thampurun, Mater. Sci. Eng. A319 (2001) 893.

[2]. P. Liu, L. Cheng and Y. W. Zhang, Acta Mater. 49 (2001) 817.

[3]. V. Tvergaard and J. W. Hutchinson, J. Mech. Phys. Solids 40 (1992) 1377.

[4]. V. Tvergaard and J. W. Hutchinson, J. Mech. Phys. Solids 41 (1993) 1119.

[5]. V. Tvergaard and J. W. Hutchinson, Phil. Mag. A70 (1994) 641.

[6]. V. Tvergaard and J. W. Hutchinson, J. Mech. Phys. Solids 44 (1996) 789.

[7]. J. G. Williams and H. Hadavinia, J. Mech. Phys. Solids 50 (2002) 809.

[8]. Y. Wei and J. W. Hutchinson, Int. J. Fracture 93 (1998) 315.

[9]. D. J. Hayes, Some Applications of Elastic Plastic Analysis to Fracture Mechanics, Ph.D. Thesis, Imperial College of Science and Technology, London, 1970.

[10]. M. Ortiz and E. P. Popov, Int. J. Num. Meth. Eng. 21 (1985) 1561.

[11]. J. C. Simo and M. Ortiz, Comp. Meth. Appl. Mech. Eng. 49 (1985) 221.

[12]. M. Ortiz and J. C. Simo, Int. J. Num. Meth. Eng. 23 (1986) 353.

[13]. N. Aravas, Int. J. Num. Meth. Eng. 24 (1987) 1395.

[14]. J. C. Nagtegaal, Comp. Meth. Appl. Mech. Eng. 33 (1982) 469.

[15]. J. C. Simo and R. L. Taylor, Comp. Meth. Appl. Mech. Eng. 48 (1985) 101.

[16]. D. B. Marshall and A. G. Evans, J. Appl. Phys. 56 (1984) 2632.

[17]. A. A. Volinsky, N. R. Moody and W. W. Gerberich, Acta Mater. 50 (2002) 441.

[18]. W. Li and T. Siegmund, Acta Mater. 52 (2004) 2989.

[19]. W. Li and T. Siegmund, CMES-Comp. Model. Eng. Sci. 5 (2004) 81.

Chapter 4 Experiments and Discussions

4.1. Methodology

In the experiment part of this project, we use wedge indentation technique to investigate mechanical properties of thin films, interface adhesion properties and interface delamination processes. The experiments are performed using a conventional nanoindenter (UMIS-2000H, CSIRO, Australia) with a wedge tip made of diamond. The tip length is 4.206μm and the included-angle is 120°. The advantage of using a wedge indenter is that the thin-film/substrate systems are under plain-strain conditions, which alleviates the tensile stresses that usually cause radial cracks. In addition, the driving force for delamination is the largest among all indenter geometries so that systems with strong adherent interfaces can be tested and characterized [1].

Numerical analysis is then applied to obtain the hardness, Young's modulus of the film, and if applicable, together with the yield strength of the film by using the method derived by Johnson [2]. Furthermore, FEM simulations are conducted to derive the interface adhesion properties, i.e., interface strength and interface energy, based on the experimental data.

Scanning electron microscope (SEM, JSM-5400, JEOL, Japan) is used to observe surface morphology, width and length of indentation impression, pattern of delamination failure and so on. These features are then correlated with various characteristics of the load-penetration curves measured from the indentation tests.

4.2. Indentation Equipment

Ultra-Micro Indentation System (UMIS-2000H, CSIRO, Australia) is used to perform indentation experiments on the thin-film systems. The indenter is driven into the surface by a piezo-ceramic loading system until a resistance equal to a pre-set force is met [3]. The penetration depth is measured under the conditions of force equilibrium at each step. Load is transmitted to the indenter shaft through a spring system as illustrated in Figure 4-1, whose deflection is measured by a Force-LVDT (linear variable differential transformer). The relative displacement of the indenter shaft is measured correspondingly by a Depth-LVDT when the indenter contacts the sample [4].

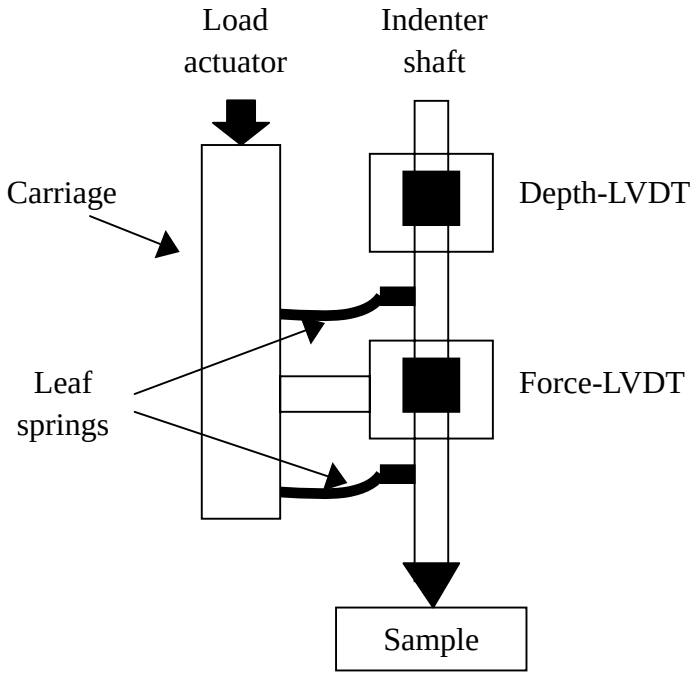

Fig. 4-1 Schematic description of UMIS nanoindenter [3].

The system allows two independent settings of depth and force measurement shown in Table 4-1 [3].

Table 4-1 UMIS-2000H nanoindenter specifications [3].

Depth setting	A	B
Range of penetration	0-2μm	0-40μm
Displacement resolution	0.05nm	
Force setting	A	B
Range of maximum force	0-50mN	0-500mN
Force resolution	0.75μN	

4.3. Experimental Procedure

Two types of experimental procedures are carried out in this project:

Procedure A illustrated in Figure 4-2 consists of the following steps: 1) the indenter approaches the surface until a pre-set initial contact force (usually 0.1mN) is reached; 2) it is then followed by a loading segment until the pre-set maximum load is reached; 3) the indenter is held at the maximum load for 5 seconds; 4) afterwards, the indenter is withdrawn from the sample at the same rate as that in the loading segment; and 5) the indenter is held in contact with the surface at 10% of the maximum load for 30 seconds to correct the thermal drift.

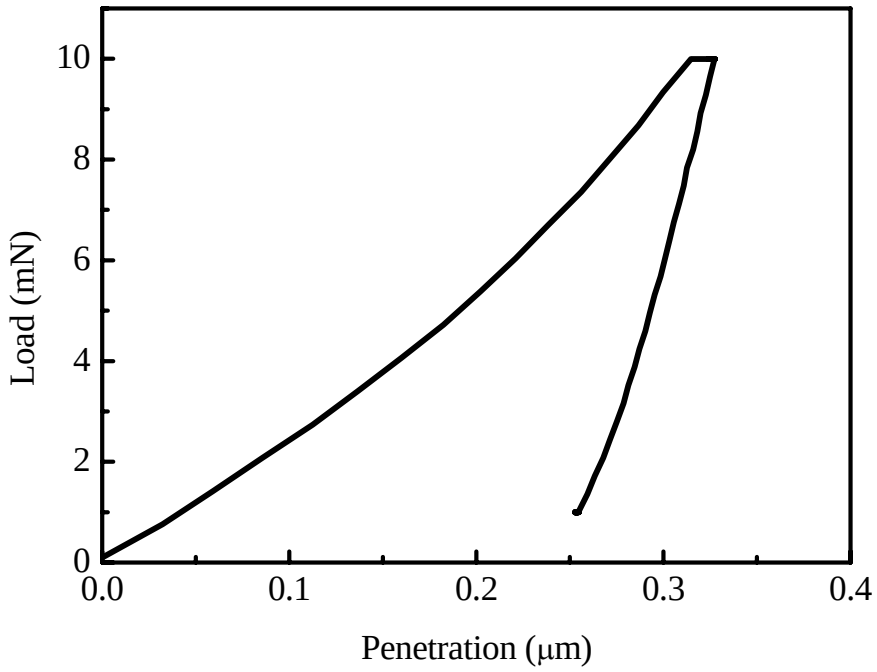

Fig. 4-2 Typical experimental data of Procedure A.

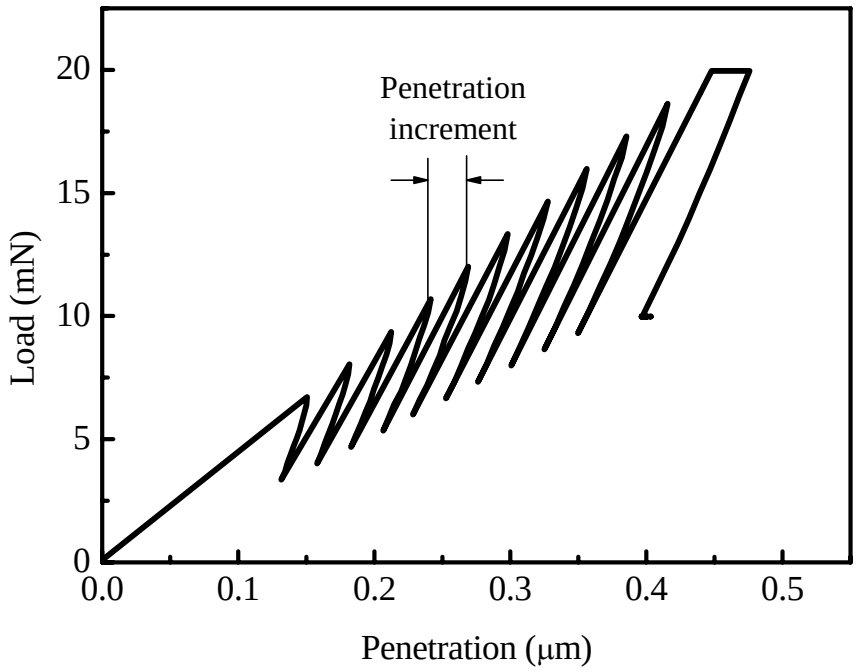

Fig. 4-3 Typical experimental data of Procedure B.

Procedure B is a multi-loading/partial-unloading procedure. In this procedure, the indenter undergoes unloading at each increment until 50% of the current load is approached, as illustrated in Figure 4-3. For homogeneous materials, the penetration increment between each load step is evenly distributed due to the linear relation between the load and displacement for wedge indentation.

The indentation experiments are under load-control and the load-penetration data are recorded at each increment during loading/unloading sections. A typical impression of a wedge indentation is illustrated in Figure 4-4, and the dimensions of the indentation impression are shown in the figure.

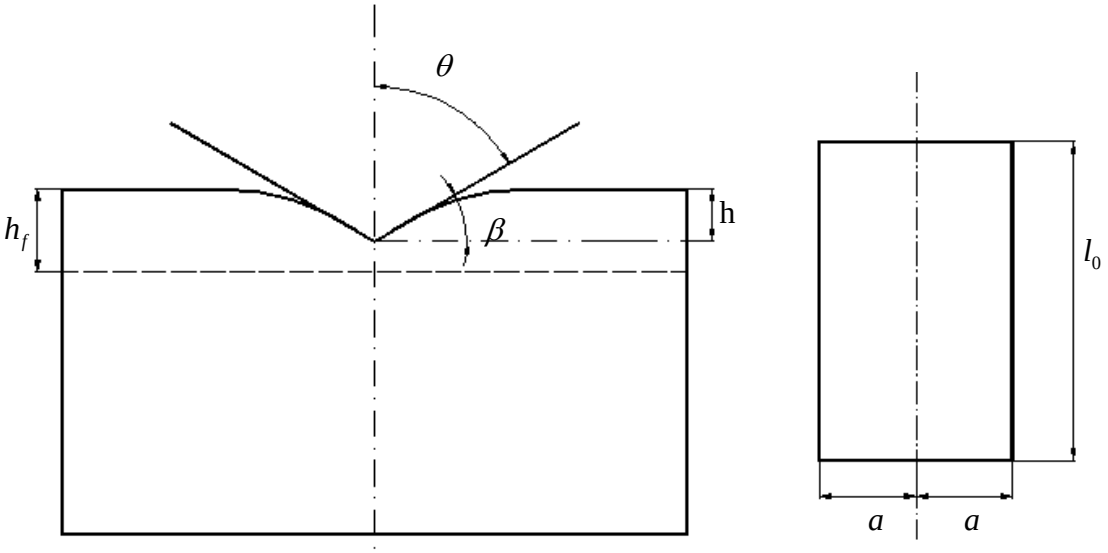

Fig. 4-4 Schematic illustration of wedge indentation on a thin film system: (a) side view, and (b) top view of the indentation impression.

h is the penetration depth of the indenter; h_f is the thickness of the film; θ is the semi-included angle of the indenter; l_0 is the length of the impression, which is equal to that of the indenter tip; and a is the half-width of the impression.

4.4. Analysis Scheme

4.4.1. Reduced Modulus and Hardness from Experimental Data

As discussed previously in Chapter 2, the initial portion of the unloading curve can be modeled as an elastic solid indented by a rigid wedge tip. Thus, the mean pressure p_m is given by [5]:

$$p_m = \frac{E_r \cot\theta}{2(1-\nu^2)} \tag{4.4.1}$$

where E_r and ν are the reduced modulus and Poisson's ratio of the material indented; and θ is the semi-included angle of the wedge indenter.

The hardness is defined as:

$$p_m = \frac{P}{A} \tag{4.4.2}$$

where the projected contact area $A = 2al = 2hl_o / \tan\beta$. Here, $l_o = 4.206\mu$m is the length of the wedge indenter and $\beta = 30^\circ$ is the inclination angle of the wedge face to the surface of the solid ($\beta = 90^\circ - \theta$). Thus, we have:

$$P = \frac{E_r \cot\theta}{2(1-\nu^2)} A = \frac{l_0}{(1-\nu^2)} E_r h \tag{4.4.3}$$

By linearly fitting the initial part of unloading curve, we obtain $P = Ch$ and the slope is:

$$C = \frac{l_0}{(1-\nu^2)} E_r \tag{4.4.4}$$

Therefore, the reduced modulus (defined in Chapter 2, Eq.(2.2.1)) of the whole system can be obtained as:

$$E_r = \frac{(1-\nu^2)}{l_0} C \tag{4.4.5}$$

Meanwhile, the hardness (i.e., mean pressure) can be calculated by:

$$p_m = \frac{P}{A} = \frac{P \tan \beta}{2hl_o} \tag{4.4.6}$$

4.4.2. Indentation Tip Area Correction

The analytical methods described above are based on the assumption that the indentation tip is geometrically perfect and in full contact with the specimen during the whole indentation procedure. However, the tip is never perfect in real cases and for a wedge indenter, misaligment always exists, especially during the initial contact of the indentation. All of these factors will affect the true contact area, and thus, the determination of the elastic modulus, hardness, and yield strength, etc. Inspired by the standard method [4] used to calibrate the indenter area function during normal nanoindentation tests with a Berkovich tip, we calibrate the effective projected contact area of wedge indentation as follows:

We first choose a reference material, a bulk aluminum (Al) block. The reason to use this material rather than fused silica, the commonly-used reference material for nanoindenter, is that fused silica may be too hard and may damage the wedge indenter.

Then we indent the Al bulk with the multi-loading/partial-unloading process (Procedure B). By fitting the initial part of the unloading curve at each step, we obtain the reduced modulus at different indentation depths:

$$E_r(h) = C(h)\frac{(1-\nu^2)}{l_0} \tag{4.4.7}$$

where $C(h)$ is the slope of the initial part of unloading curve at each step; and

$\nu = 1/3$ is the Poisson's ratio.

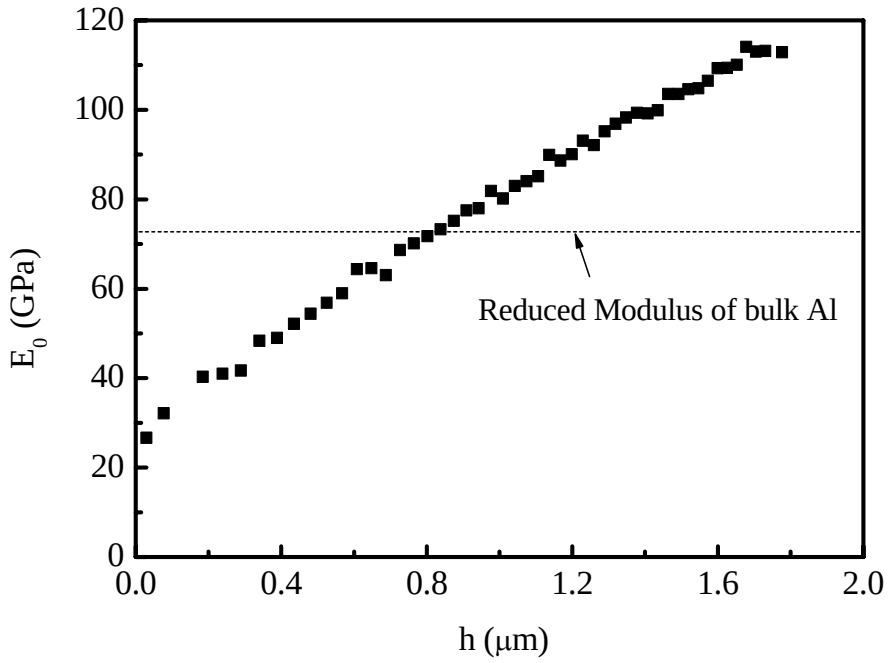

Fig. 4-5 Uncorrected reduced modulus E_0 versus penetration for bulk Al.

Figure 4-5 shows the uncorrected reduced modulus E_0 versus the penetration depth, it is clear that the reduced modulus increases with the penetration depth. However, for a bulk material, the reduced modulus should be independent of penetration depth. In the case of aluminum, the Young's modulus and Poisson's ratio are 68.3GPa and 0.33, respectively [6]. Thus the reduced modulus can be calculated from Eq.(2.2.1), with the Young's modulus and Poisson's ratio for diamond being 1140GPa and 0.07, respectively:

$$E_{r(AL)} = \frac{1}{\frac{(1-\nu_{s(AL)}{}^2)}{E_{s(AL)}} + \frac{(1-\nu_i^2)}{E_i}} = 72.0GPa$$

Therefore, we derive the correction factor as a function of the indentation depth as:

$$\alpha(h) = \frac{E_{r(AL)}}{E_0} \tag{4.4.8}$$

The reduced modulus calculated directly from fitting the initial unloading curve should be corrected by this factor α according to the penetration depth so that the effects of imperfection in the tip geometry and contact area are taken into account. This procedure was proposed when performing standard nanoindentation tests by using UMIS nanoindenter [3]. We hereby adopt the same procedure for the correction of the wedge indentation test.

The average Young's modulus of the bulk aluminum of ten indentation sites after calibration is 66.91±7.13GPa. Table 4-2 gives the corrected Young's modulus of other bulk materials tested (average of 10 indentation sites). However, we do not have enough data to make comparison with those in literatures at this stage.

Table 4-2 Young's modulus (GPa) of bulk materials after calibration.

Cu	Cu (annealed)	Ni
101.49±13.37	74.82±14.38	154.15±26.47

With the confidence obtained from the wedge indentation of the bulk materials, we can now turn our attention to thin film systems. For the thin film systems tested, the same correction method is applied. However, the Young's modulus is still found to vary with penetration depth after calibration due to the substrate effect. This issue will be presented and discussed in more details in the next section.

4.4.3. Substrate Effect

By substituting the calibrated reduced modulus into Eq.(2.2.1), we can determine the modulus of the specimen. However, for the thin film system, the modulus is naturally affected by the substrate during the indentation test. To obtain the properties of the film, we have to separate the substrate effects.

By re-arranging Eq.(4.4.3), we have $\frac{P}{h} = \frac{l_0}{(1-\nu^2)} E_r$. Since E_r is a constant for a homogeneous material, the value of P/h should be a constant and independent of penetration depth as well. Therefore, by re-plotting the load-penetration curve as P/h versus h, we can determine how the substrate affects the measured properties during indentation. When the value of P/h is approximately a constant in certain shallow indentation range, the values of the reduced moduli derived from the load-penetration curve within this range are insignificantly affected by the substrate. Therefore, the measured moduli should mainly reflect the properties of the film only. The parameter P/h can be defined as effective stiffness, similar to that of the stiffness in tensile testing.

During the analysis of the indentation data, we first determine the range of penetration depth in which the value of P/h is approximately a constant. Then, we calculate the average Young's modulus (calibrated) and hardness within this range as the properties of the thin film.

This approach has been approved effective in the analysis of normal Berkovich indentation of low-k films [7-8]. The validity of applying this approach for wedge indentation will be confirmed by the simulation and the experimental results

presented later.

4.4.4. Yield Strength of Thin Film

With the Young's modulus and hardness of the film obtained by the procedures described above, we then employ Johnson's model [2] discussed in Chapter 2 to calculate the yield strength of the film. Johnson [2] proposed a relation between Young's modulus, hardness and yield strength stated as equation (2.2.12):

$$\frac{\overline{p}}{Y} = \frac{1}{\sqrt{3}}\left\{1 - \ln(5 - 4\nu) + \ln\left[\frac{4E}{\pi Y}\tan\beta + 3(1 - 2\nu)\right]\right\}$$

for a blunt wedge indenter and materials having a low ratio of elastic modulus to yield strength. The model was originally proposed for bulk materials based on Hill's solution [9] for the problem of a cavity in an elastic-plastic material being expanded by an internal pressure. In addition to the blunt wedge indenter and materials having a low ratio of elastic modulus to yield strength required by the model itself, we apply this method to derive yield strength of the thin film when another two conditions are met: 1) the indentation depth is shallow so that the effects from the substrate are negligible; and 2) the elastic-plastic boundary of deformation lies at a radius of c within the film so that Hill's solution is valid, i.e., $c < h_f$, where h_f is the film thickness.

After obtaining the Young's modulus, hardness and yield strength of the film, we can perform simulations for the system to determine the interface adhesion properties.

4.5. Results and Discussions of Single Layer Thin Film System

4.5.1. Sample Fabrication

SiOC low-k films (BD) are deposited on Si by a parallel plate PECVD system [7]. The source gases are $((CH_3)_3SiH, 3MS))$ and O_2, of which the flow rate ratio $3MS/O_2$ is fixed at 6. The total pressure is maintained at 4 Torr while ratio-frequency power at 600W. The film thicknesses estimated from the deposition time and the deposition rate are 200nm and 500nm. The Si substrates, which have an oxide layer of approximately 5nm thick on the surface, are heated at 350ºC during the deposition.

4.5.2. 200nm BD Film Deposited on Silicon

4.5.2.1. Indentation Response

Since our primary interest focuses on the interface adhesion properties and delamination process, we firstly investigate the influence of interface delamination on the load-penetration curve, as well as on the effective stiffness of the system. Indentation tests with different maximum loads have been performed. The data obtained from Procedure B have been used to monitor the changes of the effective stiffness continuously.

A typical load versus penetration curve is shown in Figure 4-6. The test was performed under load control and is applied in 50 steps to a maximum load of 15mN. Each step contains a loading and a partial unloading section as well as a dwell time of 0.5 second between each step. There are several interesting features in Figure 4-6, which will be discussed in association with the corresponding effective stiffness and

SEM observations.

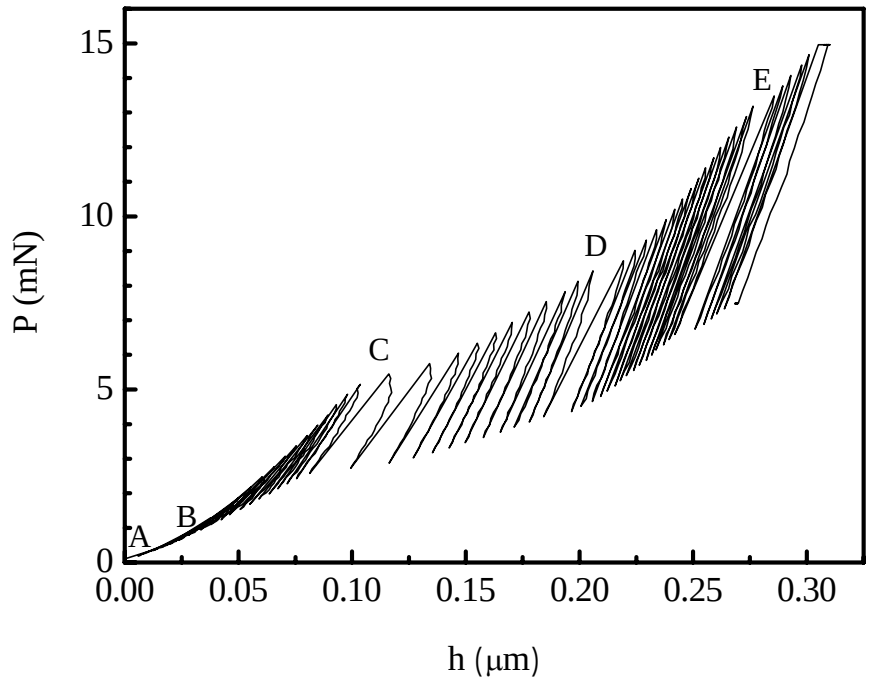

Fig. 4-6 Load versus penetration with a maximum load of 15mN.
The letters present several characteristics that will be discussed in the text.

At the initial stage of the test (A→B), the penetration depth increases almost linearly with increasing load of each step and the effective stiffness of the system remains approximately a constant as shown in Figure 4-7. From the discussion presented in Section 4.4.3, we therefore believe that within this range, the indentation response is insignificantly affected by the hard substrate (silicon), thus mainly reflects the property of the film. When the penetration depth increases further (B→C), the load-penetration curve becomes superlinear, and the reduced modulus of the system increases with increasing penetration depth. The increase is mainly due to the increasing substrate effect when penetration proceeds. At these stages (A→B→C), no

permanent damage such as an indent has been incurred to the thin film system. Hence no indentation impression has been observed under SEM.

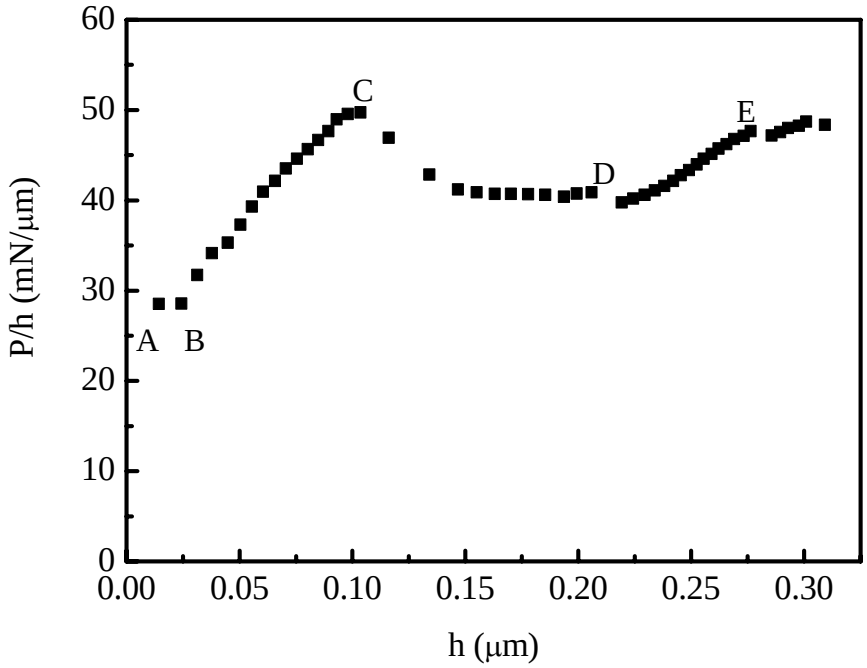

Fig. 4-7 Effective stiffness versus penetration.

The letters present several characteristics that will be discussed in the text.

When the indenter penetrates beyond 0.104μm (point C), the increment of the penetration depth becomes larger and unevenly distributed (C→D). However, the increment of the load of each step remains the same as that of the previous stage (B→C), indicating a dramatic decrease at point C in the effective stiffness of the system. Undoubtedly, this sudden decrease reflects the irreversible failure induced in the thin film system by the indentation. However, from the SEM images (as shown in Figure 4-8) obtained within this stage at the penetration depth of approximately 0.15μm, no surface crack outside indentation impression is observed. This implies that the possible failure most likely occurs at the interface. The cracks observed at the

center of the impression are probably the film cracks at the indenter tip during the unloading process.

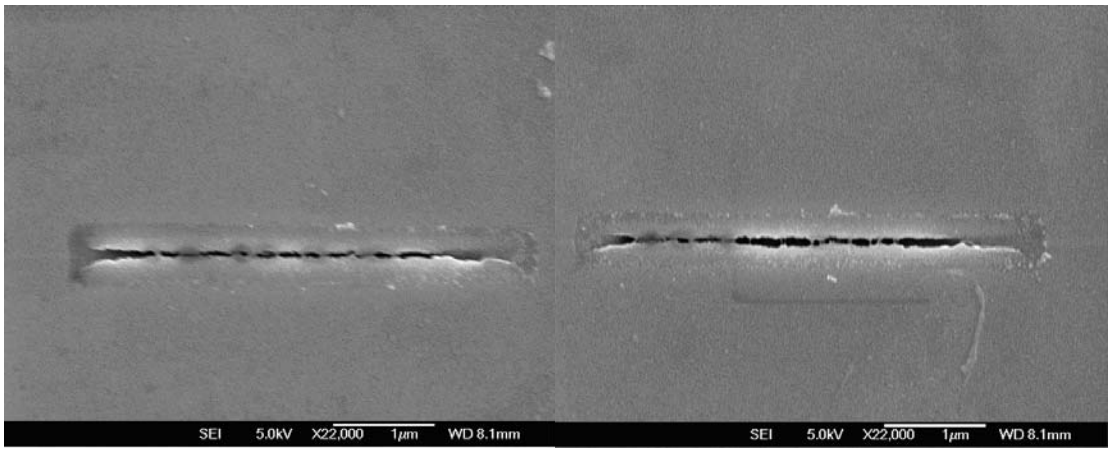

(a) (b)

Fig. 4-8 SEM images of the indentation impressions when the penetration depth is within the film at (a) 0.147μm, and (b) 0.155μm.

With further increase in penetration depth, surface crack occurs at a large area surrounding the indenter and the film begins to spall off as shown in Figure 4-9. With respect to the argument of the occurrence of interface delamination, it is reasonable to conclude that the formation of the two spalling patches is the consequence of the propagation of the interface delamination and its interception with the surface.

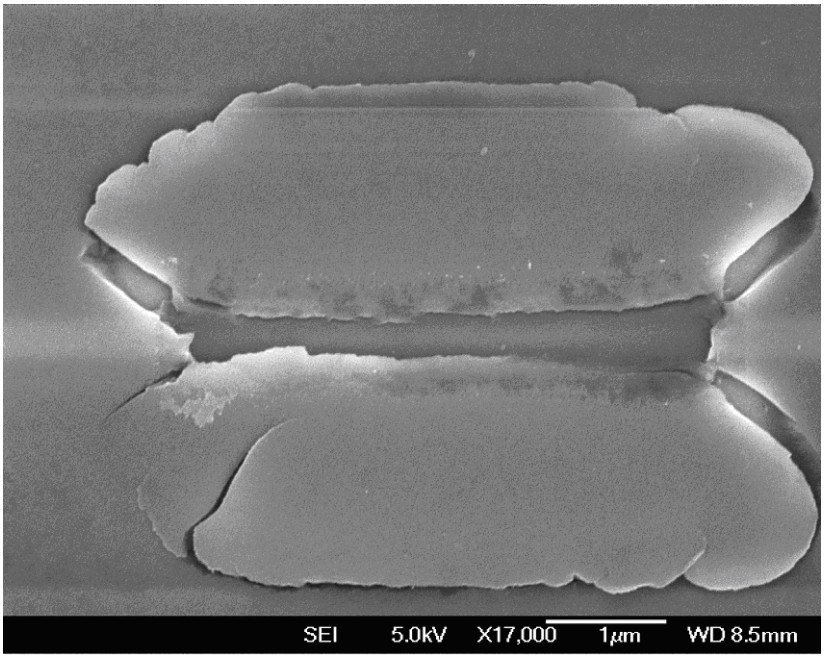

Fig. 4-9 SEM image of the indentation impression when the penetration depth is within the film at approximately 0.175μm.

When the penetration depth reaches 0.2μm (point D), the penetration depth increment at each step decreases (Figure 4-6, D→E) and the effective stiffness of the system increases (Figure 4-7, D→E). It is noticed that the thickness of the film is 200nm, the indenter has penetrated through the film and reached the substrate. Thus, the increase in the effective stiffness is probably due to the increasing contribution of the relatively harder substrate, silicon.

There is another sudden shift in penetration depth when the load is approximately 13.478mN (Figure 4-6, point E), which is probably the result of the total spalling off of the film from the substrate as shown in Figure 4-10.

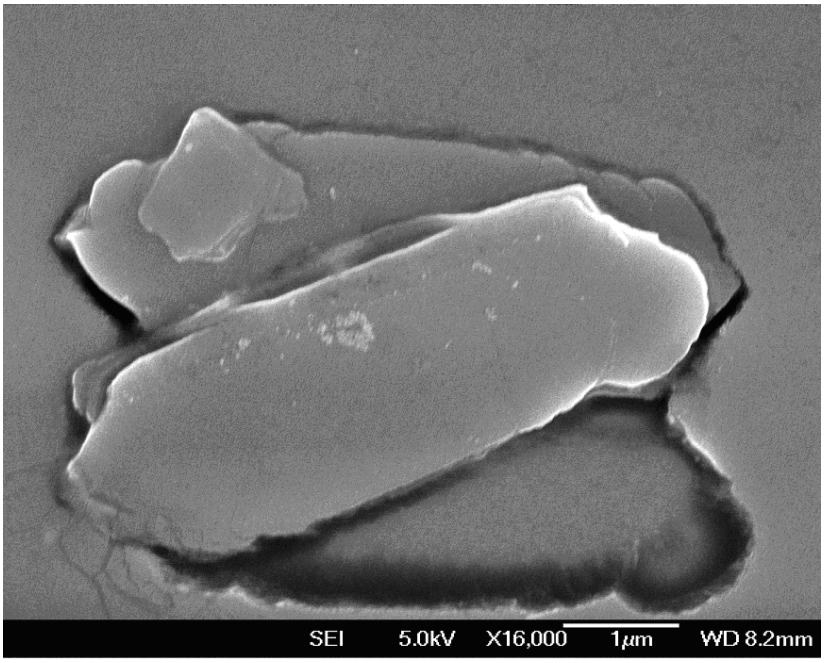

Fig. 4-10 SEM image of the indentation impression when the penetration depth is approximately 0.27μm.

Therefore, the influence of the initiation and propagation of the interface delamination on load-penetration curve and the effective stiffness can be summarized as follows: 1) the sudden increase and uneven distribution of penetration increment indicate the onset of interface delamination; 2) further propagation of the interface delamination leads to a decrease in the effective stiffness of the system; and 3) the effective stiffness increases again when the indenter penetrates through the film and into the substrate due to the increasing substrate effect, when the substrate is relatively harder.

4.5.2.2. Properties of the 200nm BD Thin Film

In order to study the substrate effect and determine the properties of the BD film,

we perform shallow indentations with a maximum load of 5mN.

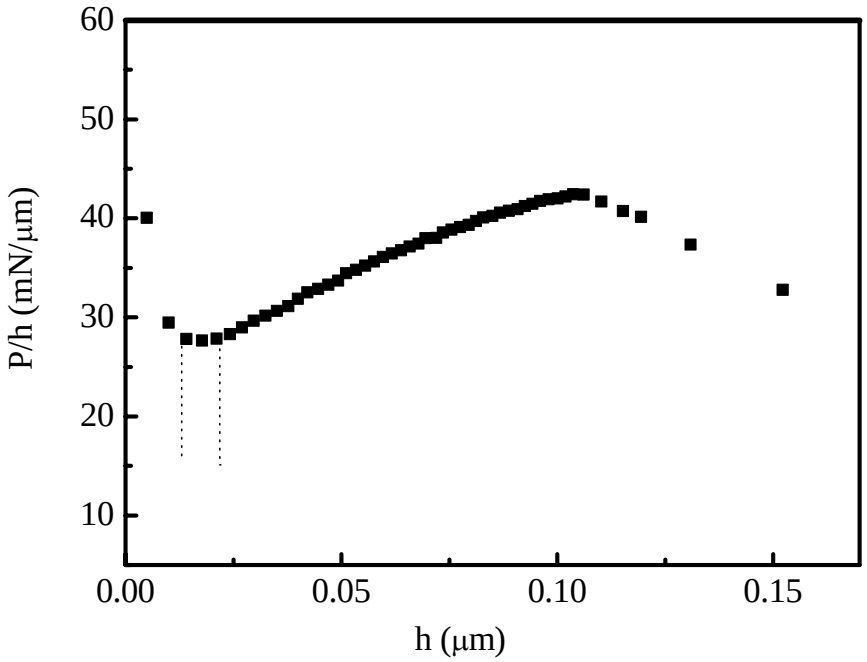

Fig. 4-11 Effective stiffness versus penetration.
The region marked by the dashed lines is used to determine the properties of the film.

From the P/h versus h curve shown in Figure 4-11, we can identify a small range between the third and the fifth indentation step, in which the values of effective stiffness P/h are approximately a constant of 20.77mN/μm. Based on the analysis presented in Section 4.4.3, it is concluded that the properties derived from the data within this range should reflect the properties of the 200nm BD film. We neglect the first two points here since they are not reliable due to the limitation of the machine resolution. This range is less than 12.5% of film thickness, which meets one of the requirements mentioned in Section 4.4.4 for the application of Johnson's model [2]. In absence of the technique for measuring the plastic zone during indentation, we can assume that the plastic zone is a semicircle within the film due to the shallow

penetration depth and the symmetry of the system. The properties of the film derived from the experimental data of ten indentation sites are listed in Table 4-3.

Table 4-3 Properties of the 200nm BD film.

Reduced modulus	13.30 ± 0.84 GPa
Young's modulus	11.97 ± 0.76 GPa
Hardness	1.90 ± 0.05 GPa
Yield strength	1.24 ± 0.08 GPa

4.5.3. 500nm BD Deposited on Silicon

4.5.3.1. Indentation Response: Corner Crack

For 500nm BD film deposited on silicon, we first observe cracks at the corner of the indentation impression as shown in Figure 4-12. From the corresponding load-penetration curves in Figure 4-13 and Figure 4-14, we find that the development of the corner crack has little influence on the load-penetration curve. As a consequence, there is little effect on the effective stiffness as shown in Figure 4-15 and Figure 4-16. Probably, there is no interface delamination at this stage.

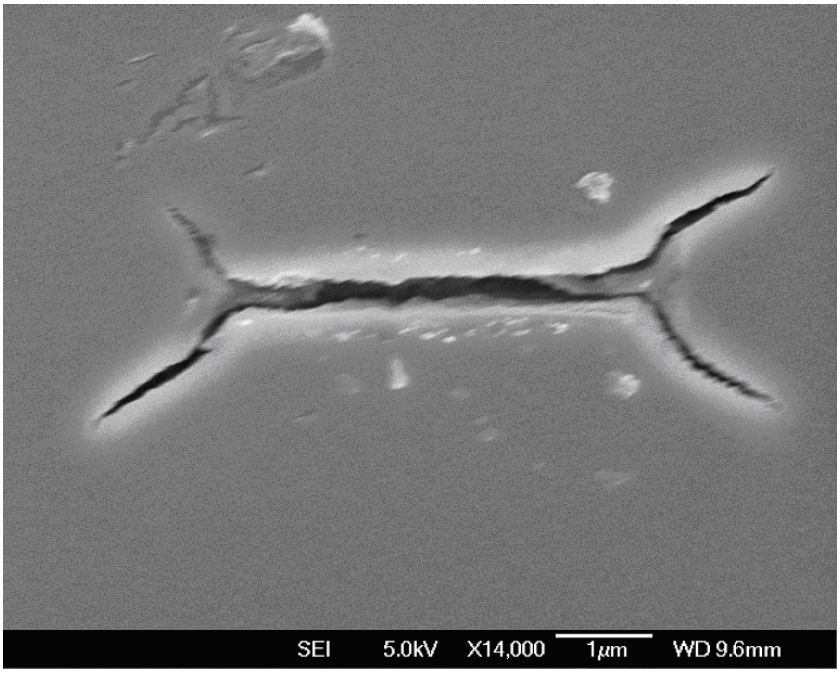

(a)

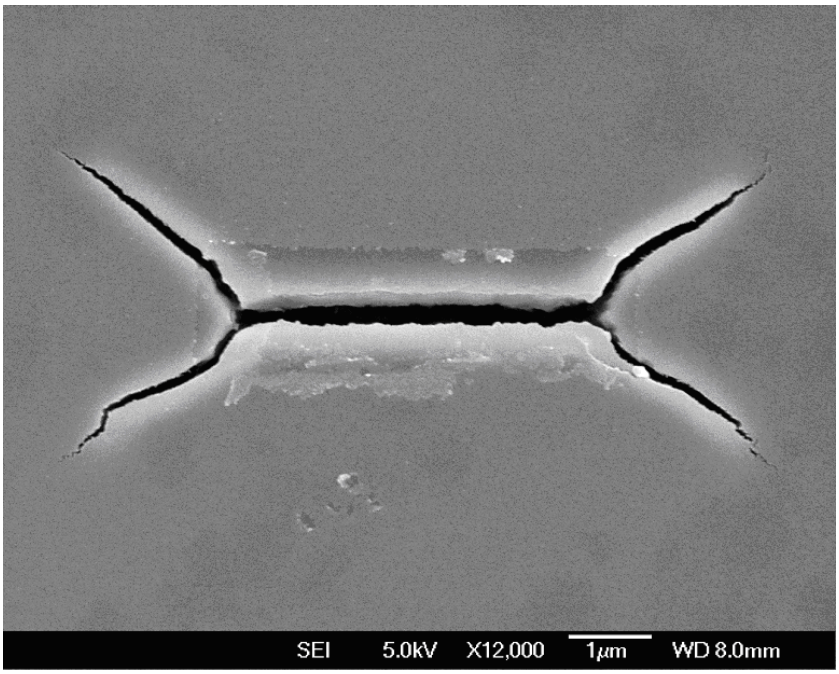

(b)

Fig. 4-12 SEM images of indentation impressions when the penetration depth is at (a) 0.179μm, and (b) 0.174μm.

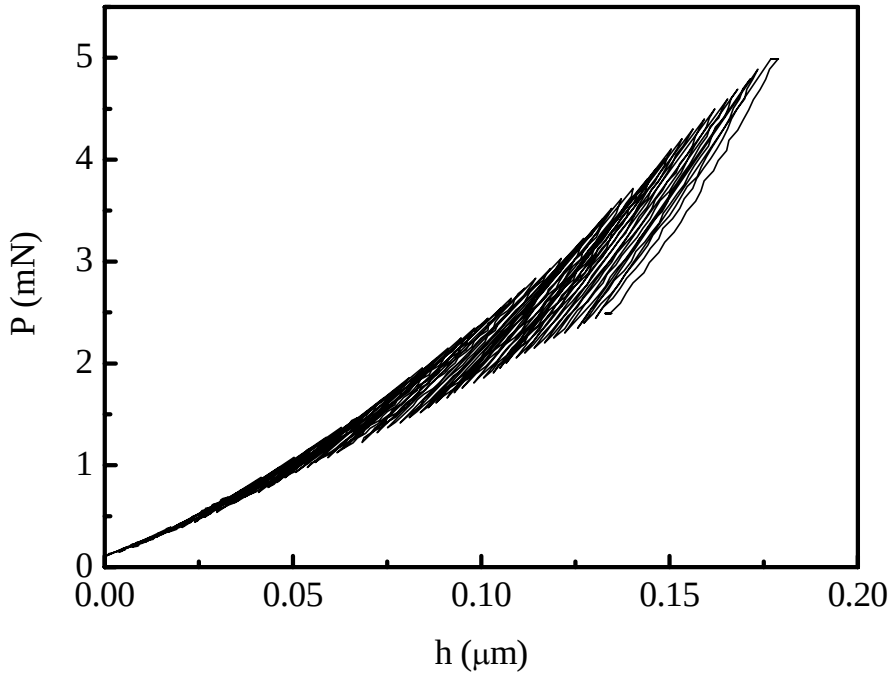

Fig. 4-13 Load versus penetration curve corresponding to Figure 4-12 (a).

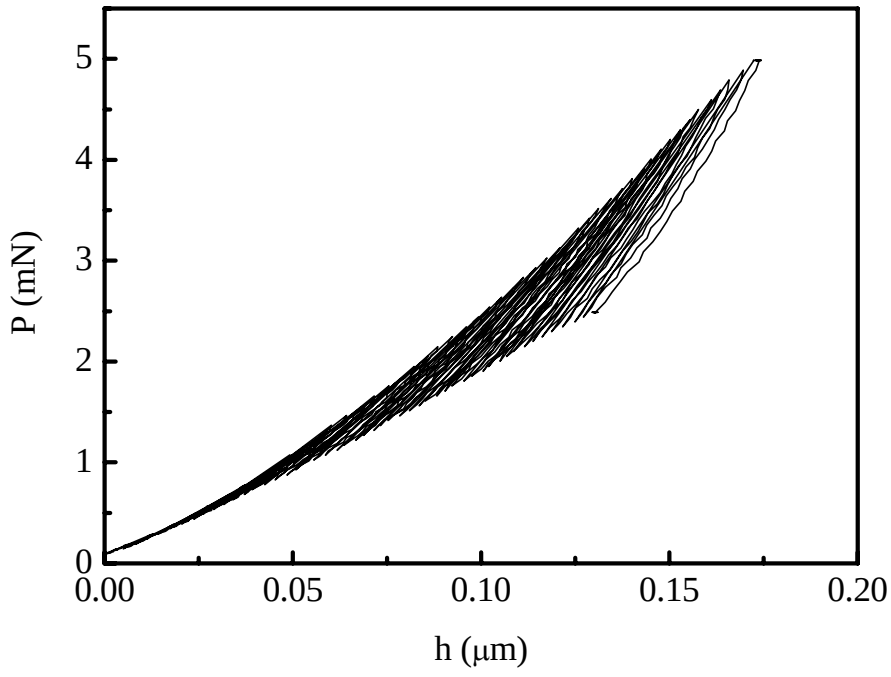

Fig. 4-14 Load versus penetration curve corresponding to Figure 4-12 (b).

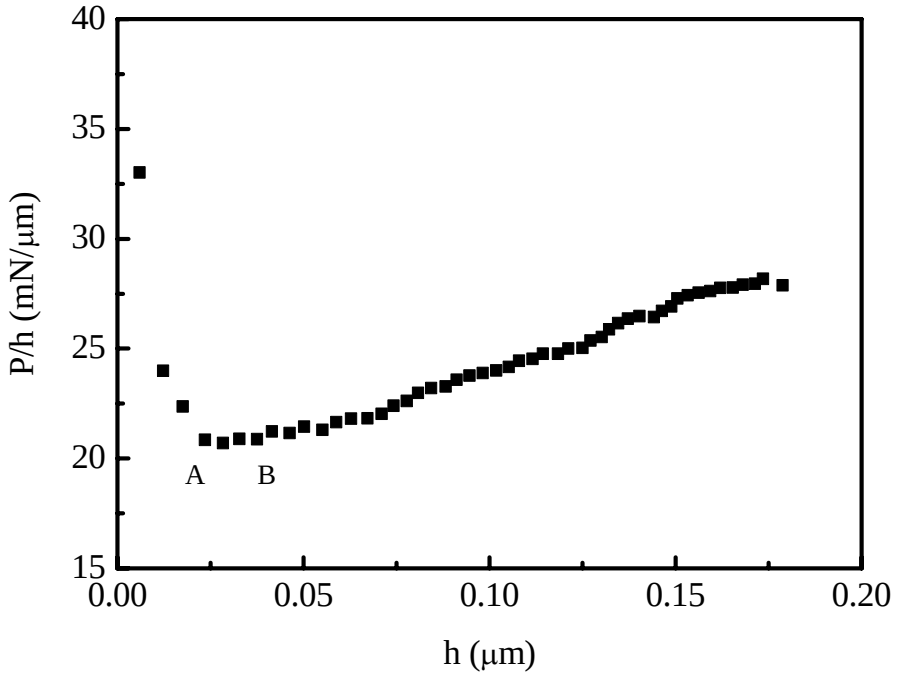

Fig. 4-15 Effective stiffness versus penetration curve corresponding to Figure 4-12 (a). Range [A, B] is discussed in Section 4.5.3.3.

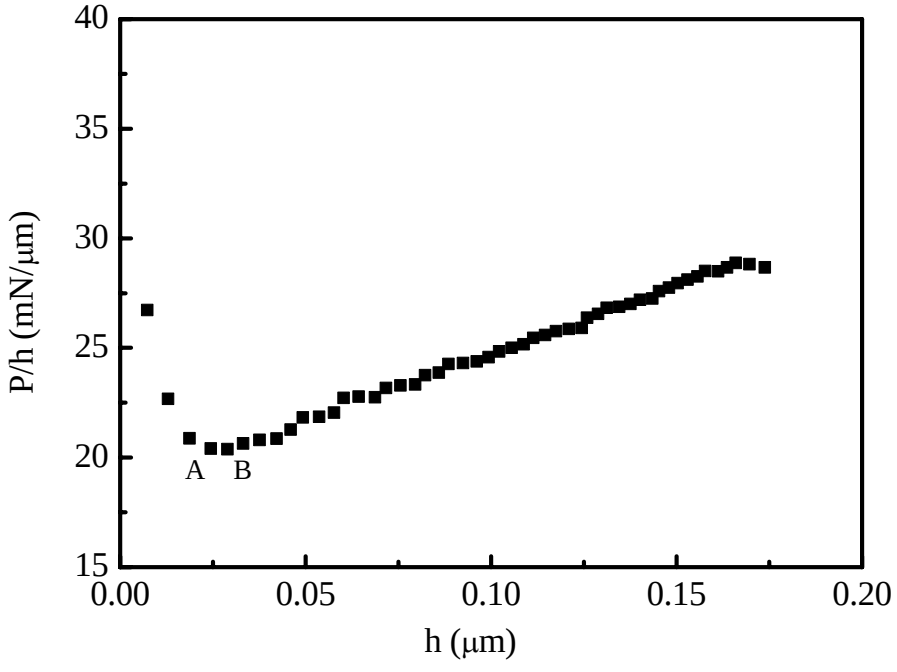

Fig. 4-16 Effective stiffness versus penetration curve corresponding to Figure 4-12 (b). Range [A, B] is discussed in Section 4.5.3.3.

4.5.3.2. Indentation Response: Interface Delamination

When we increase the indentation load, the characteristics of the P-h curve change significantly. Figure 4-17 shows the P-h curve obtained with a maximum load of 20mN, and Figure 4-18 shows the corresponding effective stiffness of the specimen.

Comparing with that of the 200nm BD/Si system, we find similar tendencies: an initial linear range (A→B) reflects the properties of the thin film; no permanent damage has been incurred to the system during stage A→C; the effective stiffness increases due to the substrate effect in this stage, and then decreases dramatically at a penetration depth of 0.246μm (C→D) due to the initiation and propagation of the interface delamination, which can be observed by SEM as shown in Figure 4-19 (a). When the indenter penetrates into the substrate and beyond the depth of 0.549μm (D→E), the stiffness increases again, reflecting the increasing influence of the harder substrate, silicon. The sudden increase in penetration increment at about 0.624μm (point E) is probably the result of spalling off the film as shown in Figure 4-19 (b).

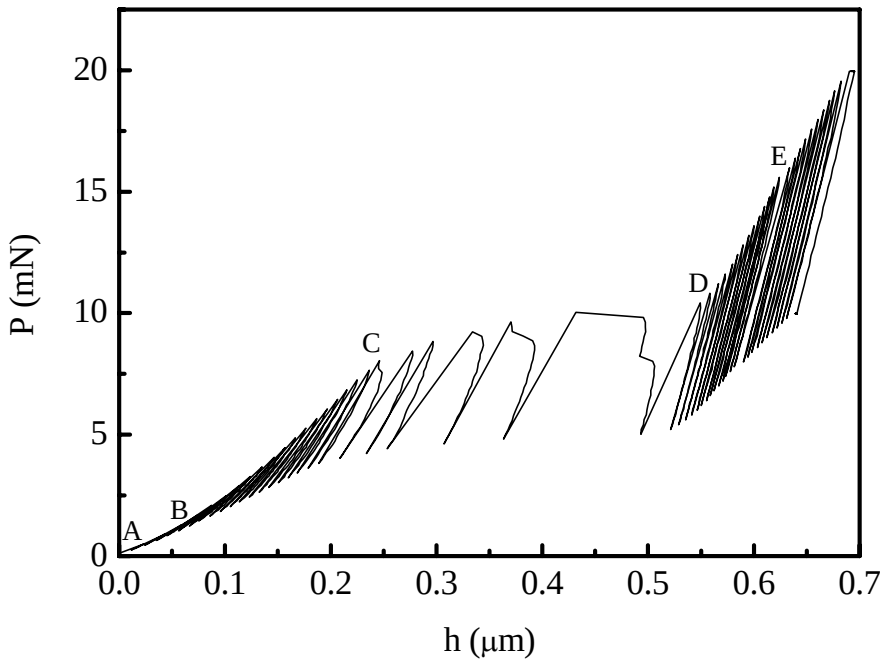

Fig. 4-17 Load versus penetration with a maximum load of 20mN.

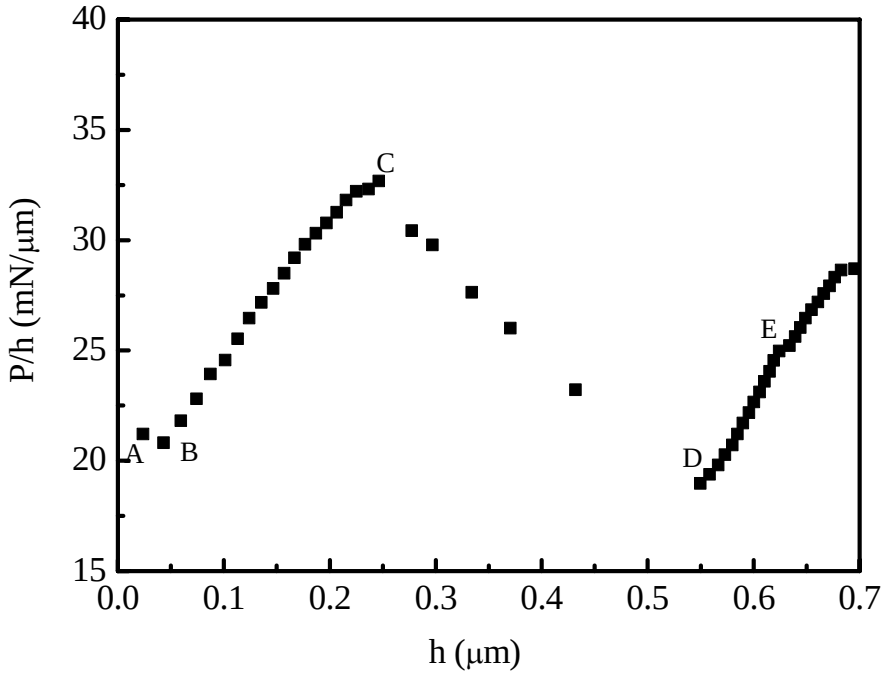

Fig. 4-18 Effective stiffness versus penetration corresponding to Figure 4-17.

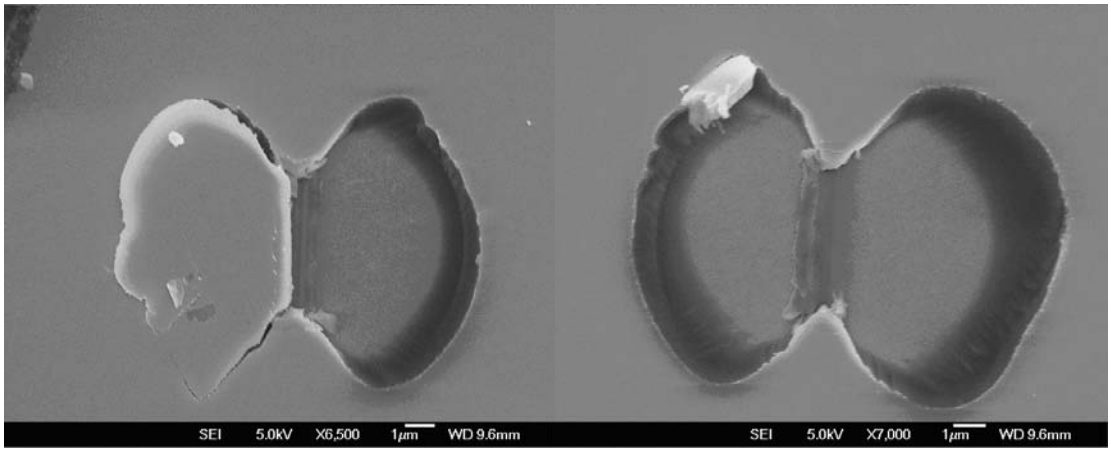

(a) (b)

Fig. 4-19 SEM images of indentation impressions when the penetration depth is within the film at (a) 0.555μm, and (b) 0.695μm.

From the above discussion, it may be concluded that: 1) the sudden increase and the uneven distribution of the penetration increment indicate the onset of interface delamination; 2) further propagation of the interface delamination leads to a decrease in the effective stiffness of the system; and 3) the effective stiffness increases again when indenter penetrates through the film and into the substrate due to the increasing substrate effect, when the substrate is relatively harder.

4.5.3.3. Properties of the 500nm BD Thin Film

Similar to the case of 200nm BD/Si, we perform shallow indentations with a maximum load of 5mN to study the substrate effect. We choose the constant stiffness range (refer to range A→B in Figure 4-15 and Figure 4-16) to calculate the properties of the thin film listed in Table 4-4. The range is less than 10% of the film thickness. The assumption that the plastic zone is a semicircle within the film is made to apply

Johnson's model [2].

Table 4-4 Properties of the 500nm BD film.

Reduced modulus	10.23 ± 0.52 GPa
Young's modulus	9.18± 0.48 GPa
Hardness	1.62 ± 0.06 GPa
Yield strength	1.13 ± 0.06 GPa

These values are slightly lower than those of the 200nm BD film discussed previously (refer to Table 4-3), which is probably due to: 1) the different film thickness, grain size, etc; and 2) the 200nm BD film may be affected more by the substrate due to the thinner film thickness.

4.5.3.4. Simulation of the 500nm BD/Si System

The BD/Si system is chosen due to the increasing interests in low-k dielectric material and the universal application of silicon substrate, especially in electronic devices.

With the properties such as Young's modulus and yield strength of the 500nm BD film obtained from indentation experiments above, we can perform simulations for this thin-film/substrate system to determine the interface adhesion properties of the system and make comparison with the experimental results.

The simulations are performed with initial parameters obtained from experiments

as listed in Table 4-4. For the Si substrate, $E_s = 112.4\text{GPa}$ [6] and $\sigma_{ys} = 3.10\text{GPa}$ are used. $D_s = 0$ so that the Si substrate is treated as an elastic-plastic material. All these parameters in the simulations are normalized by $\sigma_{yf} = 1.13\text{MPa}$ and a length of $\Delta_0 = 0.1\mu\text{m}$ since we are interested thin film structures in micrometer levels. The experimental data are normalized following the same scheme for the sake of comparison between the simulation and experimental results.

By directly varying the pre-set interface strength and interface energy in the simulations, we can make the critical moment as close to that of the experiment as possible. The simulation results suggest that if the interface strength $\hat{\sigma} = 0.045\sigma_{yf}$ and interface energy $\Gamma_0 = 0.0016\sigma_{yf}\Delta_0$ are chosen for the interface adhesion properties of the 500nm BD/Si system, the relative error of the critical penetration

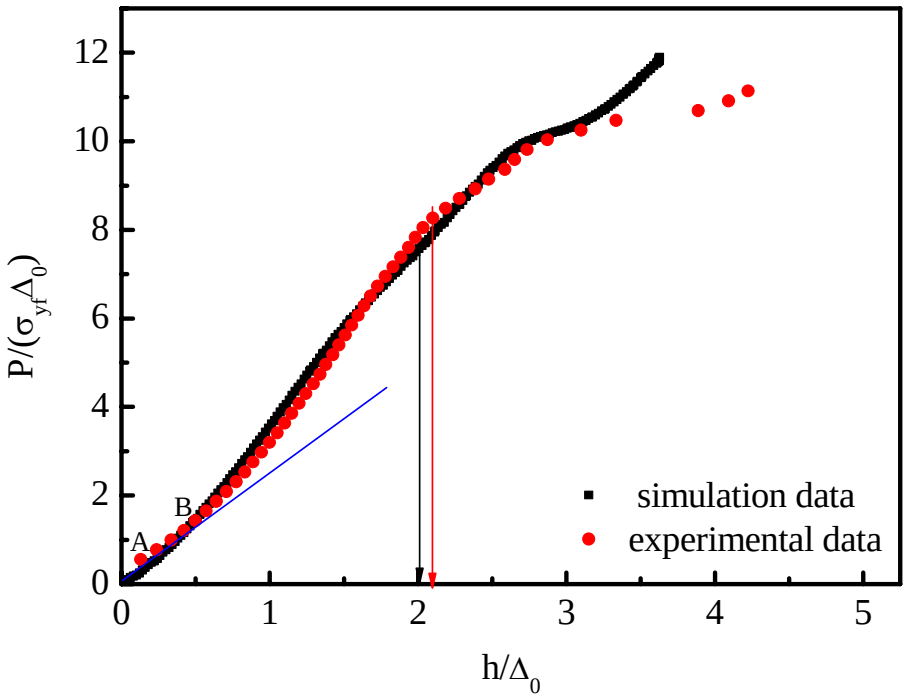

Fig. 4-20 Simulation of the 500nm BD/Si system.

The arrows correspond to the critical moments. A→B reflects the properties of the film.

depths between the simulation and experiment is within 5%. Figure 4-20 shows the good agreement between the simulation and experimental results. The initial linear part (A→B), which is insignificantly affected by the hard substrate, reflects the properties of the BD film. With further indentation, the stiffness of the system increases due to the increasing influence from the substrate and the load-penetration curve becomes superlinear, which has been discussed in previous subsections. The interface delamination occurs when the penetration depth reaches approximately $2.005\Delta_0$ in the simulation, or $2.098\Delta_0$ in the experiment. The critical value in the simulation is determined by the stress and strain states of the system, whereas in the experiment, the critical value is determined by the shift of the load-penetration curve, together with SEM observations. We notice that the shape of the simulation curve agrees well with that of the experiment before delamination. However, after delamination, the slope of the simulation curve is slightly higher than that of the experimental one. This is probably due to the overestimation of the effects of strain-hardening in the simulation. The deviation of the simulation curve from the experimental one when the penetration depth is beyond $3.097\Delta_0$ is probably due to the fracture of the film, which is not considered in the simulation model. The good agreement between the simulation and the experiment validates the analysis scheme used to obtain the properties of the thin film, especially the Young's modulus and yield strength.

Alternatively, we can obtain the interface adhesion properties of the system by using the methodology presented in Chapter 3 as well. We can perform a series of

basic simulations of which the critical moments are close to that of the experiment, and then predict the dependence of P_c and P_d on the interface strength $\hat{\sigma}$ and interface energy Γ_0, and finally $\hat{\sigma}$ and Γ_0 can be determined with P_c^e and P_d^e measured in experiment. However, due to the limitation of time, this work will be carried out in future studies.

Figure 4-20 presents one of the most important results of this project. It reveals several important features and implications for characterizing interface adhesion properties by using wedge indentation technique and simulations. Firstly, the traction-separation law is capable of describing the interface adhesion properties. Secondly, there exist clear relationships between indentation measurable quantities and interface adhesion properties. Thirdly, it indicates that the interface adhesion properties, i.e., interface strength and interface energy, can be determined by combining wedge indentation tests and FEM simulations. Although the results are still preliminary, they are very promising and important. With further studies, the proposed method should be improved and applied more widely.

4.6. Results and Discussions of Multi-Layer Thin Film System

4.6.1. Sample Fabrication

Multi-layer thin film systems with four different top layers (50nm barrier low-k films) deposited by PECVD, are investigated. The thin films between the top layer and the Si substrate are

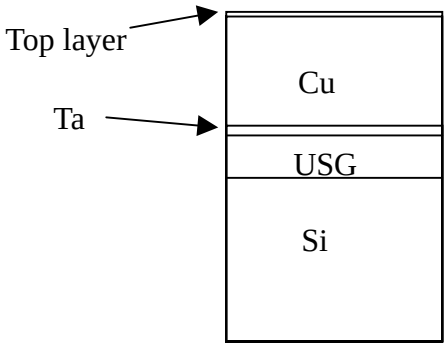

Fig. 4-21 Schematic illustration of the structures of the multi-layer systems.

600nm Cu, 25nm Ta, and 300nm undoped silicate glass (USG). The structures are shown schematically in Figure 4-21 and the deposition parameters of the top layers are listed in Table 4-5 [10].

Table 4-5 Deposition parameters of the barrier low-k films.

Dielectric-cap	Relative dielectric constant	Gases/flow (sccm)	HFRF (watt)	LFRF (watt)	Pressure (Torr)
SiN	7 (±0.2)	SiH_4/500 NH_3/400 N_2/1600	570	430	2.6
SiCO	4.4 (±0.2)	CO_2/3000 4MS/500	500	400	2.5
BLOk™-1	4.6 (±0.2)	He/200 3MS/80 NH_3/160	300	-	3
BLOk™-2	4.9 (±0.2)	He/400 3MS/150	460	-	8.7

4.6.2. Indentation Response

The experiments are performed under load control with multi-loading/ partial-unloading procedures until the pre-set maximum load is achieved. The four multi-layer specimens display similar indentation responses. Conclusions similar to

those of BD/Si systems can be drawn from the analysis of indentation load-penetration curves.

Figure 4-22 shows a load-penetration curve of the multilayer system with SiN as the top layer. There is no significant disturbance in the curve during the initial penetration within 50nm, indicating that no delamination happens within this range. In addtion, there is no surface crack observed by SEM at this stage.

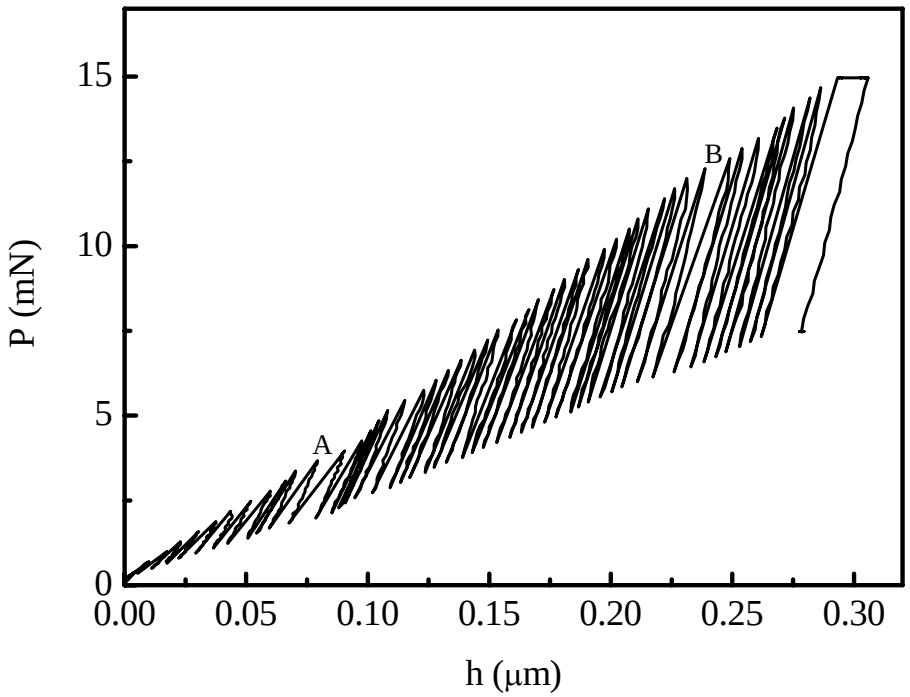

Fig. 4-22 Load versus penetration curve of the SiN system.

With further increasing penetration depth up to 0.079μm (point A), a disturbance occurs and it is probably due to the cracking at the edge of the indentation impression as shown in Figure 4-23.

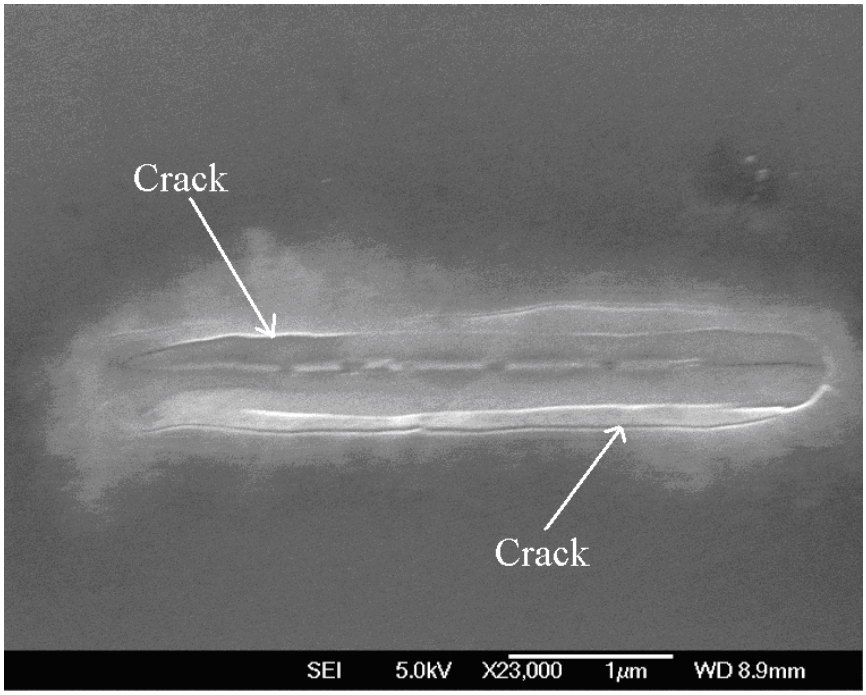

Fig. 4-23 SEM image of the indentation impression when the load level is 5mN.

The second shift in the penetration curve at 0.239μm (point B) is probably due to the bending of the top layer. Since the material for the second layer, copper, is very ductile, it is almost impossible to induce interface delamination between the top layer and the copper layer by the wedge indenter with an included-angle of 120° at the load applied. Thus, it is reasonable to believe that the disturbance in the load-penetration curve is due to the cracking or fracture of the top layer by bending.

Similarly, no delamination happens during the initial penetration within the top layer in the other three systems since no disturbance can be observed in the load-penetration curves shown in Figure 4-24 to Figure 4-26. When the wedge indenter penetrates into the copper layer (refer to Figure 4-27 to Figure 4-29), there are possible cracks of the top layer at the edge of indentation impression at

penetration depth of 0.081μm, 0.127μm, and 0.185μm for SiCO, BLOk^{TM}-1, and BLOk^{TM}-2, respectively.

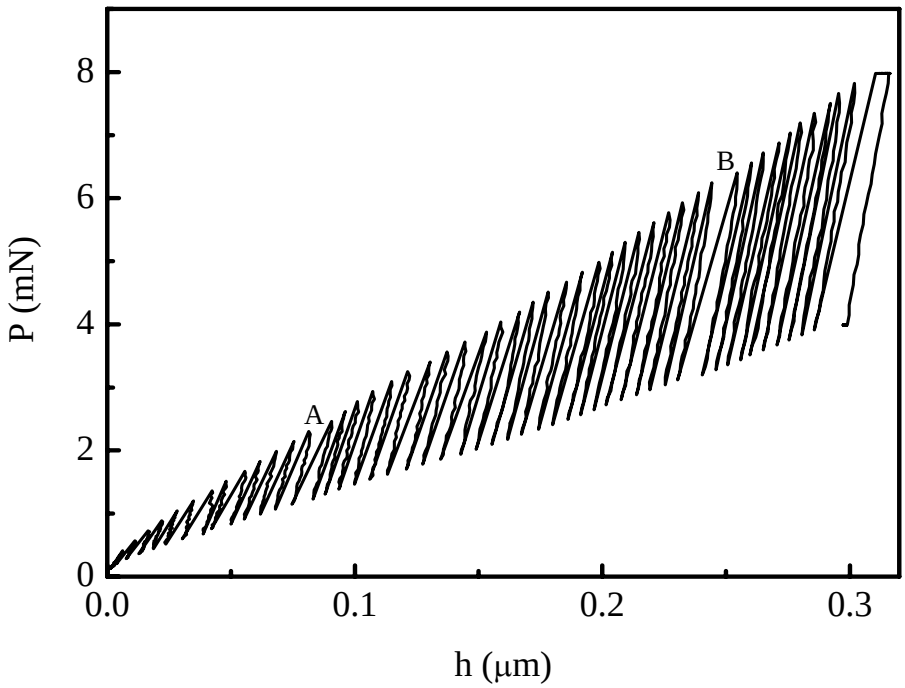

Fig. 4-24 Load versus penetration curve of the SiCO system.

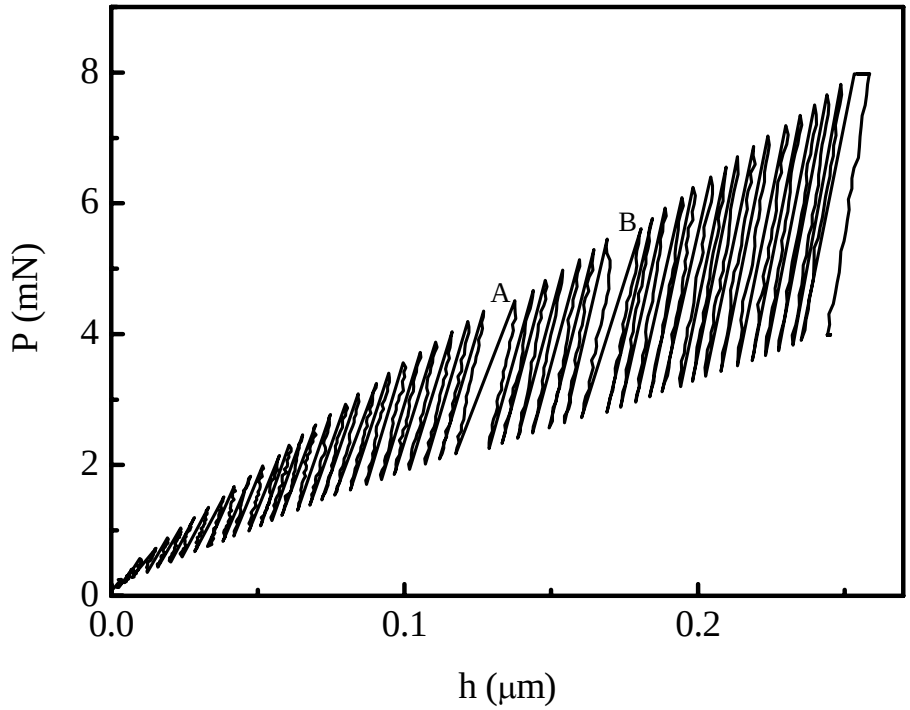

Fig. 4-25 Load versus penetration curve of the BLOk^{TM}-1 system.

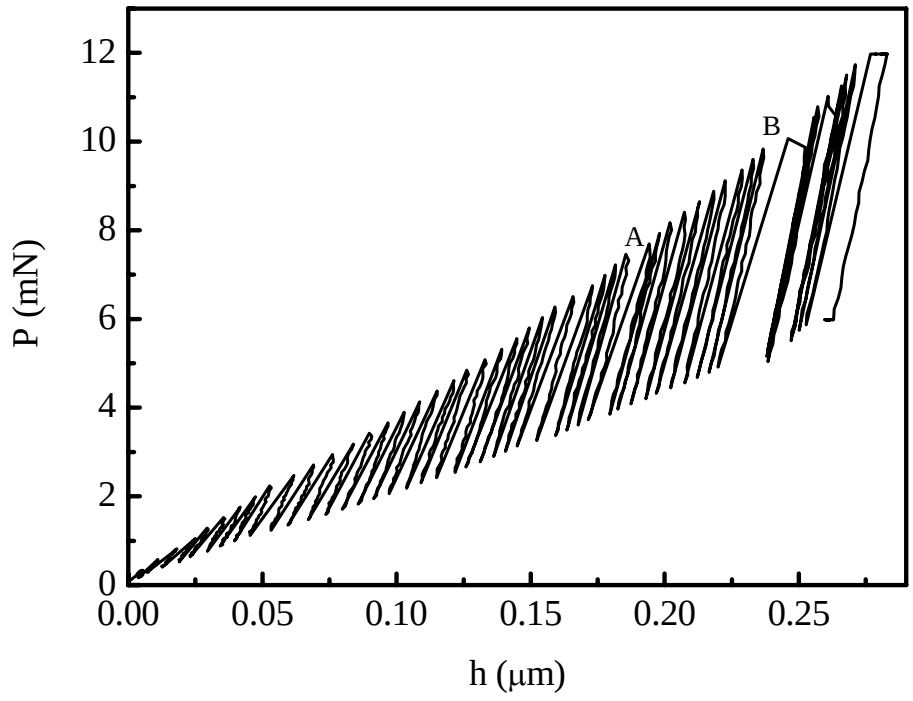

Fig. 4-26 Load versus penetration curve of the BLOk^{TM}-2 system.

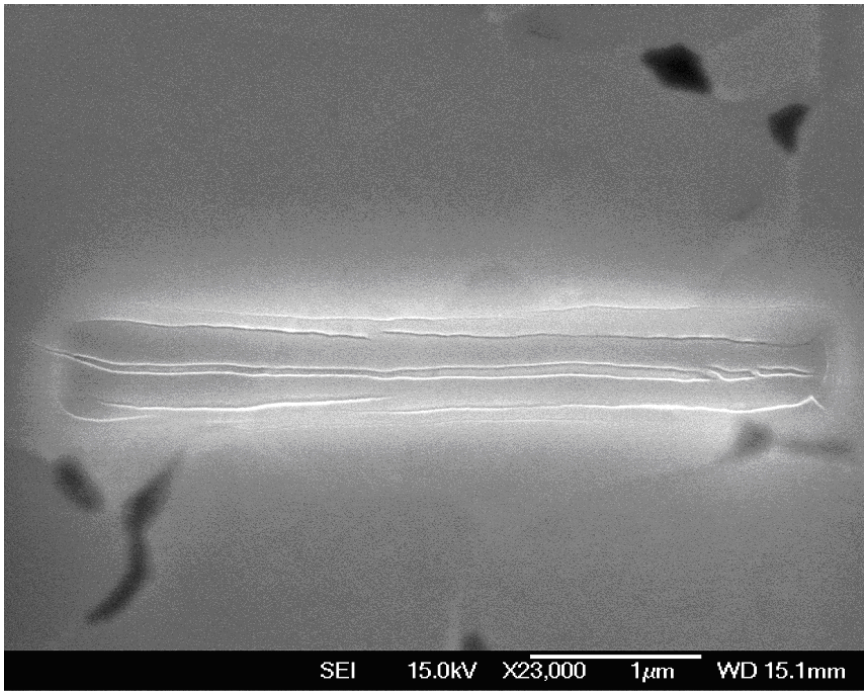

Fig. 4-27 SEM image of the indentation impression of the SiCO system when the load level is 4mN.

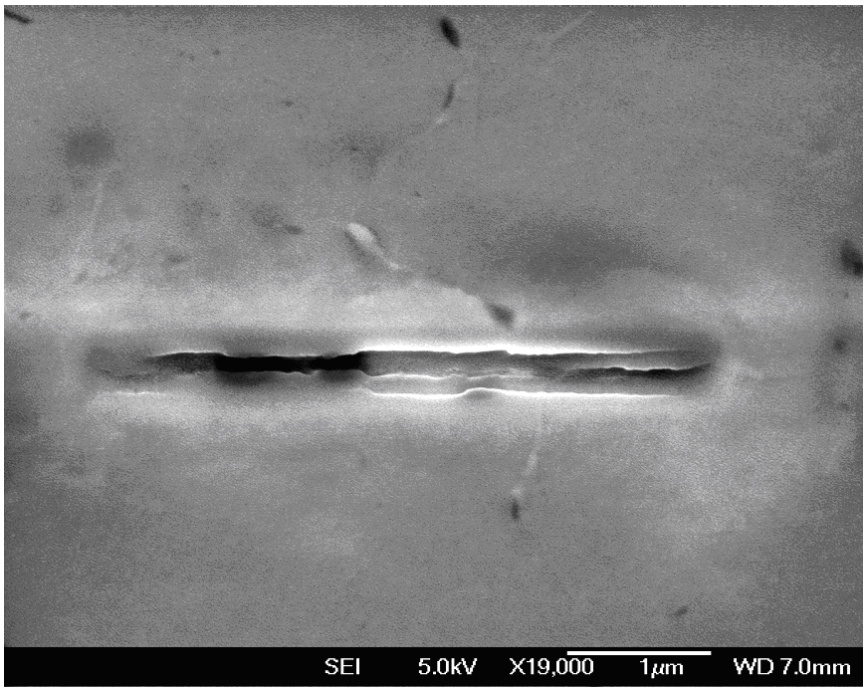

Fig. 4-28 SEM image of the indentation impression of the BLOk^{TM}-1 system when the load level is 5mN.

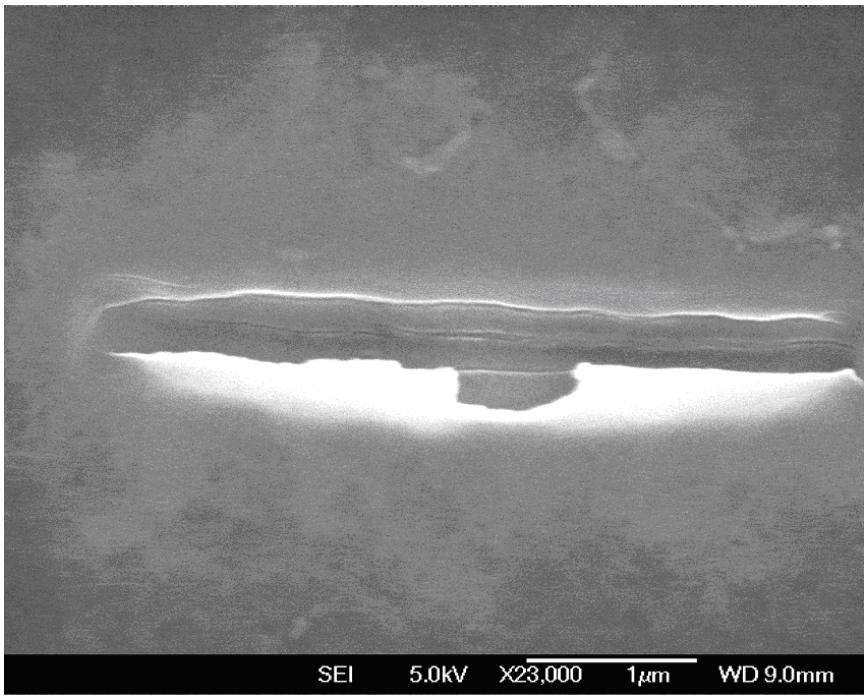

Fig. 4-29 SEM image of the indentation impression of the BLOk^{TM}-2 system when the load level is 5mN.

The bending of the top layers occurs in all the three systems when the indenter penetrates further due to the severe pile-up in the underlayer, copper. It seems that the BLOk^{TM}-1 system has a higher critical load of failure than those of the SiN and SiCO systems. When the BLOk^{TM}-1 system is treated with nitrogen gas to remove the oxygen in the top layer/copper interface thus form the BLOk^{TM}-2 system, the maximum critical load of the system is increased.

From the above discussion, we can conclude that 1) there is no interface delamination between the top layer and copper layer when the indentation penetration is within the top layer; and 2) the top layer fractures when the penetration reaches about 1/2 of the Cu layer, probably due to the bending effects.

4.6.3. Properties of the Top Layer

Theoretically, the scheme that we use to analyze the properties of the single-layer systems can also be applied to these multi-layer systems. However, due to the ultra-thin thickness of the top layer and the resolution limitation of the testing equipment, it is impossible to obtain the film only information. As we can see in the single-layer system, the range in which the substrate effect can be neglected is usually within 10%-15% of the film thickness. Thus, for these multi-layer systems, we need to obtain load-penetration information during the initial 5nm to 7.5nm of penetration, which is beyond the machine resolution. Therefore, it is impossible to derive the mechanical properties of the top layer at this stage. However, it may be possible in the future when equipments with higher resolutions are available, which allows us to conduct simulations of these systems to investigate their adhesion properties.

In summary, wedge indentation can introduce interface delamination in soft-film/hard-substrate systems (e.g. 500nm BD/Si). The interface adhesion properties can be therefore derived by FEM simulations in combination with experiments. However, for hard-film/soft-substrate systems (e.g. SiN/Cu), due to the compliance of the soft substrate (or underlayer), wedge indentation may hardly induce interface delamination, instead, the film fractures due to bending effect. Obviously, to characterize the interface adhesion properties of such systems is still a challenge issue.

References

[1]. D. R. Mumm and A. G. Evans, Acta Mater. 48 (2000) 1815.

[2]. K. L. Johnson, J. Mech. Phys. Solids 18 (1970) 115.

[3]. A. C. Fischer-Cripps, Winumis Software User Manual, CSIRO, Lindfield, 2001.

[4]. A. C. Fischer-Cripps, Nanoindentation, Springer-Verlag, New York, 2002.

[5]. I. N. Sneddon, Fourier Transforms, McGraw-Hill, New York, 1951.

[6]. N. A. Waterman and M. F. Ashby, The Materials Selector, Chapman & Hall, London, 1997.

[7]. L. Shen, K. Zeng, Y. Wang, B. Narayanan and R. Kumar, Microelectron. Eng. 70 (2003) 115.

[8]. L. Shen and K. Zeng, Microelectron. Eng. 71 (2004) 221.

[9]. R. Hill, The Mathematical Theory of Plasticity, Clarendon Press, Oxford, 1950.

[10]. W. S. Ng, The Methodology of Nanoscratch & Nanoindentation for Adhesion Study in Barrier Low-k/Low-k Films, FYP Report, Nanyang Technological University, Singapore, 2003-2004.

Chapter 5 Conclusions and Future Work

5.1. Conclusions

In this project, the mechanical behavior of interface during wedge indentation experiments has been investigated by numerical simulations and experiments. The interface delamination is found to initiate in pure shear (mode II), and subsequently transits into a mixed mode with further propagation. The onset of interface delamination will cause a sudden decrease in the load-penetration curve and the stiffness of the whole system will decrease after the delamination.

The effects of interface adhesion properties, i.e., interface strength and interface energy, on the initiation of interface delamination have been investigated by parametric studies. Increasing either the interface strength $\hat{\sigma}$ or the interface energy Γ_0 will cause an increase in the critical load P_c to initiate interface delamination. The effect of interface strength $\hat{\sigma}$ on the critical load P_c seems to be more significant than that of interface energy Γ_0 when $\hat{\sigma}/\sigma_{yf}$ is larger than 0.4.

Based on the results of parametric studies, the following methodology has been proposed to determine the interface adhesion properties of a thin-film/substrate system: 1) collect basic data of the thin-film/substrate system for numerical simulations either by indentation test or other mechanical tests; 2) perform a series of simulations with different values of the interface adhesion properties to establish the dependence of the critical load P_c and the characteristic load P_d on interface strength $\hat{\sigma}$ and interface energy Γ_0; 3) replot the data to obtain a contour plot, from

which the interface strength $\hat{\sigma}$ and interface energy Γ_0 of a certain system can be extracted once P_c^e and P_d^e are measured by indentation test.

In parallel with simulations, the mechanical properties of thin films have been investigated by wedge indentation experiments. By re-arranging the load-penetration curves and defining the effective stiffness P/h, we identify a range with negligible substrate effect when the indentation depth is shallow. Thus, the mechanical properties of the film can be derived from the load-penetration curve measured within this range. These properties can be used to perform FEM simulations to determine the interface adhesion properties of the thin-film/substrate system tested.

The indentation response shows that the onset of the interface delamination will cause a sudden shift and an uneven distribution of the penetration depth while the development of the corner cracks does not affect the indentation response. Meanwhile, the initiation and propagation of interface delamination will cause a decrease in the effective stiffness of the system.

The simulation results agree well with the experimental ones. Similar characteristics of the load-penetration curves in response to the onset and propagation of interface delamination have been observed. With the mechanical properties such as Young's modulus and yield strength of the thin film obtained from indentation experiments, FEM simulation can be performed for the thin-film/substrate system of interest. The consistency of the simulation and experimental result of the 500nm BD/Si system validates the analysis scheme applied to characterize mechanical properties of the thin film. Furthermore, the values of the interface adhesion

properties, i.e., interface strength and interface energy, of the 500nm BD/Si system are derived.

The results presented here suggest that wedge indentation is a useful tool to characterize the mechanical properties of thin films. The interface adhesion properties of thin-film/substrate system can be determined by FEM simulations in combination with experimentally-measured information.

5.2. Future Work

In view of the results discussed above, some future work may be recommended.

The methodology, which is proposed to determine the interface adhesion properties from experimentally-measured information, should be applied to the single layer systems we tested, i.e., 200nm BD/Si and 500nm BD/Si systems. With the mechanical properties of the thin film obtained from the indentation tests, one can perform a series of FEM simulations for the system and predict the dependence of P_c and P_d on the interface adhesion properties. Then the interface strength $\hat{\sigma}$ and interface energy Γ_0 for the system can be determined from the contour plot and compared with the values derived in this project.

For the multi-layer systems, little work can be done without improvement of the indentation equipment. Once the resolution of the machine is improved, one may obtain the mechanical properties of the ultra thin top layer and observe the indentation response within the top film. However, large amount of work has to be done to simulate the multi-layer systems due to their complexity.

Appendix 1. The values of the coefficients in § 3.4.2.1.

$$A_{11} = \frac{\partial g}{\partial q} + \Delta\varepsilon_p (K \frac{\partial^2 g}{\partial p \partial q} + \sum_{\alpha=1}^{n} \frac{\partial^2 g}{\partial q \partial H^\alpha} \frac{\partial H^\alpha}{\partial \Delta\varepsilon_p})$$

$$+\Delta\varepsilon_q (K \frac{\partial^2 g}{\partial p^2} + \sum_{\alpha=1}^{n} \frac{\partial^2 g}{\partial q \partial H^\alpha} \frac{\partial H^\alpha}{\partial \Delta\varepsilon_p}]$$

$$A_{12} = \frac{\partial g}{\partial p} + \Delta\varepsilon_p (-3G \frac{\partial^2 g}{\partial q^2} + \sum_{\alpha=1}^{n} \frac{\partial^2 g}{\partial q \partial H^\alpha} \frac{\partial H^\alpha}{\partial \Delta\varepsilon_q})$$

$$+\Delta\varepsilon_q (-3G \frac{\partial^2 g}{\partial p \partial q} + \sum_{\alpha=1}^{n} \frac{\partial^2 g}{\partial p \partial H^\alpha} \frac{\partial H^\alpha}{\partial \Delta\varepsilon_q}]$$

$$A_{21} = K \frac{\partial \Phi}{\partial p} + \sum_{\alpha=1}^{n} \frac{\partial \Phi}{\partial H^\alpha} \frac{\partial H^\alpha}{\partial \Delta\varepsilon_p}$$

$$A_{22} = -3G \frac{\partial \Phi}{\partial q} + \sum_{\alpha=1}^{n} \frac{\partial \Phi}{\partial H^\alpha} \frac{\partial H^\alpha}{\partial \Delta\varepsilon_q}$$

$$b_1 = -\Delta\varepsilon_p \frac{\partial g}{\partial q} - \Delta\varepsilon_q \frac{\partial g}{\partial p}$$

$$b_2 = -\Phi$$

Appendix 2. The values of the coefficients in § 3.4.2.2.

$$A_{11} = \frac{\partial g}{\partial q} + \sum_{\alpha=1}^{n}\sum_{\beta=1}^{n}(\Delta\varepsilon_p \frac{\partial^2 g}{\partial q \partial H^\alpha} + \Delta\varepsilon_q \frac{\partial^2 g}{\partial p \partial H^\alpha}) c_{\alpha\beta} \frac{\partial h^\beta}{\partial \Delta\varepsilon_p}$$

$$A_{12} = \frac{\partial g}{\partial p} + \sum_{\alpha=1}^{n}\sum_{\beta=1}^{n}(\Delta\varepsilon_p \frac{\partial^2 g}{\partial q \partial H^\alpha} + \Delta\varepsilon_q \frac{\partial^2 g}{\partial p \partial H^\alpha}) c_{\alpha\beta} \frac{\partial h^\beta}{\partial \Delta\varepsilon_q}$$

$$A_{21} = \sum_{\alpha=1}^{n}\sum_{\beta=1}^{n}\frac{\partial \Phi}{\partial H^\alpha} c_{\alpha\beta} \frac{\partial h^\beta}{\partial \Delta\varepsilon_p}$$

$$A_{22} = \sum_{\alpha=1}^{n}\sum_{\beta=1}^{n}\frac{\partial \Phi}{\partial H^\alpha} c_{\alpha\beta} \frac{\partial h^\beta}{\partial \Delta\varepsilon_q}$$

$$B_{11} = \frac{1}{3}\Delta\varepsilon_p(\frac{\partial^2 g}{\partial p \partial q} + \sum_{\alpha=1}^{n}\sum_{\beta=1}^{n}\frac{\partial^2 g}{\partial q \partial H^\alpha} c_{\alpha\beta} \frac{\partial h^\beta}{\partial p}) + \frac{1}{3}\Delta\varepsilon_q(\frac{\partial^2 g}{\partial p^2} + \sum_{\alpha=1}^{n}\sum_{\beta=1}^{n}\frac{\partial^2 g}{\partial p \partial H^\alpha} c_{\alpha\beta} \frac{\partial h^\beta}{\partial p})$$

$$B_{12} = -\Delta\varepsilon_p(\frac{\partial^2 g}{\partial q^2} + \sum_{\alpha=1}^{n}\sum_{\beta=1}^{n}\frac{\partial^2 g}{\partial q \partial H^\alpha} c_{\alpha\beta} \frac{\partial h^\beta}{\partial q}) - \Delta\varepsilon_q(\frac{\partial^2 g}{\partial p \partial q} + \sum_{\alpha=1}^{n}\sum_{\beta=1}^{n}\frac{\partial^2 g}{\partial p \partial H^\alpha} c_{\alpha\beta} \frac{\partial h^\beta}{\partial q})$$

$$B_{21} = \frac{1}{3}(\frac{\partial \Phi}{\partial p} + \sum_{\alpha=1}^{n}\sum_{\beta=1}^{n}\frac{\partial \Phi}{\partial H^\alpha} c_{\alpha\beta} \frac{\partial h^\beta}{\partial p})$$

$$B_{22} = -(\frac{\partial \Phi}{\partial q} + \sum_{\alpha=1}^{n}\sum_{\beta=1}^{n}\frac{\partial \Phi}{\partial H^\alpha} c_{\alpha\beta} \frac{\partial h^\beta}{\partial q})$$

$$m_{pI} = \frac{A_{22}B_{11} - A_{12}B_{21}}{A_{11}A_{22} - A_{21}A_{12}}$$

$$m_{pn} = \frac{A_{22}B_{12} - A_{12}B_{22}}{A_{11}A_{22} - A_{21}A_{12}}$$

$$m_{qI} = \frac{A_{21}B_{11} - A_{11}B_{21}}{A_{12}A_{21} - A_{22}A_{11}} = \frac{A_{11}B_{21} - A_{21}B_{11}}{A_{11}A_{22} - A_{21}A_{12}}$$

$$m_{qn} = \frac{A_{21}B_{22} - A_{11}B_{22}}{A_{12}A_{21} - A_{22}A_{11}} = \frac{A_{11}B_{22} - A_{21}B_{12}}{A_{11}A_{22} - A_{21}A_{12}}$$